AFRL-AFOSR-UK-TR-2011-0064

Metamaterial-Based Cylinders Used for Invisible Cloak Realization

Zvonimir Sipus
Dario Bojanjac
Branimir Ivsic
Tin Komljenovic

University of Zagreb
Faculty of Electrical Engineering and Computing
Unska 3
Zagreb, Croatia HR-10000

EOARD GRANT 10-3024

Report Date: August 2011

Final Report from 23 July 2010 to 23 July 2011

Air Force Research Laboratory
Air Force Office of Scientific Research
European Office of Aerospace Research and Development
Unit 4515 Box 14, APO AE 09421

REPORT DOCUMENTATION PAGE

Form Approved OMB No. 0704-0188

1. REPORT DATE *(DD-MM-YYYY)*	2. REPORT TYPE	3. DATES COVERED *(From – To)*
01-08-2011	Final Report	23 July 2010 – 23 July 2011

4. TITLE AND SUBTITLE

Metamaterial-Based Cylinders Used for Invisible Cloak Realization

5a. CONTRACT NUMBER

FA8655-10-1-3024

5b. GRANT NUMBER

Grant 10-3024

5c. PROGRAM ELEMENT NUMBER

61102F

6. AUTHOR(S)

Zvonimir Sipus
Dario Bojanjac
Branimir Ivsic
Tim Komljenovic

5d. PROJECT NUMBER

5d. TASK NUMBER

5e. WORK UNIT NUMBER

7. PERFORMING ORGANIZATION NAME(S) AND ADDRESS(ES)

University of Zagreb
Faculty of Electrical Engineering and Computing
Unska 3
Zagreb, Croatia HR-10000

8. PERFORMING ORGANIZATION REPORT NUMBER

N/A

9. SPONSORING/MONITORING AGENCY NAME(S) AND ADDRESS(ES)

EOARD
Unit 4515 BOX 14
APO AE 09421

10. SPONSOR/MONITOR'S ACRONYM(S)

AFRL/AFOSR/RSW (EOARD)

11. SPONSOR/MONITOR'S REPORT NUMBER(S)

AFRL-AFOSR-UK-TR-2001-0064

12. DISTRIBUTION/AVAILABILITY STATEMENT

Approved for public release; distribution is unlimited. (approval given by local Public Affairs Office)

13. SUPPLEMENTARY NOTES

14. ABSTRACT

The realization of structures that do not scatter electromagnetic field, i.e. structures that appear invisible for EM waves is not a new concept. The possibility of a plane wave passing through some structure without distortions (i.e. with zero scattered field) has been investigated theoretically since 1960s (see e.g. [1]-[4]). Recently, the possibility of cloaking objects using a metamaterial cover has extensively been studied ([5]-[7]). In this approach, material has been used to render a volume effectively invisible to incident radiation, i.e. to squeeze space from a volume into a shell surrounding the concealment volume. Coordinate transformations that are used for cloak design do not influence the form of Maxwell's equations, but they affect permittivity and permeability tensors (ε and μ respectively), making the needed materials spatially varying and anisotropic. When viewed externally, the concealed volume and the cloak both appear to have the propagation properties of free space, i.e. they appear invisible to electromagnetic waves. The required anisotropy is supposed to be obtained by using metamaterials.

The main realized outcomes of the project is the development of the program "UniaxCloak" that analyzes cylindrical and spherical cloaks made from the uniaxial materials. The program can fully characterize uniaxial cloaks, i.e. it calculates scattered width and total scattered width in a frequency range of interest. In the cylindrical case, the incident wave can have arbitrary angle of incidence. And we have made a detailed investigation of properties of cloaks that are made from uniaxial materials. In practice, such cloaks can be made from metamaterials, for example from split-ring periodic structures or periodic wire structures.

15. SUBJECT TERMS

EOARD, metamaterials, invisible cloak

16. SECURITY CLASSIFICATION OF:			17. LIMITATION OF ABSTRACT	18, NUMBER OF PAGES	19a. NAME OF RESPONSIBLE PERSON
a. REPORT	b. ABSTRACT	c. THIS PAGE			SCOTT DUDLEY, Lt Col, USAF
UNCLAS	UNCLAS	UNCLAS	SAR	94	19b. TELEPHONE NUMBER *(Include area code)* +44 (0)1895 616162

FINAL REPORT FOR CONTRACT **FA8655-10-1-3024**

Metamaterial-Based Cylinders Used for Invisible Cloak Realization

by

Zvonimir Sipus
Dario Bojanjac
Branimir Ivsic
Tin Komljenovic

SUBMITTED BY: Prof. Zvonimir Sipus
Faculty of Electrical Engineering and Computing
University of Zagreb
Unska 3
Zagreb, HR-10000, Croatia

20 July 2011

Grant/Cooperative Agreement Award

1. AWARD NO.	2. EFFECTIVE DATE	3. PURCHASE REQUEST NO.	4. CFDA NO.	PAGE OF
FA8655-10-1-3024	22 JUL 2010	See Block 16	12.800	1 3

5. ISSUE BY EOARD CODE FA8655	6. AWARDED TO CAGE CODE A01MB	7. AUTHORITY
EUROPEAN OFFICE OF AEROSPACE RESEARCH AND DEVELOPMENT UNIT 4515 BOX 14 APO AE 09421 USA WENDY HARRISON +44(0)18956161 wendy.harrison@london.af.mil	UNIVERSITY OF ZAGREB FACULTY OF ELECTRICAL ENGINEERING UNSKA 3 ZAGREB HR-10000 CROATIA	10 U.S.C. 2358 8. PERIOD OF PERFORMANCE 22 July 2010 To 21 July 2011

9. SCOPE / AGREEMENT TERMS

Assistance is for Research entitled, "Metamaterial-Based Cylinders Used for Invisible Cloak Realization ." The "Air Force Research Laboratory Grants Terms and Conditions Sep 2009 - Awards to International Educational Institutions and Non-Profit Organizations" and the Recipient's Technical Proposal are incorporated by reference. Awardee signature is not required on this agreement; however, the recipient agrees to the conditions specified in this award unless notice of disagreement is furnished to the awarding officer within 15 days after the signature date. In case of disagreement, the recipient shall not incur any costs until the disagreement is resolved.

10. RECIPIENT PRINCIPAL INVESTIGATOR	11. OTHER SPONSORING AGENCY(S)
Professor Zvonimir Sipus	N/A

12. ADMINISTRATIVE OFFICE CODE FA8655	13. PAYING OFFICE CODE: F78900	14. STAFF JUDGE ADVOCATE OFFICE
EUROPEAN OFFICE OF AEROSPACE RESEARCH AND DEVELOPMENT 86 BLENHEIM CRESCENT RUISLIP, MIDDLESEX HA4 7HB UNITED KINGDOM	DFAS-LI 27 ARKANSAS ROAD LIMESTONE MAINE 04751-6216 USA	AFOSR/JA (703) 696-9500 875 NORTH RANDOLPH STREET SUITE 325, ROOM 3112 ARLINGTON, VIRGINIA 22203 USA

15. GOVT PROGRAM MANAGER (Name, Org, Tel, Email)
Scott Dudley, Lt Col, USAF, +44 (0) 189 561 6162, Scott.Dudley@london.af.mil

16. ALLOCATED FUNDING: The following funds with associated Accounting Classification reference number(s) (ACRNs) are allotted to this agreement:

ACRN	FUND CITATION(s)	AMOUNT
	SEE CONTINUATION	

SPECIAL INSTRUCTIONS: PAYMENT WILL BE MADE BY ELECTRONIC FUNDS TRANSFER.
PAYING OFFICE INSTRUCTIONS: USE EARLIEST CITED FUNDS FIRST.
PAYMENT SCHEDULE (if applicable): SEE FOLLOWING PAGE(S) FOR REPORT AND PAYMENT SCHEDULE AND INSTRUCTIONS

	Government Share	Recipient Share	Total	18. INVOICE INSTRUCTION
17. TOTAL FUNDS OBLIGATED	$30,000.00	$0.00	$30,000.00	INVOICES NOT REQUIRED - SEE FOLLOWING PAGE(S)
19. AMOUNT OF AWARD	$30,000.00	$0.00	$30,000.00	
20. OPTIONS N/A	Government Share	Recipient Share	Total	21. PERIOD

FOR THE RECIPIENT		FOR THE UNITED STATES OF AMERICA	
22. SIGNATURE		23. SIGNATURE	
24. NAME AND TITLE	25. DATE SIGNED	26. NAME AND TITLE WENDY HARRISON GRANTS OFFICER	27. DATE SIGNED 22 Jul 10

ConWrite Version 6.12.0
Created 22 Jul 2010 3:03 PM

TABLE OF CONTENTS

1 INTRODUCTION

Introduction

The realization of structures that do not scatter electromagnetic field, i.e. structures that appear invisible for EM waves in outer space, is not a new concept. The possibility of a plane wave passing without distortions through a structure with anisotropic filling was theoretically first investigated in 1960s, see [1]. The basis of the work was the invariance property of Maxwell's equations with respect to transformation of space metric and permeability and permittivity tensors of the medium. In [2]-[5] it was shown that for certain combinations of permittivities in a two-layer dielectric ellipsoid, the scattered field is zero. The analysis revealed that at least one of the layers should have relative permittivity smaller than one (i.e. local negative polarizability, which is inherent to plasmonic materials and plasma-like ENG metamaterials), and moreover such structures have the advantage of not requiring anisotropic materials. In [6], hard surfaces were used in the design of supporting struts of reflector antenna feeds, to reduce their blockage in reflector systems. In this way it is possible to considerably reduce the scattered field for one angle of incidence, for both polarizations of the incident wave. Several other concepts for obtaining invisible scatterers were proposed, like minimum scattering antennas and active scatterers ([7], [8]).

The possibility of cloaking objects using a metamaterial cover has extensively been studied (see e.g. [9]-[13]). Metamaterials are new composite materials that recently have found applications in the design of antennas and microwave components. These special materials can be formed by periodic arrangements of many sub-wavelength inclusions in a dielectric environment, in such a way as to achieve macroscopic electromagnetic or optical properties that cannot be found in nature. In the metamaterial cloak approach, material has been used to render a volume effectively invisible to incident radiation, i.e. to squeeze space from a volume into a shell surrounding the concealment volume. The perfect cloak ensures that for any incident field the electromagnetic scattered field vanishes in the free-space external to the cloaking shell, and the total field vanishes inside the free-space cavity of the shell. Thus, any object placed in the cavity does not perturb the electromagnetic field outside the cloak, and an external observer does not see the object and the cloak, like they are absent. However, the coordinate transformations that are used for cloak design do not affect the form of Maxwell’s equations, but they influence permittivity and permeability tensors. Consequently, the materials needed for building the cloak are fully anisotropic with spatially-varying constitutive parameters.

The first practical realization of a cloak was made by Schurig *et al.* in 2006 [14]. The realized cloak was not fully anisotropic, but it was designed to work for only one polarization (TM_z polarization). By this design of metamaterial layers with only the radial dependence of the radial permeability component was needed, and it was realized using the split-ring resonators. The described cloak was prototyped and embedded into scattering chamber. The distribution of the vertical component of the electric field around the cloak was scanned, and the obtained results showed some decrease of the scattered field. Although this experiment proved the basic idea of cloaking, the level of scattered field has not been quantified.

Previous work in invisibility, therefore, gives rise to several questions:

1. Why the developed cloak with the reduced variation of constitutive parameters (i.e. cloaks made from uniaxial materials) scatters the electromagnetic field, even in the ideal case?
2. Is it possible to realize a cloak with the reduced variation of constitutive parameters that is entirely invisible (at least at the central frequency)?
3. What is the bandwidth of a cloak that is built using metamaterial layers? Is it possible to enlarge the bandwidth of such a cloak?
4. Is it possible to realize a cloak with the reduced variation of constitutive parameters that work for oblique direction of incident wave?
5. Is it possible to realize a cloak that is invisible to pulse excitation (i.e. to radar)?
6. Is it possible to extend the single-curved models (cloaks) to double-curved structures?

The purpose of the project is, therefore, to provide further analysis of this issue.

The possible application of the developed cloak will be reduction of the scattered field from some mechanical structure. In more details, there are many situations where electromagnetic waves are obstructed by some mechanical structure. The obstruction may represent aperture blockage causing increased sidelobes and reduced gain, if the structure is a part of the antenna system or if it is placed close to the antenna. Examples of such structures are objects placed in the vicinity of the antenna system (e.g. musts on ships near radars or communication systems), supporting struts in large reflector systems, etc. In all such systems the frequency, polarization and angle of incidence are known which allows us to construct a special structure that will reduce the scattered field.

2 PROJECT OBJECTIVE AND REALIZED OUTCOMES

Project objective and realized outcomes

Uniaxial cylindrical cloaks have recently been proposed to prevent scattering of electromagnetic waves, i.e. to render objects invisible. The proposed cloaks with reduced variation of constitutive parameters suffer from nonzero reflectance, i.e. they are only partly invisible. Therefore, the purpose of a 12-month effort is to develop an analysis method and the corresponding software for analyzing cylinders made from metamaterial-based concentric layers with an application to invisible cloak realization. The main parameter of interest is the scattered field, i.e. if the considered structure really appears invisible to the incident wave. The considered structures are modeled as a multilayer anisotropic cylinder where both permittivity and permeability tensors are diagonal in the cylindrical coordinate system. The active cloaks can be also analyzed in this way since their homogeneous electromagnetic model is based on complex constitutive parameters. We have considered incident electromagnetic waves coming both from normal and oblique incident direction. The proposed analysis method is connected with a suitable global optimization routine, and the developed software package is used to help in cloak design. A possible application of the considered prototype is reduction of scattered field from mechanical structures that need to be placed in front of big antennas, such as radar antennas or reflector systems.

The work in the project has been divided in the following tasks:

1. Making a detailed investigation of properties of cloaks that are made from uniaxial materials, e.g. from metamaterial layers. The investigation includes characterization of already developed cloaks and extensive investigation of the cloak bandwidth.
2. Extension of the program for analyzing uniaxial multilayer cylinders – with the extended version it will be possible to analyze the case when the incident field has oblique direction of propagation and oblique polarization.
3. Merging the program for analyzing uniaxial cylindrical structures with the global optimization program. As a global optimization algorithm we have chosen the Particle Swarm Optimization (PSO) algorithm. This is an evolutionary algorithm similar to the genetic algorithm and to the simulated annealing, but it operates on a model of social interactions between independent agents and utilizes swarm intelligence to achieve the goal of optimization problems. It was chosen here since the associated algorithm has the same or better performances comparing to other global optimization programs.
4. Extension of the program to include the analysis of spherical cloaks. By this it will be possible to analyze double-curved cloaking structures.

The main realized outcomes of the project are:

- We have developed the program “UniaxCloak” that analyzes cylindrical and spherical cloaks made from the uniaxial materials. The program can fully characterize uniaxial cloaks, i.e. it calculates scattered width and total scattered width in a frequency range of interest. In the cylindrical case, the incident wave can have arbitrary angle of incidence.
- We have merged the program “UniaxCloak” with the global optimization program based on the particle swarm optimization (PSO) method. By this one can determine the optimum cloak design since the analysis methods based on the transformation electromagnetics do not take all the effects into account.
- We have made a detailed investigation of properties of cloaks that are made from uniaxial materials. In practice, such cloaks can be made from metamaterials, for example from split-ring periodic structures or periodic wire structures.

3 ANALYSIS OF UNIAXIAL MULTILAYER CYLINDERS USED FOR INVISIBLE CLOAK REALIZATION

Analysis of uniaxial multilayer cylinders used for invisible cloak realization

3.1. INTRODUCTION

The possibility of cloaking objects using a metamaterial cover has extensively been studied (see e.g. [9]-[13]). In the metamaterial cloak approach, material has been used to render a volume effectively invisible to incident radiation, i.e. to squeeze space from a volume into a shell surrounding the concealment volume. Coordinate transformations that are used for cloak design do not influence the form of Maxwell's equations, but they affect permittivity and permeability tensors (**ε** and **μ**, respectively), making the needed materials spatially varying and anisotropic. When viewed externally, the concealed volume and the cloak both appear to have the propagation properties of free space, i.e. they appear invisible to electromagnetic waves.

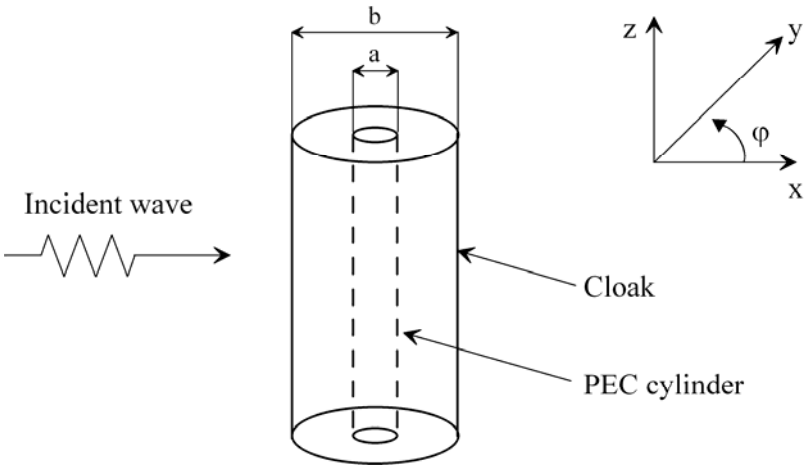

Figure 3.1. A sketch of the analyzed structure.

The considered structure consists of a PEC cylinder (object being cloaked) and of a metamaterial cloak. A sketch of the analyzed structure is given in Fig. 3.1. For the cloak design, a coordinate transformation which compresses free space from the cylindrical region $0 < r < b$ into the concentric cylindrical shell $a < r' < b$ is applied, where a and b represent the cloak inner and outer radius, respectively (the constitutive structure parameters are considered

in the cylindrical coordinate system). The used transformation leads to the following expressions for the components of the permittivity and permeability tensors [9]:

$$\begin{aligned} \varepsilon_r &= \mu_r = \frac{r-a}{r} \\ \varepsilon_\varphi &= \mu_\varphi = \frac{r}{r-a} \\ \varepsilon_z &= \mu_z = \left(\frac{b}{b-a}\right)^2 \frac{r-a}{r}. \end{aligned} \tag{3.1a}$$

Note that all components of the tensors are functions of radius, which implies a very complicated metamaterial design. Such a cloak is referred to as an ideal cloak that has not yet been realized. However, several cloak designs have been reported which claim to work properly when illuminated with a normal incident plane wave of specific polarization [14, 15], that is, with either the electric field or the magnetic field parallel to the z-axis (TM_z polarization or TE_z polarization, respectively).

The metamaterial cloak, designed by Schurig *et al.* [14], is intended for use with TM_z polarization of the incident wave at microwave frequencies. It is clear that only ε_z, μ_r and μ_φ components are relevant in this case. A significantly simplified design can be achieved by fixing values of ε_z and μ_φ and letting only μ_r to vary along the radial direction:

$$\begin{aligned} \varepsilon_z &= \left(\frac{b}{b-a}\right)^2 \\ \mu_r &= \left(\frac{r-a}{r}\right)^2 \\ \mu_\varphi &= 1. \end{aligned} \tag{3.1b}$$

The metamaterial reported in [14] used the unit cell of approximately cubic shape, filled with one split-ring resonator. The realized cloak consisted of ten concentric cylinders, each of which was three unit cells tall.

In the simulations presented in [14], both realizations of the cloak were considered (i.e., the cloak based on ideal material as well as the cloak based on the simplified material with spatially varying permeability). When simulating the simplified version, the continuous variation of $\mu_r(r)$ through the structure was approximated by a 10-step piecewise constant function, that mimicked the concentric rings of the fabricated cloak. The results revealed that the cloak reduced both the back-scattered field (reflection) and the forward-scattered field (shadow). The described cloak was also prototyped and embedded into scattering chamber. The distribution of the vertical component of the electric field around the cloak was scanned, and the obtained results showed some decrease of the scattered field. Although this experiment proved the basic idea of cloaking, the level of scattered field has not been quantified.

Similarly to the realization of a so-called TM_z cloak, there is another realization of metamaterial cloak by Cai *et al.* [15]. This cloak is intended to work with TE_z polarized wave

at optical frequencies. In TE_z cloak only components μ_z, ε_r and ε_φ are relevant, thus it is again possible to simplify the metamaterial design by allowing only ε_r to vary in radial direction:

$$\begin{aligned} \mu_z &= 1 \\ \varepsilon_r &= \left(\frac{r-a}{r}\right)^2 \cdot \left(\frac{b}{b-a}\right)^2 \\ \varepsilon_\varphi &= \left(\frac{b}{b-a}\right)^2. \end{aligned} \tag{3.1c}$$

The required distribution of ε_r is realized using metal wires embedded in a dielectric material, i.e. with a thin wire plasma-like metamaterial. Here, the effective permittivity varies in radial direction and its real part has to exhibit the required behaviour ($0<\mathrm{Re}\{\ \varepsilon_r\ \}<1$) with negligible imaginary part (i.e with negligible losses) [15].

The purpose of this chapter is to provide the analysis of uniaxial multilayer cylinders used for invisible cloak realization. Furthermore, we will discuss how dispersion influences cloak properties, i.e. we will try to determine the frequency bandwidth of the considered cloaks.

3.2. THEORETICAL CONSIDERATIONS

We consider a circular-cylindrical cloak with the axis in *z*-direction (see Fig.3.1). The incident plane wave propagates in the positive *x*-direction (i.e. the normal incidence, the oblique incidence will be treated in section 5), while the electric field is assumed to be parallel with the *z*-axis (TM_z polarization; TE_z polarization is going to be treated afterwards). In cylindrical coordinates the E_z electric field component is given in the form:

$$E_z(r,\varphi) = \sum_{m=-\infty}^{\infty} j^m \mathrm{J}_m(k_0 r) e^{-jm\varphi}, \tag{3.2}$$

where $\mathrm{J_m}$ is the *m*-th order Bessel function of the first kind and k_0 is the wave number ($k_0=2\pi/\lambda_0$). Since the incident wave propagates perpendicularly to the cylinder axis, there is no variation of the field in the *z*-direction (i.e. $\partial/\partial z = 0$). Consequently, the curl Maxwell equations can be written as:

$$\begin{aligned} H_r &= -\frac{1}{j\omega\mu_r r}\frac{\partial E_z}{\partial \varphi} \\ H_\varphi &= \frac{1}{j\omega\mu_\varphi}\frac{\partial E_z}{\partial r} \\ \frac{1}{r}\left(\frac{\partial}{\partial r}\left(rH_\varphi\right) - \frac{\partial H_r}{\partial \varphi}\right) &= j\omega\varepsilon_z E_z. \end{aligned} \tag{3.3}$$

By combining these equations and assuming piecewise constant approximation of radial permeability variation, we obtain the following form of Bessel's differential equation for the E_z component of the electric field:

$$r^2 \frac{\partial^2 E_z}{\partial r^2} + r \frac{\partial E_z}{\partial r} + (k^2 r^2 - \bar{m}^2) E_z = 0, \tag{3.4}$$

where $k = \omega^2 \mu_\varphi \varepsilon_z$ and $\bar{m} = m\sqrt{\mu_\varphi / \mu_r}$.

The general solution of (3.4) is:

$$C_1 \mathrm{J}_{\bar{m}}(kr) + C_2 \mathrm{H}^{(2)}_{\bar{m}}(kr), \tag{3.5}$$

where C_1 and C_2 represent constants (to be determined from the boundary conditions), while $\mathrm{J}_{\bar{m}}$ and $\mathrm{H}^{(2)}_{\bar{m}}$ are Bessel functions of the first kind and Hankel functions of the second kind of order $\bar{m}$, respectively. For the TE_z cloaking cylinder we obtain the equivalent differential equation, by applying the substitutions $E_z \rightarrow H_z$, $\varepsilon \rightarrow \mu$ and $\mu \rightarrow \varepsilon$. Note that the resulting order of Bessel functions ($\bar{m}$) for both cloaks is not integer and that it depends on both permeability and permittivity tensors (**μ** and **ε)**.

The multilayered structure is analyzed using G1DMULT algorithm [16], which calculates the spectral-domain Green's functions in the same way for planar, circular-cylindrical and spherical geometries. The algorithm is based on dividing the multilayer problem into equivalent sub-problems, one for each dielectric layer. For normal incidence the fields inside each layer of the cylindrical structure are of the form (e.g. E_z component):

$$E_z(r, m) = a_m^i \mathrm{J}_m(k^i r) + b_m^i \mathrm{H}_m^{(2)}(k^i r) \tag{3.6}$$

Here k^i is the wave number in i-th layer, and a_m^i and b_m^i are the unknown coefficients to be determined. The equivalent sub-problems are interrelated (and the coefficients a_m^i and b_m^i are calculated) by enforcing the continuity of tangential components of electric and magnetic fields over the layer interfaces, in spectral domain. The implementation of radially anisotropic structures into the G1DMULT algorithm is quite simple – one only needs to change the order of Bessel/Hankel function in each anisotropic layer according to the equation (3.5). More details about G1DMULT can be found in [16].

3.3. RESULTS OF THE CLOAK ANALYSIS

In order to characterize the level of "invisibility" achieved by metamaterials, we have calculated the total scattering width (σ_T) of the cloaked cylinder, i.e. the total scattered power per unit length normalized with the incident power density [17]. In scientific literature there is another parameter for characterizing scattering objects – the equivalent blockage width (W_{eq}). It is a complex-valued parameter (introduced in [6]) that represents the width of an ideal

shadow which produces the same forward-scattered field as the cylinder that is being observed (in our case, a cloaking cylinder). Both W_{eq} and σ_T are quantities that actually show how wide the cylinder seems to electromagnetic waves. There is a simple relation between these two parameters for lossless scatterers – σ_T is just equal to $2 \cdot \mathrm{Re}(W_{eq})$. Therefore, the considered cloaks can be characterized with total scattering width only. We have also calculated the angular variation of bistatic scattering width (σ_{2D}) in order to check if there is any direction with distinctively stronger scattered field.

3.3.1. Ideal cloak

The metamaterial constitutive parameters have been calculated by equation (3.1a). Our intention was to thoroughly investigate cloak that was experimentally realized by Schurig *et al*. [14]. Therefore, we have selected the same dimensions and the working frequency as in the experimental model case. The cylinder axis is set in *z*-direction and the cloak inner and outer radii are a = 2.71 cm and b = 5.89 cm, respectively. All components (r, φ and z) of permittivity and permeability tensors have gradients as a function of radius. Such anisotropy has been approximated by 1- to 10- steps piecewise constant functions representing the stepwise cloak realization, in order to analyze how the subtlety of the approximation of radial anisotropy influences the total scattering width, i.e. “the invisibility”.

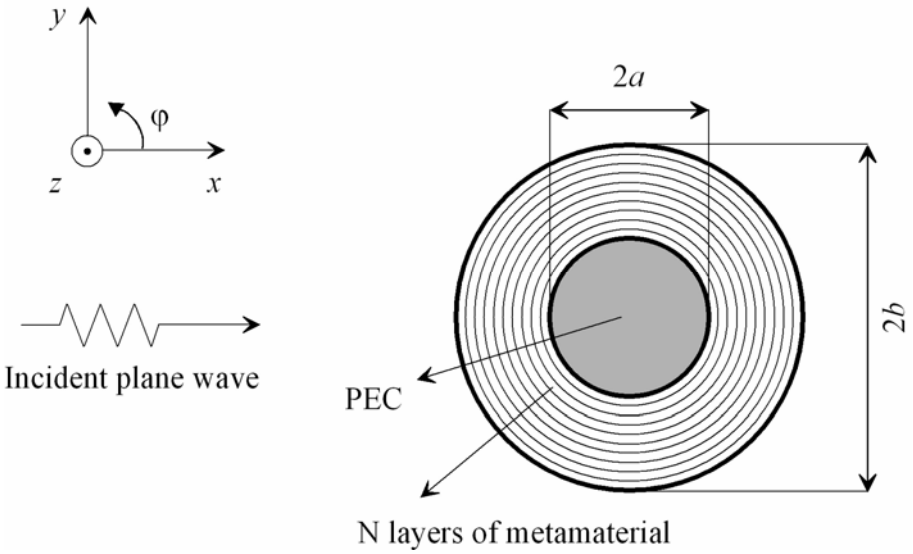

Figure 3.2. A sketch of the analyzed structure. The cloak contains *N* concentric cylindrical metamaterial layers.

In order to compare different cloak realizations, first we performed one referent simulation for the case without any cloak, i.e. with only PEC circular cylinder present. The radius of the considered cylinder is a = 2.71 cm. The total scattering width of the PEC cylinder is equal to 12.71 cm for TM_z and 8.98 cm for TE_z polarization of the incident wave at the working frequency of 8.5 GHz, see Fig. 3.3. By calculating the total scattering widths for the cases with cloaks present it also becomes possible to compare the obtained invisibility for the two analyzed cases (the case with the cloak present and the case without the cloak - a referent case). The obtained invisibility could also be described by total scattering width reduction (ratio of total scattering widths for the two cases).

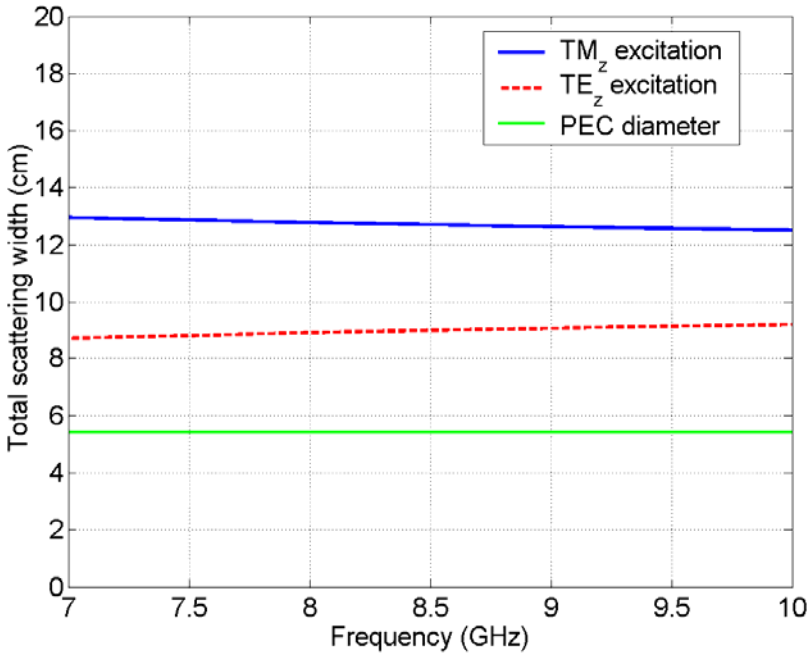

Figure 3.3. Total scattering width of PEC cylinder for normal incidence. Both TM_z and TE_z polarizations are shown.

Due to the full anisotropy, the ideal cloak is supposed to work for arbitrary polarization. Therefore, complete analysis is provided for both the cloak excited by the TE_z and the cloak excited by TM_z polarized waves. The simulations have been performed at the central frequency (8.5 GHz). The calculated total scattering width and the angular variation of bistatic scattering width are shown in Figs. 3.4 – 3.7. It can be seen that by increasing the number of metamaterial layers, the achieved invisibility improves. Thus, it can be concluded that the 10-layer approximation of the continuous anisotropic structure is good enough for practical purposes (even 5-layers realization has a very good performance). It can also be noted that the level of scattered field is low for both polarizations (Figures 3.6 and 3.7) and, as expected, the invisibility was achieved for both excitations.

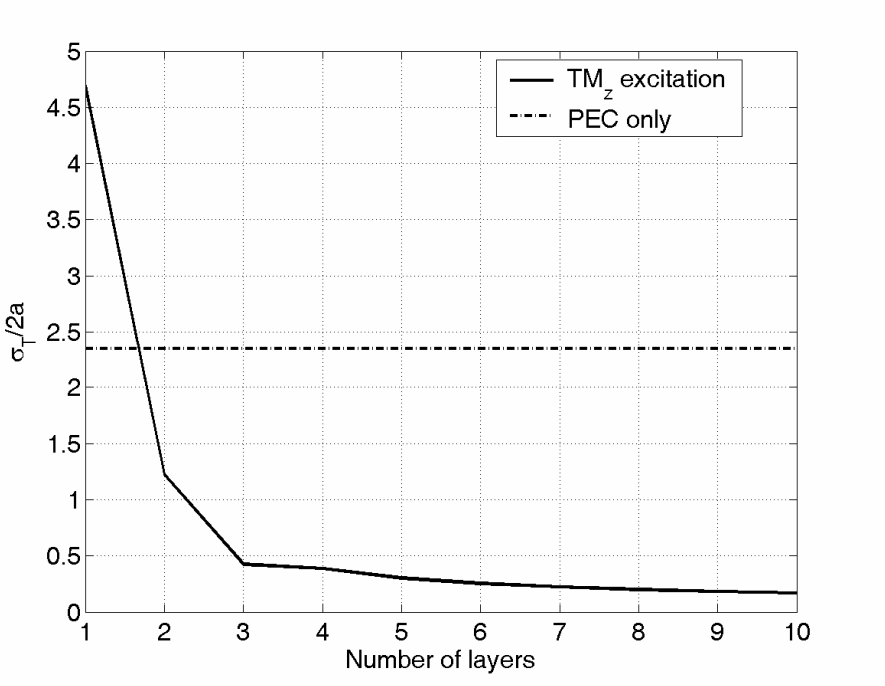

Figure 3.4. Normalized total scattering width vs. number of layers for ideal cloak (TM_z polarization).

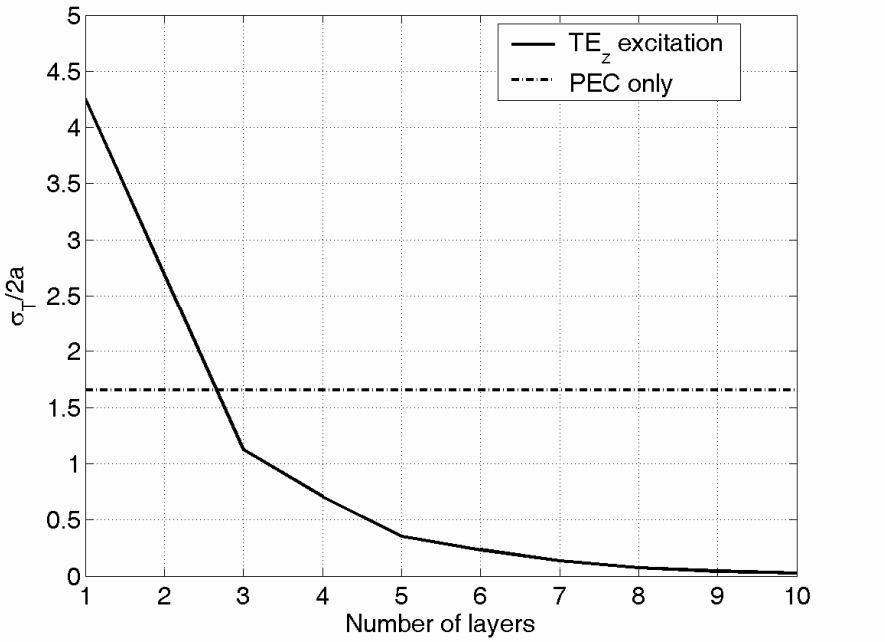

Figure 3.5. Normalized total scattering width vs. number of layers for ideal cloak (TE_z polarization).

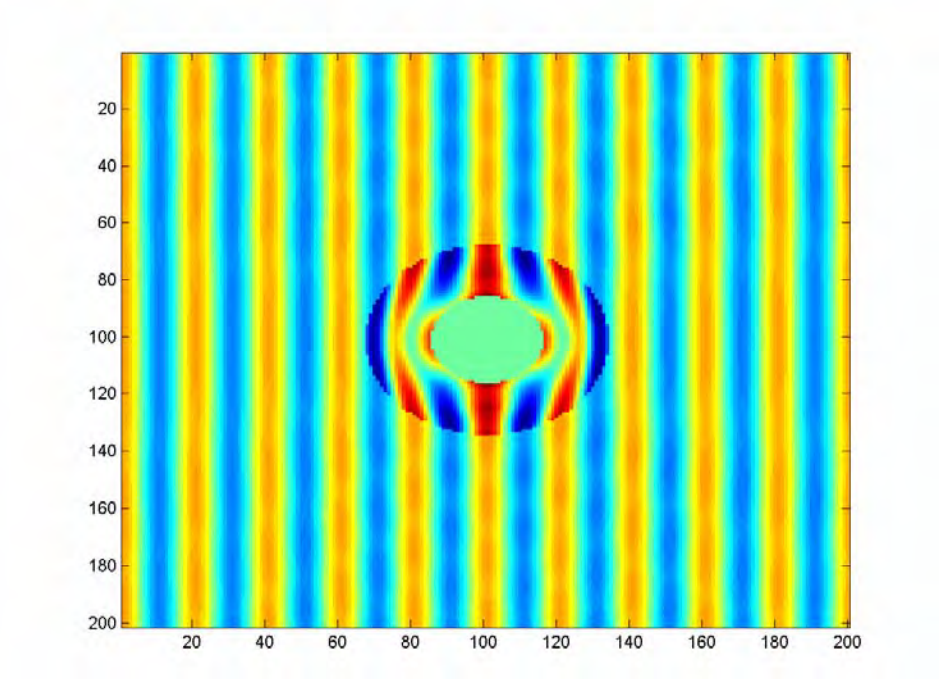

Figure 3.6. Electric-field distribution in the vicinity of the 10-layers realization of ideal cloaking cylinder (TM_z polarization).

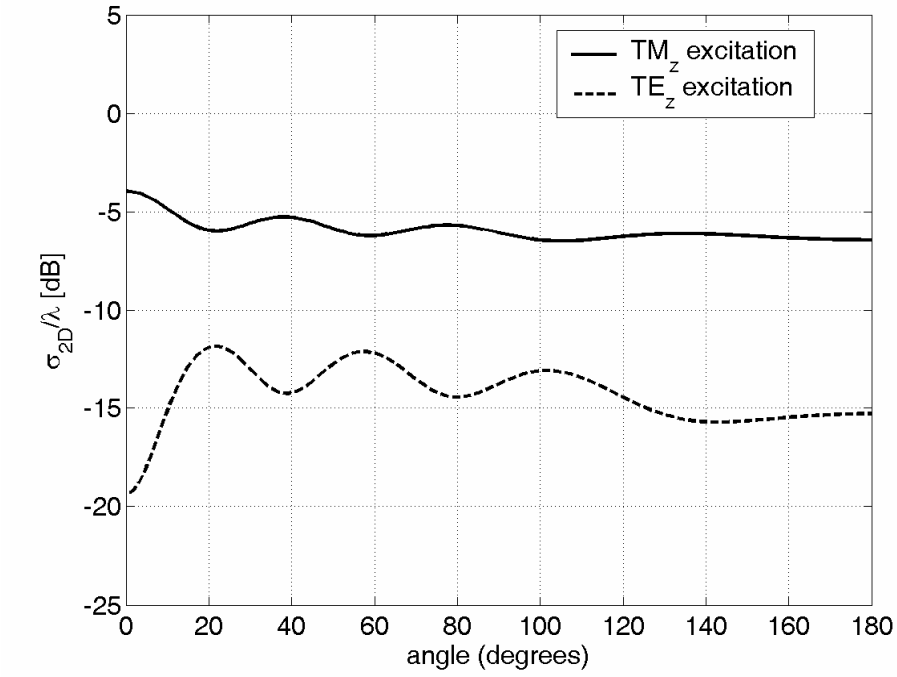

Figure 3.7. Normalized bistatic scattering width of 10-layers realization of ideal cloaking cylinder (TE_z and TM_z polarization).

3.3.2. TM_z cloak (Schurig cloak)

For the TM_z cloak, the coordinate transformations for metamaterial design have been simplified, so the metamaterial constitutive parameters were calculated by equation (3.1b). Such simplified cloak should work only for TM_z polarization and thus only ε_z, μ_r and μ_φ components are relevant. From equation (3.1b) it can also be seen that both the permittivity tensor component in z-direction and the permeability tensor component in φ-direction are constant. Furthermore, only radial anisotropy of permeability tensor ($\mu_r(r)$) is present. This anisotropy is approximated with 1 to 10- steps piecewise constant functions in a way mentioned before.

The analysis of how the subtlety of the approximation of radial anisotropy influences the total scattering width (i.e. the "invisibility") has been given only for excitation by TM_z polarization (Fig. 3.8). It can be seen that for structures with more than 5 layers there is practically no improvement of the obtained invisibility – the obtained total scattering width reduction is around 3. The main reason for such a small gain was the reflection of the incident wave from the cloak surface due to the impedance mismatch. The electric-field distribution in the vicinity of the TM_z cloak is given in Fig. 3.9, and it can be seen that the reflection from the cloak surface causes ripples in the electric-field distribution.

For the cross-polarization excitation (TE_z) the radial anisotropy of μ_r does not affect the value of calculated total scattering width. This is because the magnetic field is parallel to z-axis and thus it is zero in radial direction. Fig. 3.10 shows the angular variation of bistatic scattering width of the TM_z cloak for both polarizations. Note that the level of scattered field for the TE_z polarization is much larger than the one calculated for the TM_z polarization. Therefore the TM_z cloak is indeed unsuitable for cross-polarization excitation, as has been presumed.

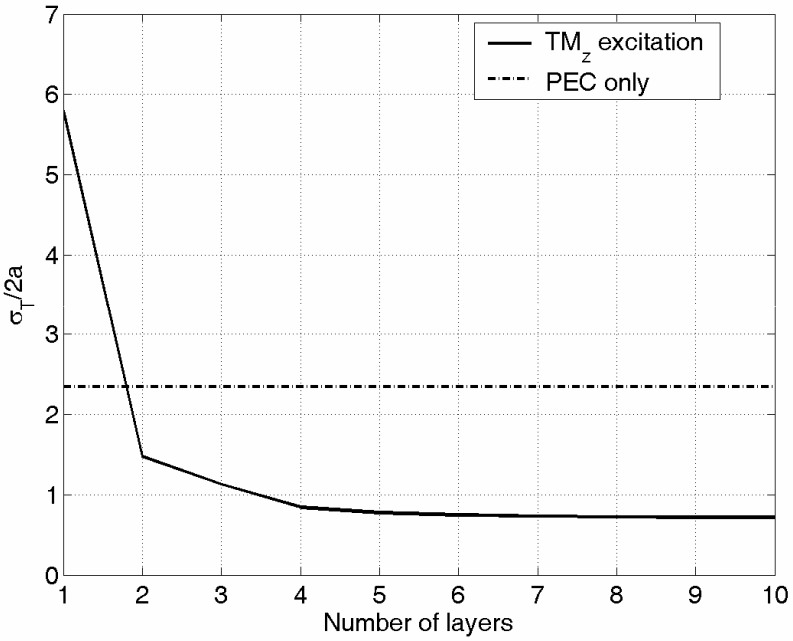

Figure 3.8. Normalized total scattering width vs. number of layers for TM_z cloak (TM_z polarization).

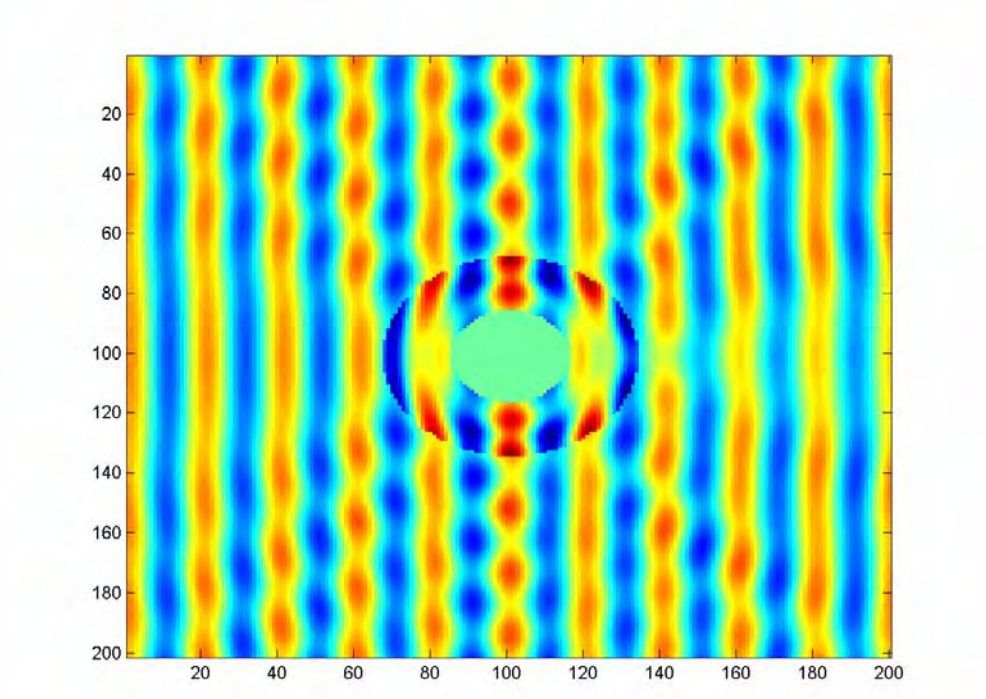

Figure 3.9. Electric-field distribution in the vicinity of the 10-layers realization of the TM_z cloaking cylinder (TM_z polarization).

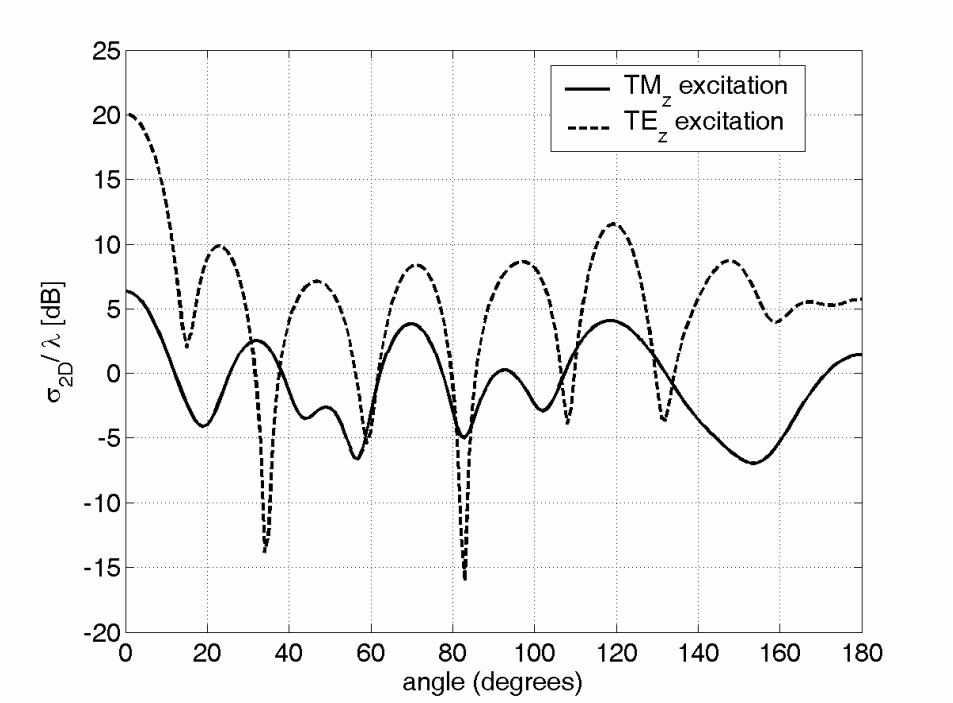

Figure 3.10. Normalized bistatic scattering width of 10-layers realization of TM_z cloaking cylinder (TM_z and TE_z polarization).

3.3.3. TE_z cloak (Cai cloak)

The TE_z cloak was designed as a completely dual cloak to the TM_z cloak described in the previous section and the metamaterial constitutive parameters were calculated by equation (3.1c). Such simplified cloak is thus designed to work only for TE_z polarization and only μ_z, ε_r and ε_φ components of the associated tensors are relevant. Complementary to the TM_z cloak, for the TE_z cloak only radial variation of the electric permittivity ($\varepsilon_r(r)$) is present. This anisotropy is also approximated with 1 to 10- steps piecewise constant functions.

The results of the simulations performed for the TE_z cloak are shown on Figs. 3.11 and 3.12. As expected, the results are complementary to the ones provided for TM_z cloak. The realized total scattering width reduction is again smaller than in the ideal case, i.e. it is around 3 for structures with more than 5 layers. As expected, the cloak is found to be suitable only for TE_z excitation.

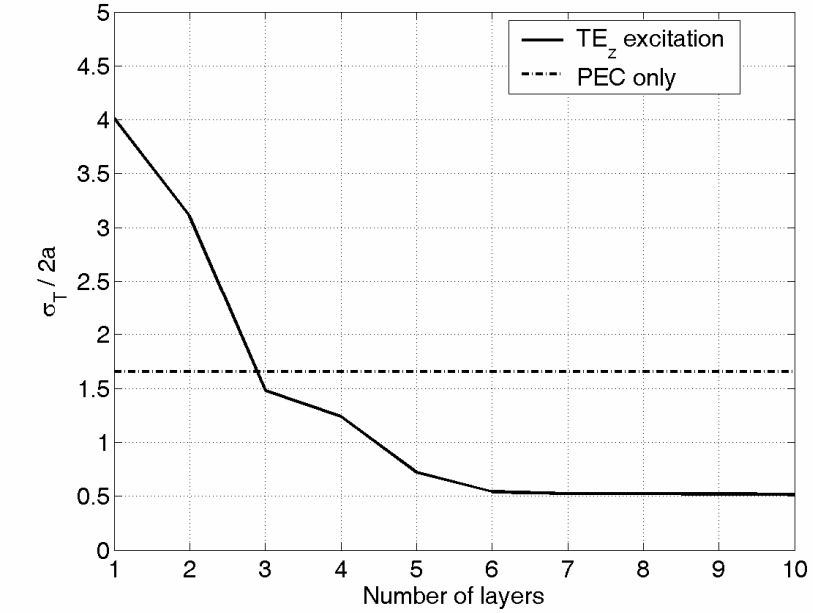

Figure 3.11. Normalized total scattering width vs. number of layers for TE_z cloak (TE_z polarization).

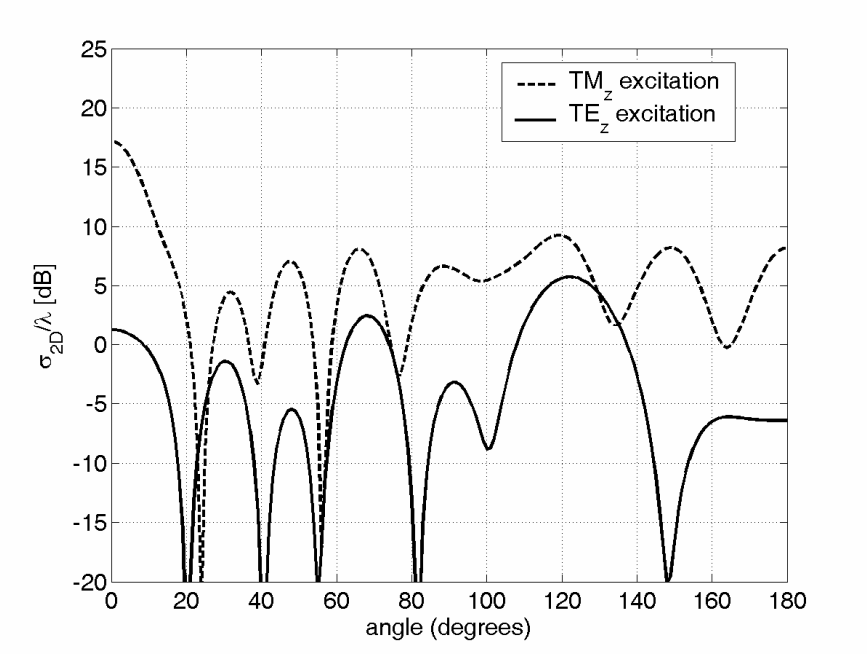

Figure 3.12. Normalized bistatic scattering width of 10-layers realization of TE_z cloaking cylinder (TM_z and TE_z polarization).

3.4. LIMITATIONS OF SIMPLIFIED CLOAK REALIZATIONS

The performed simulations show that for the simplified cloak realizations (TM_z and TE_z cloaks) the achieved total scattering width reduction is around 3, though only for one certain excitation. In reality, the magnetic permeability and the electric permittivity in metamaterials are always frequency dependent. Therefore, the frequency variations of μ and ε would have an effect on the level of achieved invisibility (see eq. 3.4 and 3.5).

The frequency dependence of the magnetic permeability (realized with some kind of split rings) is given by the so-called Lorentz model [18]:

$$\mu_{eff} = 1 - \frac{f_{mp}^{\,2} - f_0^{\,2}}{f^2 - f_0^{\,2} - j\gamma f}. \tag{3.7}$$

Here f is the frequency of the signal, f_{mp} denotes the frequency at which μ_{eff}=0 for the lossless case (null-point of the function), f_0 is the frequency at which μ_{eff} diverges (the pole of the function), while the factor γ represents the losses. In our calculations we have approximated f_{mp} by $f_{mp} = 1.02 \cdot f_0$, following the measured values of practical SRR-based metamaterials published in [18] and [19] (see Figure 3.13).

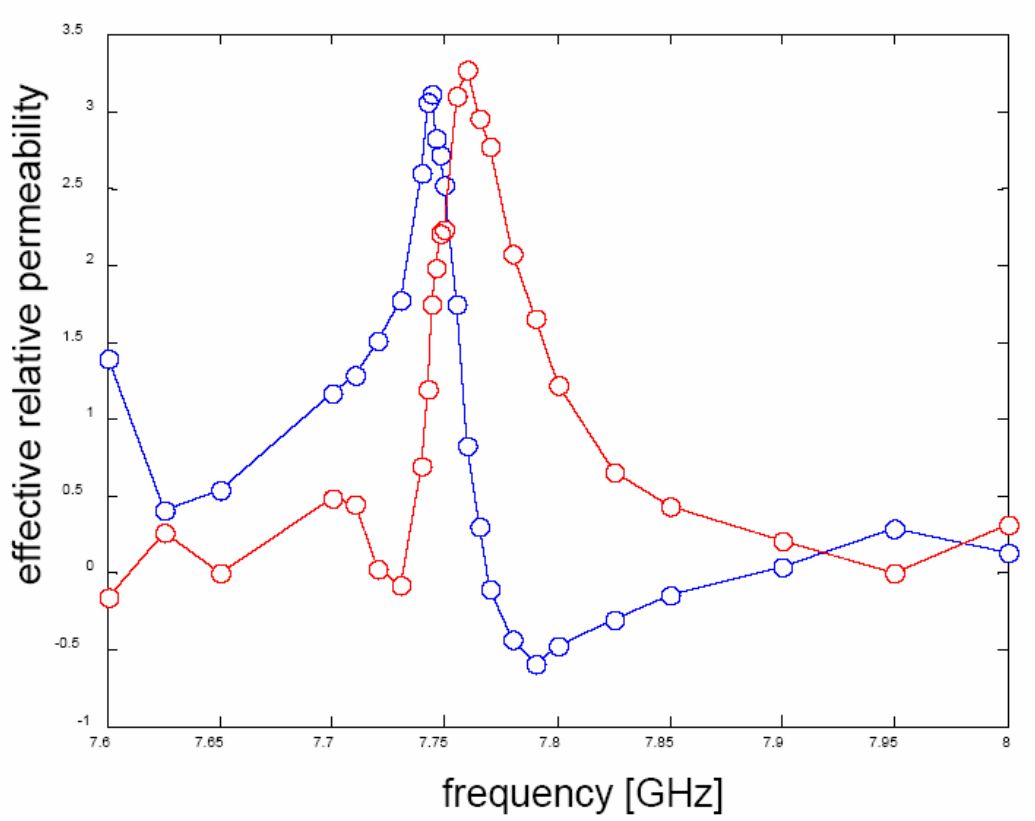

Figure 3.13. Frequency dependence of μ_r (from [18] and [19]).

On the other hand, the frequency dependence of the electric permittivity (realized with some kind of array of thin wires) is given by the so-called Drude model [18]:

$$\varepsilon_{eff} = \left(1 - \frac{f_p^{\,2}}{f^2 - j\gamma f}\right) \cdot \varepsilon_{host}. \tag{3.8}$$

Here f is the frequency of the signal and f_p represents the frequency at which $\varepsilon_{eff} = 0$ for the lossless case (null-point of the function). Factor γ represents the losses, while ε_{host} is the permittivity of the medium which is hosting the metamaterial structure.

Frequency dependencies of relative magnetic permeability and relative electric permittivity in radial direction are shown in Fig. 3.9. For simplicity, only the lossless case is being considered here (i.e. $j\gamma f = 0$).

For the central frequency f = 8.5 GHz it is assumed that the radial components of the permittivity and permeability tensors are μ_r= 0.14 (for TM_z cloak) and ε_r = 0.48 (for TE_z cloak). These are the values needed for the cloak realizations with one layer only. It is now obvious that if μ_r or ε_r throughout the structure are designed according to eq. 3.1b and 3.1c, these values can be achieved only at some certain frequency. Due to dispersion, the values of μ_r or ε_r will grow with increasing frequency. Therefore, the achieved level of invisibility will also change.

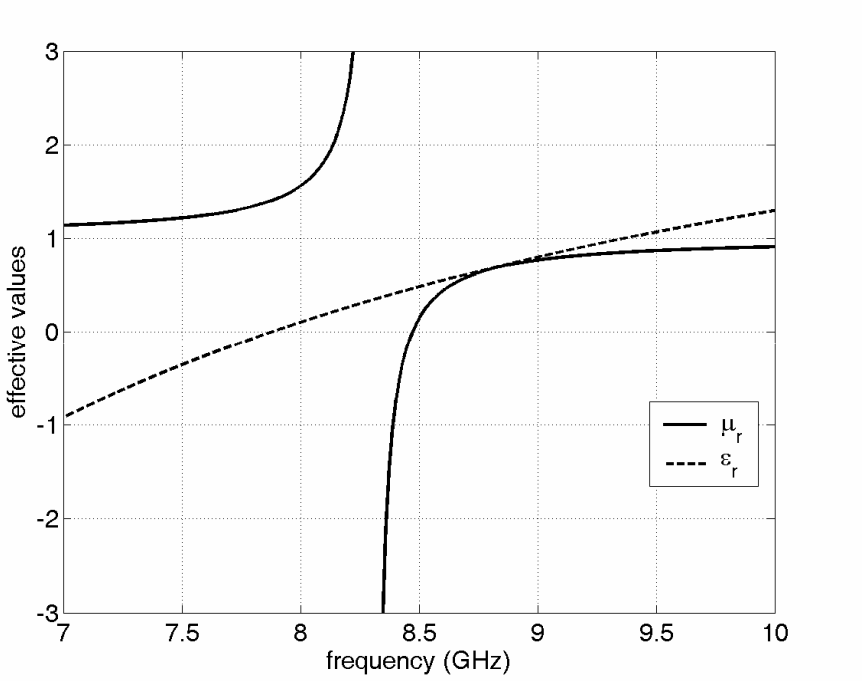

Figure 3.14. Frequency dependence of μ_r and ε_r (Lorentz and Drude model).

The simulations considered the simplified cloak realizations, in order to calculate the total scattering width with dispersion included. The cloaks were designed with ten layers of metamaterial, which is a good approximation of continuous radial change of permittivity or permeability values, as shown in section 3.2. The analysis is provided in a narrow frequency range about the central frequency (8.5 GHz), for which the values of μ_r or ε_r had been designed. Figs. 3.15 and 3.16 show the frequency dependence of the invisibility parameters for the simplified cloaks – the TM_z and TE_z cloak, respectively. The comparison with the referent case (PEC cylinder without any cloak) is also given.

We can define the bandwidth of the cloak as the frequency range (normalized to the central frequency), in which the total scattering width is smaller than the total scattering width of the hidden object (PEC cylinder in our case). It can be seen that the invisibility has been achieved only in a narrow frequency range around the central frequency (8.5 GHz). Therefore, it has also been found that the metamaterial cloak is not suitable for applications that require a larger frequency bandwidth (e.g. invisibility to radar signal). If we suppose that the cloak behaves similarly at frequencies lower than the central one, we find that the approximate bandwidths of the TM_z and TE_z cloaks are 0.02 GHz and 0.2 GHz, respectively (0.24% and 2.4 % of the central frequency). The TE_z cloak has a larger bandwidth due to the weaker frequency dependence of constitutive parameters (see Fig. 3.14).

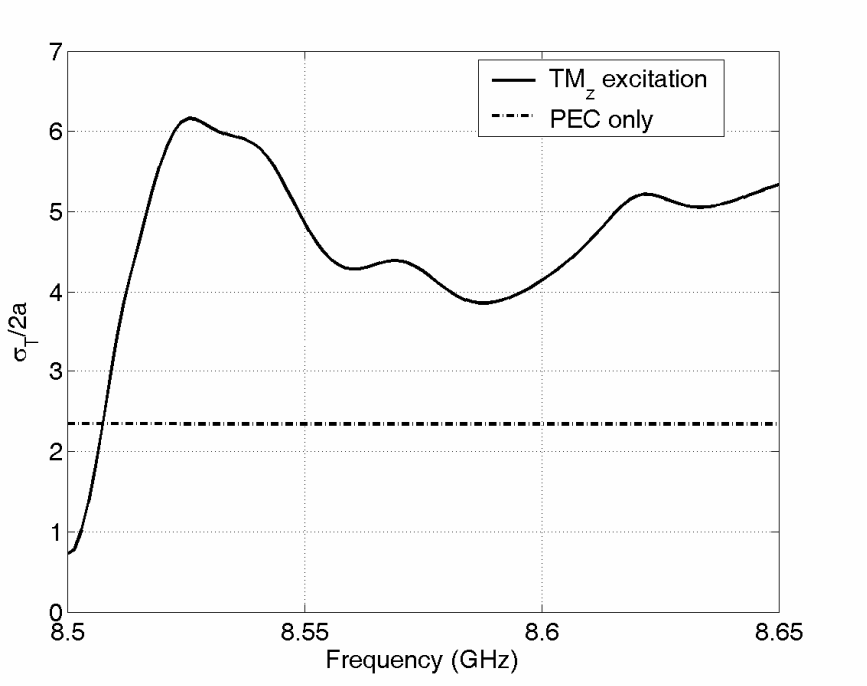

Figure 3.15. Normalized total scattering width vs. frequency for TM_z cloak with included dispersion (TM_z polarization).

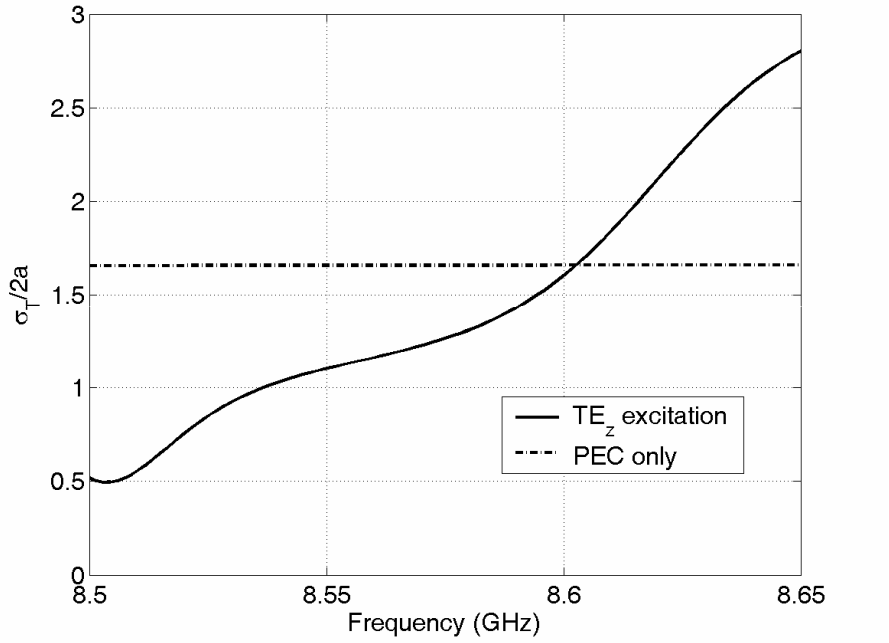

Figure 3.16. Normalized total scattering width vs. frequency for TE_z cloak with included dispersion (TE_z polarization).

The bandwidth results of the TM_z cloak strongly depend on the ratio between the frequencies f_{mp} (the frequency at which $\mu_{eff}=0$ for the lossless case) and f_0 (the frequency at which μ_{eff} diverges for the lossless case). Since this ratio depends on the particular realization of the split-ring resonator, we have investigated the dependence of the cloak bandwidth on that

ratio. In Figure 3.17 we have illustrated this dependence. It can be seen that with the ratio $f_{mp} = 1.5 \cdot f_0$ one can obtain 10 times large bandwidth, i.e. bandwidth of around 2.4 % for the TM_z polarized incident wave. However, larger ratio in practice means larger losses and worse cloak behavior (the dependence of the cloak on losses will be discussed at the end of this section). Therefore, one can conclude that if the cloak is made from resonant type of elements the bandwidth will be quite narrow.

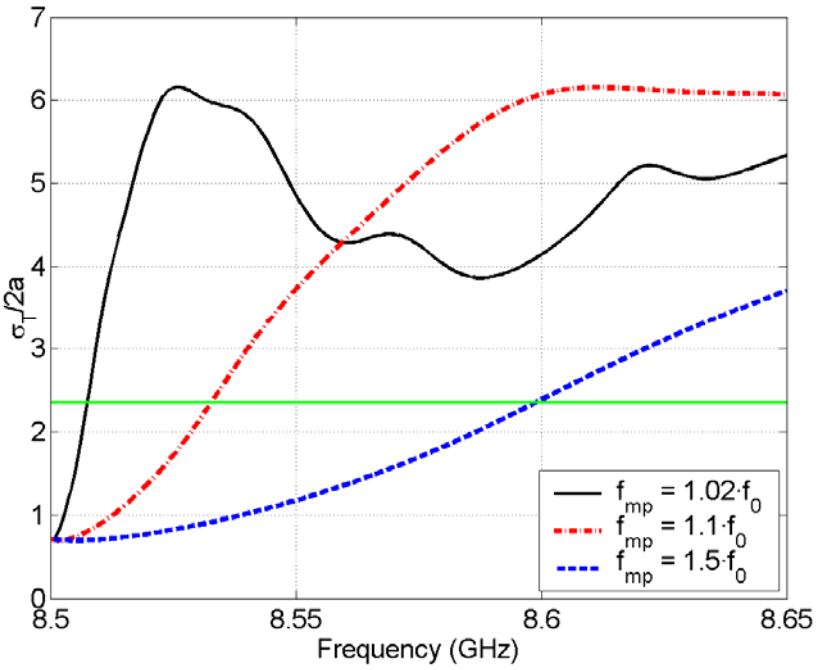

Figure 3.17. Normalized total scattering width as a function of ratio f_{mp} / f_0 for TM_z cloak (TM_z polarization).

In order to verify our bandwidth investigation (and to verify the developed code) we have compared the results calculated with the developed program and the results found in scientific literature. In [20] the bandwidth of the cloak made from elements with the Lorentz dispersion behavior was investigated. The authors have analyzed the 10-layer Schurig cloak, and they have supposed the non-uniform distribution of the f_{mp} / f_0, see table 3.1. The obtained bandwidth is around 2 %. The comparison of the total scattering width, calculated with our program and with the finite-element solver Comsol Multiphysics, is given in Fig. 3.18. The agreement with the results is very good.

The influence of losses of the periodic structure is investigated in Fig. 3.19 where the total scattering width is calculated as a function of losses (described with factor γ from equation (3.7)). It can be seen that if the value of γ is smaller than $0.001 \cdot f_0$ then the difference between lossy and lossless cases is negligible. However, for larger losses the cloak loose its cloaking behavior and it starts to behave as an absorber (i.e. the forward scattered field is drastically enlarged and the backward scattered field is reduced). That can be clearly seen in Figure 3.20 which illustrate the electric field distribution in the vicinity of the 10-layers realization of the TM_z cloaking cylinder with $\gamma = 0.01 \cdot f_0$. One can clearly see that the cloak starts to behave as a absorber resulting in strong forward scattered field.

Shell	f_{mp}	f_0	f_{mp}/f_0
1	8.4901	3.98772	2.1291
2	8.4344	4.89096	1.7245
3	8.3657	5.35577	1.5620
4	8.2953	5.63920	1.4710
5	8.2237	5.80921	1.4156
6	8.1597	5.95249	1.3708
7	8.0932	6.02870	1.3424
8	8.0336	6.09923	1.3172
9	7.9804	6.16397	1.2947
10	7.9258	6.20024	1.2783

Table 3.1. The dispersion parameters of the cloak investigated in [20].

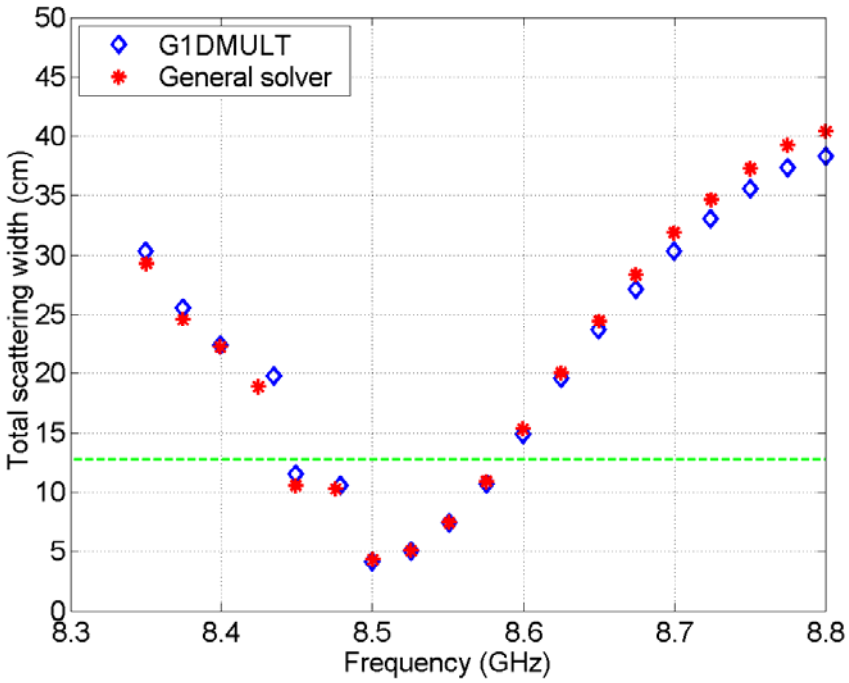

Figure 3.18. Comparison of the total scattering width calculated by the developed program (based on the G1DMULT algorithm) and by the general finite-element solver Comsol Multiphysics [20]. The dispersion parameters of the cloak are given in table 3.1.

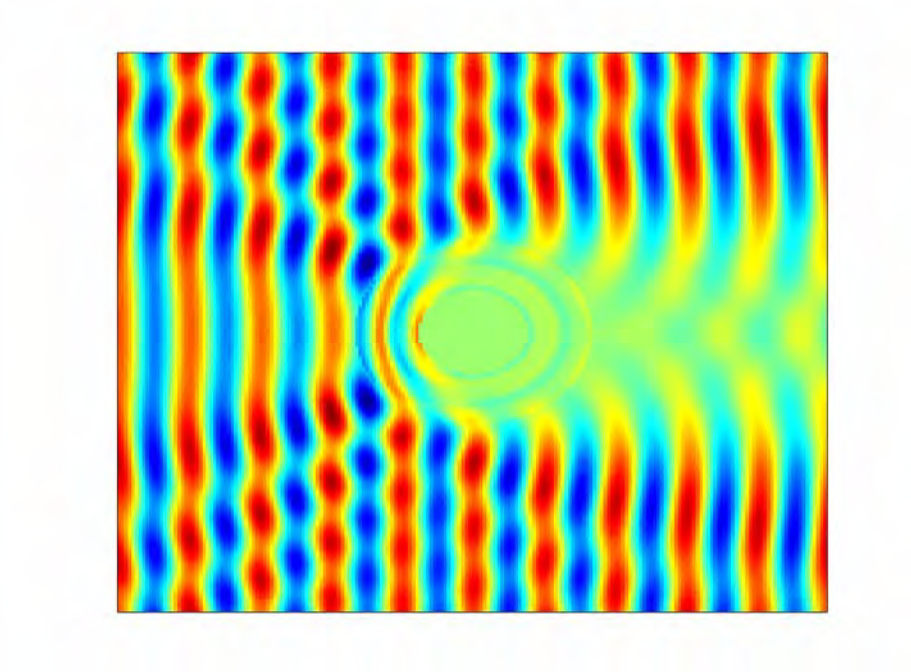

Figure 3.19. Electric-field distribution in the vicinity of the 10-layers lossy realization of the TM_z cloaking cylinder (TM_z polarization). The losses are $\gamma = 0.01 \cdot f_0$.

4 OPTIMIZATION OF UNIAXIAL MULTILAYER CYLINDERS USED FOR INVISIBLE CLOAK REALIZATION

Optimization of Uniaxial Multilayer Cylinders Used for Invisible Cloak Realization

4.1 Global optimization techniques

Global optimization is a branch of applied mathematics and numerical analysis that deals with the optimization of a function or a set of functions to some criteria. They can be formulated as a *N*-dimensional minimization problem as follows:

$$\min f(\mathbf{x}),\ \mathbf{x} = \left[x_1, x_2, ..., x_N\right], \tag{4.1}$$

where *N* is the number of the parameters to be optimized. There are many global optimization techniques available, but so far in electromagnetics only few have extensively been used. They are the genetic algorithm, the particle swarm optimization (PSO), the simulated annealing, the ant colony optimization and the multidimensional conjugate gradient method. All the global optimization techniques prove to be usable, but at this point we have concentrated on the PSO. We have chosen it since the associated algorithm is rather easy and straightforward to implement, the parameters used to tweak its performance are easily understandable, and it has the same or better performance compared to other global optimization algorithms. We have implemented three different kinds of PSO algorithm in order to compare their performance on optimization of complex electromagnetic problems, i.e. synthesis of various multilayered electromagnetic cloak designs.

4.1.1. Classical particle swarm optimization

The classical particle swarm optimization (PSO) is a robust stochastic evolutionary computation technique based on the movement and intelligence of swarms. It was initially introduced by J. Kennedy and R. C. Eberhart in 1995 [21], but in electromagnetic community it has not been extensively used until 2004 when J. Robinson and Y. Rahmat-Samii published their paper [22].

As authors [22] have conveniently put it, the PSO can best be understood through an analogy similar to the one that led to the development of the PSO. Imagine a swarm of bees in a field. Their goal is to find in the field the location with the highest density of flowers. Without any knowledge of the field a priori, the bees begin in random locations with random

velocities looking for flowers. Each bee can remember the locations that it found the most flowers, and somehow knows the locations where the other bees found an abundance of flowers. Torn between returning to the location where it had personally found the most flowers and exploring the location reported by others to have the most flowers, the ambivalent bee accelerates in both directions altering its trajectory to fly somewhere between the two points depending on whether nostalgia or social influence dominates its decision. Along the way, a bee might find a place with a higher concentration of flowers than it had found previously. It would then be drawn to this new location as well as the location of the most flowers found by the whole swarm. Occasionally, one bee may fly over a place with more flowers than had been encountered by any bee in the swarm. The whole swarm would then be drawn toward that location in additional to their own personal discovery. In this way the bees explore the field: overflying locations of greatest concentration, then being pulled back toward them. Constantly, they are checking the territory they fly over against previously encountered locations of highest concentration hoping to find the absolute highest concentration of flowers. Eventually, the bees' flight leads them to the one place in the field with the highest concentration of flowers. Soon, all the bees swarm around this point. Unable to find any points of higher flower concentration, they are continually drawn back to the highest flower concentration. In attempting to model this behavior, Kennedy and Eberhart realized that they had stumbled upon an optimizer.

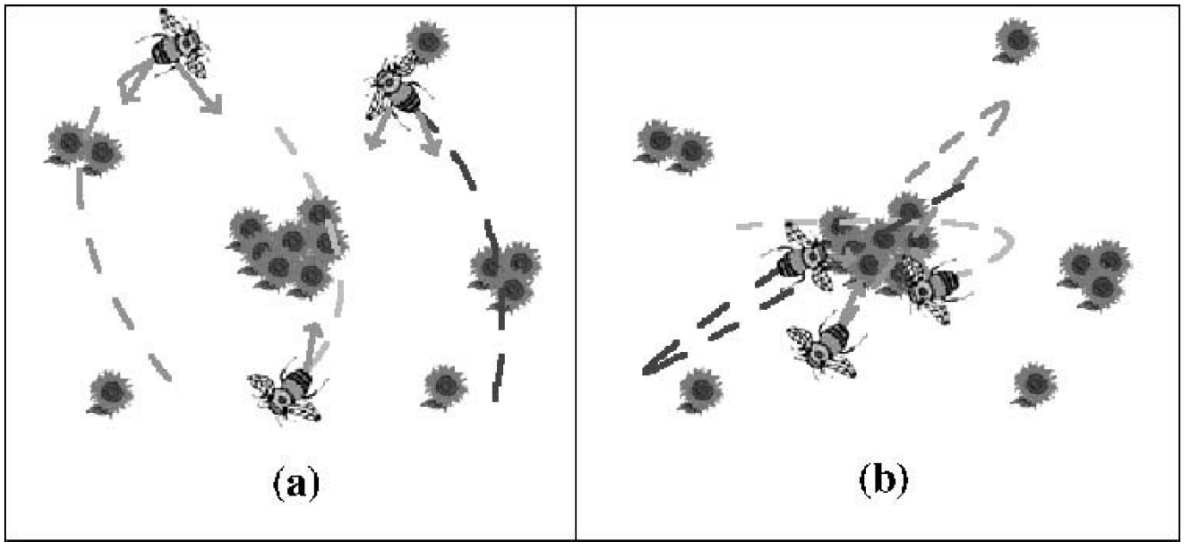

Figure 4.1. Bees in a search of field for flowers. They are attracted to location with highest concentration of flowers they have found and to the location with the highest concentration of flowers that the entire swarm has found (a). Eventually all the bees converge to the region where the highest concentration of flowers that the entire swarm has found is (b). (image taken from [22])

The language used to discuss the PSO follows from the analogy of particles in a swarm:

(1) **Particle** or **Agent**: Each individual in the swarm (bee) is referred to as a particle or agent. Particles act individually: accelerating toward the best personal and best overall location while checking the value of its current location in each time-step.

(2) **Position**: In the analogy above position is the bee's place in the field. In this case, position is represented by coordinates on the plane. In general this idea can be

extended into any *N*-dimensional space according to the problem at hand. This *N*-dimensional space is the solution space for the problem being optimized, where any set of coordinates (position vector) represents a solution to the problem. In general these can be any values needed to be optimized. Reducing the optimization problem to a set of values that could represent a position in solution space is an essential step in utilizing the PSO.

(3) Fitness: As in all evolutionary computation techniques there must be some function or method to evaluate the goodness (fitness) of a position. The fitness function takes the position in the solution space (position vector) and returns a single number representing the value of that position. In the bees searching for flowers analogy, the fitness function would simply be the flower density: the higher the density, the better the location. The fitness function provides the interface between the physical problem and the optimization algorithm. Special care has to be taken into account if multigoal analysis is carried out. More on this will be said in subsequent chapters.

(4) Personal best (pbest): In the bees analogy, each bee remembers the location where it personally encountered the most flowers. This location with the highest fitness value personally discovered by a bee is known as the personal best or pbest. Each bee has its own personal best determined by the path that it has flown. At each time-step, the bee checks if the current location has a higher fitness value and if it does, the personal best is replaced with bee's current location.

(5) Global best (gbest): Each bee also knows the highest concentration of flowers discovered by the entire swarm. This location of highest fitness encountered is known as the global best or gbest. For the entire swarm there is one global best to which all bees are attracted. At each point along their path bees compare the fitness of their current location to that of global best. If any bee is at a location of higher fitness, global best is replaced by that bee's current position.

The algorithm goes as follows:

(1) Define the solution space

When trying to optimize physical problems, one needs to select the parameters of the problem that are suitable for optimization. After selecting *N* parameters, for each parameter reasonable (physical) range in which to search for optimal solution must be given. For each dimension in an *N*-dimensional optimization X_{min} and X_{max} values have to be specified.

(2) Define fitness function

The fitness function is the link between the optimization algorithm and the physical problem that is to be optimized. The fitness function takes *N* input values (for each dimension, i.e. parameter to be optimized) and produces one single value that should unambiguous define the quality of the selected solution. In case of multi-goal analysis, weighting factors are typically introduced – so each goal can be weighted differently depending on the importance. For example, if we are trying to maximize the antenna gain while keeping low side lobe levels, the corresponding fitness function could be defined as:

$$Fitness = \alpha \cdot Gain - \beta \cdot SL(H) - \gamma \cdot SL(E). \tag{4.2}$$

Where *Gain* is the antenna gain at broadside, and *SL(H)* and *SL(E)* are the highest side lobe levels in H- and E-planes, respectively. α, β, and γ are weighting coefficients that can be adjusted to maximize the gain, or produce a beam with low side lobes. Their values could, for instance, be 1, 0.3 and 0.3, and by this way the optimizer would try to maximize the gain, but keep track of the sidelobes.

(3) Define initial particle locations and velocities

Each particle begins its search for optimal solution at a random location with a random velocity (direction and magnitude). These initial values are preselected, most often by random selection, but can also be defined according to some grid. When particle is given its initial location, personal best of each particle is calculated and updated, and among them the initial global best is selected.

(4) Run the optimization loop

The particles are systematically flown through the solution space. Each particle is moved. The movement is determined by the velocity vector. Once moved, the fitness is calculated, personal and global best are updated if the calculated fitness is greater than one remembered from before and speed is updated. The equation for updating the velocity will be defined later, but basically the velocity is determined by velocity in previous step and random influence of the distances between the current location and personal and global best positions. The loop is repeated until some stop criterion is met. The stop criterions can be many. The optimization can stop once certain fitness level is reached, if predetermined number of iterations has been carried out, or if the optimization has not improved the global best in some time. To more easily follow the optimization process a flow chart is drawn.

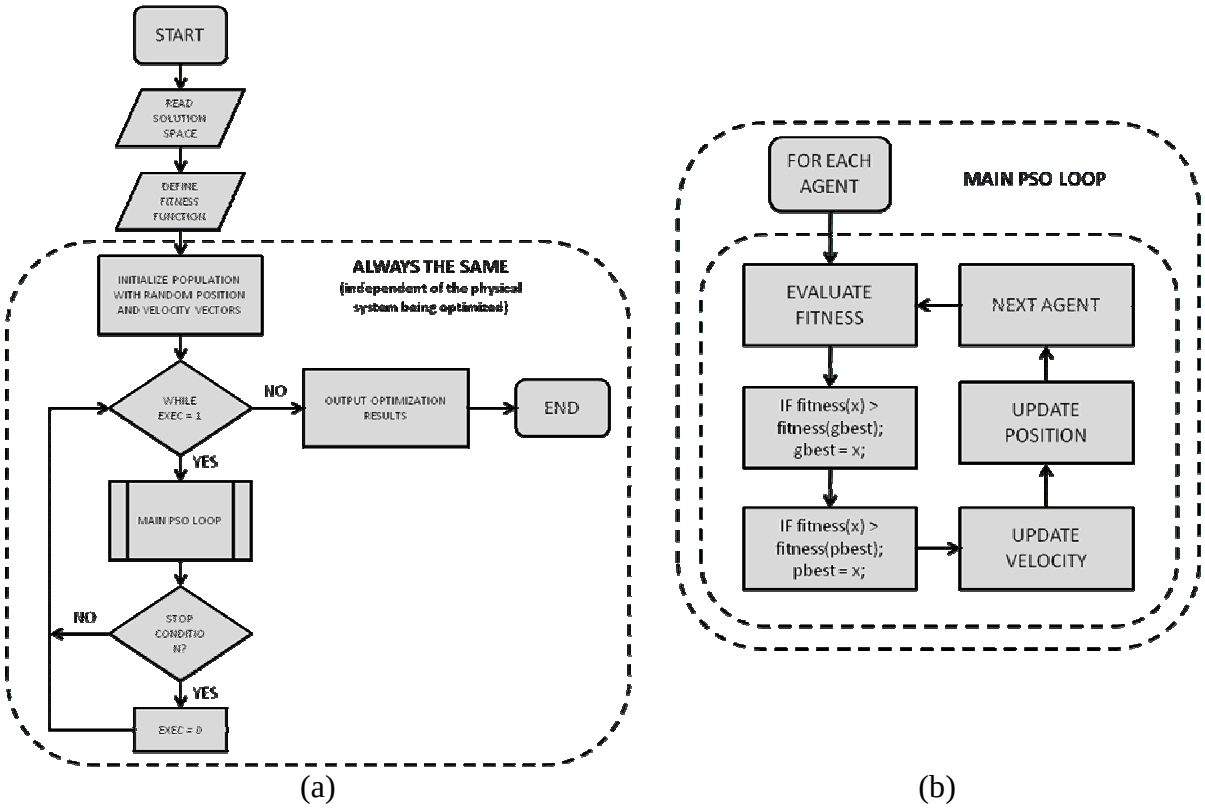

Figure 4.2. Flow chart of the PSO algorithm. (a) The whole flow chart. The part inside dashed rounded rectangle is independent of the physical system being optimized. (b) The main PSO loop

UPDATE VELOCITY

The velocity of the particle is changed according to its position relative to the locations of personal and global best. The particle is accelerated in the directions of these locations of greatest fitness according to the following equation:

$$v_n = w \cdot v_n + c_1 \cdot rand() \cdot (p_{best,n} - x_n) + c_2 \cdot rand() \cdot (g_{best,n} - x_n), \tag{4.3}$$

where v_n is the velocity of the particle in n-th dimension and x_n is the particle coordinate in the same dimension. The v_n is calculated for every dimension of the N dimensional solution space. From this equation it can be seen that new velocity is equal to old velocity scaled by the w (called the inertia factor) and increased toward the locations of personal and global best. c_1 and c_2 are scaling factors that determine the relative "pull" of personal best and global best. These are sometimes referred to as the cognitive and social rates, respectively. Increasing c_1 encourages exploration of the solution space as each particle moves toward its own personal best, while increasing c_2 encourages exploitation of the supposed global maximum. The three parameters w, c_1 and c_2 can be used to fine tune the search process. More on that will follow later. The random number function rand(·) returns a number between 0.0 and 1.0. This introduction of a random element into the optimization is intended to simulate the slight unpredictable component of natural swarm behavior, together with initialization process that varies the starting positions and velocities of the particles.

UPDATE POSITION

After particle fitness has been evaluated and velocity updated accordingly, it is time to move the particle to a new location. The velocity is applied for a given time-step Δt, usually chosen to be one and new coordinate is computed for each of the dimensions according the following equation:

$$x_n = x_n + \Delta t \cdot v_n \tag{4.4}$$

SELECTION OF PARAMETERS

Compared to some other global optimization techniques, PSO has only a couple of parameters that have to be selected prior to optimization. The goal was to develop an algorithm with an optimal balance between global exploration and exploitation of local maxima, i.e. an algorithm that would quite steadily converge, but at the same time be able to escape local extremes. The first problem was control over the search space. Without boundaries and limits on the velocities and due to the random nature, many particles would fly out of the physically meaningful solution space. This would lead to loss of time, as the algorithm would still calculate the fitness (typically computationally most expensive part of the optimization procedure) of these particles although their values as solutions where practically useless if the search space was defined properly prior to optimization start.

This problem was, at first, tackled by introduction of velocity clamping, i.e. enforcing a maximum allowed velocity called V_{max}. Most authors agreed that it is best to set V_{max} in each dimension to the dynamic range of that dimension. Second approach includes varying value of inertial weight in an attempt to strike a balance between global exploration and local exploitation. Larger values of inertial weight tend to encourage global exploration as a result of the particle being less moved by the pull of personal and global best, while with lower values particles are more rapidly attracted to the personal and global best positions. Realizing the importance of exploration early in the run, and the increasing importance of exploitation

of maxima as the run progresses, it was suggested to vary the inertial weight linearly from 0.9 to 0.4 over the course of the optimization run. For this technique to be successful, it is important to have sufficient number of iterations, so both search states could be utilized sufficiently.

Population size is another parameter that should carefully be selected. Large populations, while providing the most thorough exploration of the solution space, come at the cost of more fitness evaluations and computation time. For the PSO, previous studies claimed that relatively small population sizes can sufficiently good explore a solution space while avoiding excessive fitness evaluations. Our results show that small population is not necessarily better choice [24]. In study that we carried out while optimizing layered circular-cylindrical dielectric lens antennas we found out that sometimes it is beneficial to increase the particle count and reduce the number iterations. In this way, total number of evaluations is kept at same levels, but better optimization results can be obtained. Increasing the particle count is especially beneficiary when optimizing complex multidimensional problems. In that case, there is a high chance that the particles will be stuck in local extremes. Larger number of particles that communicate to each other are more likely to bypass this problem.

BOUNDARY CONDITIONS

The definition of the solutions space is one of the first steps carried out while preparing a specific problem to be optimized by the PSO. If the solution space is well defined, the optimization procedure will evaluate only practically realizable candidates. The question that naturally arises is: what happens when particle, by the randomness nature of its velocity, comes to the border of the solution space. To address this problem, the inventors of the PSO have imposed three different boundary conditions: absorbing, reflecting and invisible walls.

(1) Absorbing Walls: When a particle hits the boundary in one of the dimensions, the velocity in that dimension is set to zero. The particle does not stay at the boundary for long, as it is pulled back toward the allowed solution space via random nature of the velocity vector. We can say that boundary walls absorb the energy of particles trying to escape the solution space.

(2) Reflecting Walls: When a particle hits the boundary in one of the dimensions, the sign of the velocity in that dimension is changed, i.e. the particle is reflected back toward the solution space with no loss of “kinetic” energy.

(3) Invisible Walls: The particles are allowed to fly anywhere without any physical restriction, but for particles that roam outside the allowed solution space the fitness is not calculated. For nearly all engineering applications, the computationally more expensive portion of the algorithm is the fitness evaluation, so by using the invisible walls the execution time is not increased significantly. The motivation behind this technique is to save computation time by only evaluating what is in the allowed solution space, while not interfering with the natural motion of the swarm.

Most authors agree that the “invisible walls” technique provides same or slightly better results than other wall techniques. For this reason we have implemented the “invisible walls” technique in our optimization routines.

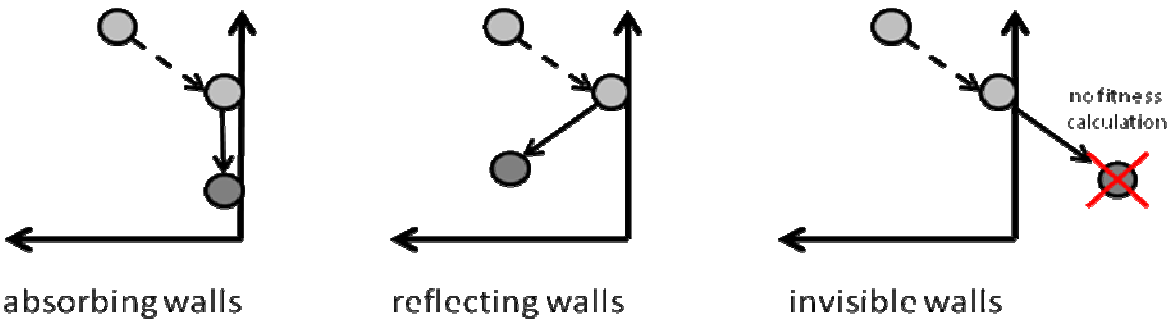

Figure 4.3. Graphical interpretation of various boundary conditions used in PSO.

4.1.2. Particle swarm optimization with local best topology

In the classical (traditional) particle swarm described above, each individual has insight to all particles present in the swarm, i.e. it knows and uses the global best solution to determine its velocity vector and consequently the trajectory by which it searches the solution space. This represents an oversimplification of the social-psychological view that individuals are more affected by those who are more successful, persuasive, or otherwise prestigious. In the human society, it is more accurate to say that the social neighborhood provides a wealth of possible models whose behavior may be emulated, and individuals seem to be affected by some kind of statistical summary of the state of their immediate social network rather than the unique performance of one individual [25]. This is the reason for introducing different neighborhood topologies.

The classical PSO algorithm outlined in previous section used a kind of topology that is known under name global best (or gbest). Each particle, in this topology, is influenced by the best performing individual in the entire population. This is equivalent to a social network where every particle is connected to every other particle. This kind of topology was acceptable, at least according to Kennedy and Mendes [25], in first applications where function landscape is largely made up of long gradients, where problem is, first, to find the best gradient region of the search space and, second, to find the extreme of that region.

Many problems, including the one studied here (synthesis of various multilayered electromagnetic cloak designs), contain cliffs, variable interactions and other features that are not typified by smooth gradients – for this kind of problems, a more robust algorithm is needed, at least according to [25]. A new topology, termed local best (or lbest) was proposed in order to deal with these, more difficult, problems.

In local best topology, the subpopulations can search diverse regions of the problem space. One part of the population can concentrate on one local optimum, while other part can search around different local optimum. The flow of information between particles is slowed down, and that can prevent premature convergence from happening. Further tweaking of the search can be made by varying the size of local neighborhood, i.e. the number of particles that each particle communicates to.

To summarize, the global best topology (i.e., the biggest neighborhood possible) often converges more quickly compared to the local best topology, but at the same time it is also more susceptible to the attraction of local optima since the population rushes unanimously

toward the first good solution found. In our optimizations, we have typically set the size of the swarm at 100, following the reasoning brought forward in previous section, while the local neighborhood was set at 5 and was defined during the first evaluation based on normalized distance between particles.

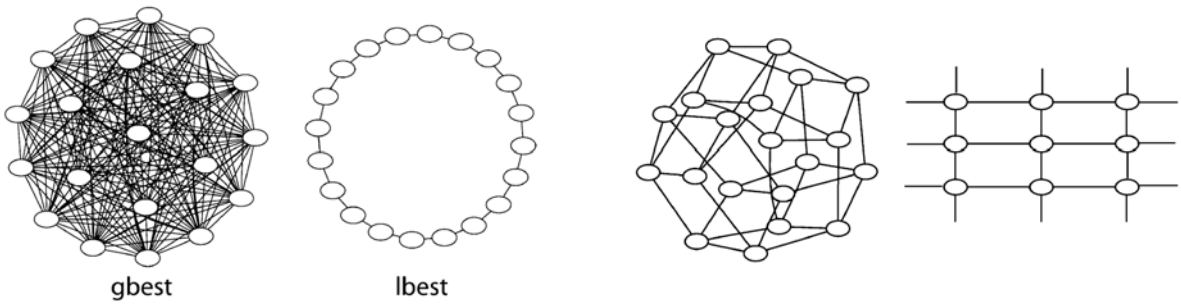

(a) (b)

Figure 4.4. Different types of topologies. (a) comparison between gbest topology used in classical PSO (every particle connects to all others) and one version of lbest topology where each particle is connected to two neighbors (b) von Neumann or square topology – each individual is connected to four other particles (above, below and on both sides, with wrapped edges) (image taken from [25])

4.1.3. Comprehensive learning particle swarm optimization

A variant of the PSO called the comprehensive learning particle swarm optimization uses a novel learning strategy in which all other particles' historical best information is used when updating particle's velocity. This strategy should enable the diversity of the swarm to be preserved and, in the end, discourage premature convergence.

There are numerous proposed variants of the PSO, but almost all of them suffer to some extent from main deficiency of the PSO – premature convergence when solving multimodal problems. The reason is to be found in the velocity equation for the classical PSO. All the particles learn from global best even if the current global best is far from the global optimum. For that reasons, the particles get attracted to the global best region and can get trapped in local optimum, if the problem to be optimized is complex with numerous local extremes. One deficiency of the classical approach is outlined in [26]: the fitness value of a particle is determined by all *N* parameters, and a particle that has discovered the region corresponding to the global optimum in some dimensions may have a low fitness value because of the poor solutions in the other dimensions. In order to make better use of this information, the authors have proposed a new learning strategy – all particles personal bests are used to update the velocity of any one particle. The velocity equation is changed as follows:

$$v_n^i = w \cdot v_n^i + c \cdot rand() \cdot (pbest_n^{f_i(n)} - x_n^i) \tag{4.5}$$

where $\mathbf{f}_i = [f_i(1), f_i(2), ..., f_i(N)]$ defines which particles' personal best the particle *i* should follow. $pbest_n^{f_i(n)}$ can be the corresponding dimension of any particle's personal best including its own, and the decision depends on the probability P_c called the learning probability which can take different values for different particles. The choice is made as follows. For each

dimension of each particle a random number is generated. If this random number is larger than P_{ci}, the corresponding dimension will learn from its own personal best, otherwise it will learn from another particle's best. As a selection procedure for the case the random number is smaller, tournament selection procedure is used. Two random particles (excluding the one whose velocity is to be updated) are chosen and their fitness values are compared. The better particle is a winner and its personal best is used as the exemplar to learn from for that dimension. There is one more addition. If all exemplars of a particle are its own personal best, one dimension is randomly chosen to learn from another particle's personal best. In order to ensure that a particle learns from good exemplars and to minimize the time wasted on poor directions, we allow the particle to learn from the exemplars until the particle ceases to improve for a certain number of generations called the refreshing gap $m - f_i$ is then reassigned for the particle.

According to authors [26] there are three main differences between the CLPSO and the original PSO. Instead of using only personal best and one global best as the exemplars, all particles' personal best can potentially be used. Furthermore, instead of learning from the same exemplar particle for all dimensions, each dimension of a particle in general can learn from different personal bests for different dimensions for a few generations. Finally, instead of learning from two exemplars at the same time, each dimension of a particle learns from just one exemplar for a few generations. These three changes increase the swarm's diversity and allow improved performance when solving complex multidimensional problems. This is explained as follows. In classical PSO, if the personal and global best for a specific dimension are on the opposite sides of the particle's current position – the particle may oscillate. However, the global best is more likely to provide a larger momentum as distance between the current particle position and global best position is likely to be larger than distance to personal best. From these reasoning it is evident that global best may influence the particle to move toward it even if it is in a local optimum region that can be far from the global optimum. If both personal and global best are on the same side in specific dimension compared to particle current position, the particle will move in that direction and it may be impossible to jump out of the local optimum area once particles personal best falls into the same local optimum region where the global best is. In case of CLPSO, the particle can fly in other directions by learning from other particles' personal best. Furthermore, as each particle's personal best is possibly a good area, the CLPSO is neither blind, nor random.

CLPSO introduces one new parameter called learning probability P_c. Question naturally arises: what is the optimal value of P_c. Studies have showed that different values of learning probability yield similar results on simple unimodal problems while seriously affecting the CLPSO performance on multimodal problems. In order to address the problem in a general manner, learning probability is typically varied between particles. In this way particles have different levels of exploration and exploitation ability and the algorithm is more suitable for solving diverse problems. The following expression was developed in order to set the P_{ci} for each particle.

$$P_{Ci} = 0.05 + 0.45 \times \frac{\left(\exp\left(\frac{10(i-1)}{ps-1} \right) - 1 \right)}{\left(\exp(10) - 1 \right)} \tag{4.6}$$

In this way the learning probability between particles ranges from 0.05 to 0.5 as shown below.

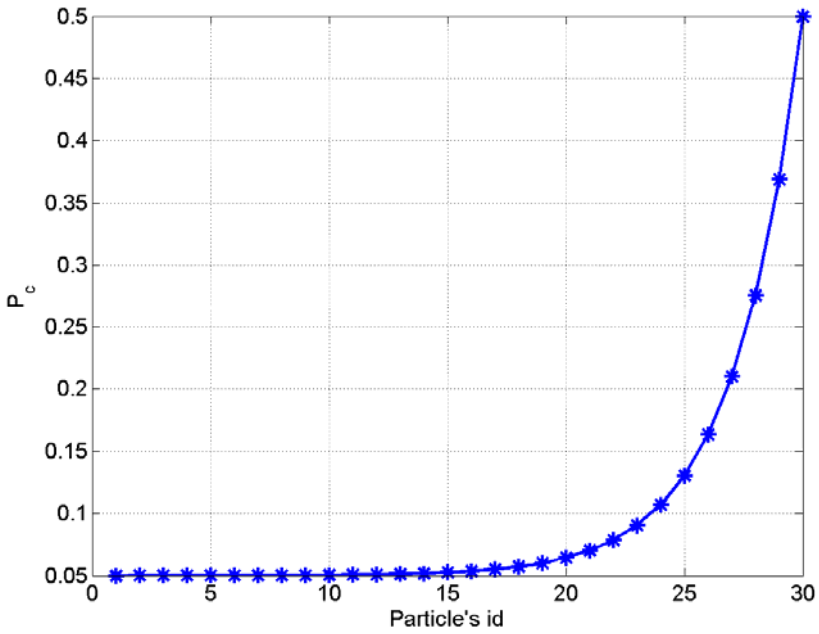

Figure 4.5. Learning probability P_c for each particle for a swarm size of 30.

4.1.4. Performance comparison

For the classical PSO we have used parameters very close to one recommended in [22]. Boundaries are left open (invisible walls), and no fitness is calculated outside. The inertial weight w decreases linearly from 0.9 to 0.4 during one optimization run, and the values of c_1 and c_2 are fixed at 1.5. In contrast to the recommendations for classical PSO, our results suggest that increasing the particle number can provide better results since the search space can be relatively large. Therefore, in the optimizations where the classical PSO has been used, the population size was typically increased to at least 100. For the modified classical PSO with local best topology [25] we clamped the velocities. The local neighborhood was typically set at 5 and was defined during first evaluation based on normalized distance between particles. In the case of CLPSO, the number of particles was keep at reasonable small number (around 40), but number of evaluations was set at much higher values in the range of 30,000 or more. The refreshing gap m was set at 7 following advice given in [26]. The mentioned steps were practical to implement, as the developed analyzing kernels were very fast, typically needing less than a second to estimate the required parameters of the structure. It should be noted that all algorithms have been able to obtain similar fitness values for most cases, so it is reasonable to assume that local extremes have largely been avoided. Details about typically used swarm parameters are summarized in Table 4.1.

	Classical PSO	**Local PSO**	**CLPSO**
Parameters			
number of particles	N_p = 100	N_p = 100	N_p = 40
maximum velocity	V_{max}: none	V_{max}: 0.5	V_{max}: none
minimum velocity	V_{min}; none	V_{min}; 0.0001	V_{min}; none
cognitive ratio	c_1 = 1.5	c_1 = 1.5	c_1 = 1.5
social ratio	c_2 =1.5	c_2 =1.5	c_2 =0
inertia weight	linearly decreasing *w*: 0.9 → 0.4	linearly decreasing *w*: 0.9 → 0.4	linearly decreasing *w*: 0.9 → 0.4
Properties			
neighborhood	entire swarm	local swarm (5)	entire swarm
solution space	$[min, max]^K$	$[0,1]^K$	$[min, max]^K$
boundary conditions	invisible wall	invisible wall	invisible wall

Table 4.1. Particle swarm optimization parameters

Fitness (lower is better, 10 layer, γ defines losses)			
	Classical PSO	**Local PSO**	**CLPSO**
γ = 0	0.009676	0.009004	0.009062
γ = 0,00001	0.416432	0.314898	0.314893
γ = 0,001	4.385527	4.385527	4.385527
γ = 0,01	9.409631	8.527133	9.409251

Table 4.2. Fitness values obtained for cloak with 10-layers with various losses

Fitness (lower is better)		
No. of layers	**Local PSO**	**CLPSO**
7	1.163527	1.168191
8	0.551858	0.551849
9	0.328954	0.328936
10	0.009004	0.009062
12	0.000966	0.001020

Table 4.3. Fitness values obtained for lossless cloak with different number of layers

4.2 Optimized cloak

Recently, several research groups investigated optimization of cylindrical cloaks. However, they have used either fully anisotropic materials [27] (with no indication how to practically realize it in microwave frequency range), or they have optimized cloaks for optical or infrared range of frequencies [28] where the permittivity smaller than one can be obtained using plasmonic materials (e.g. isotropic materials can be obtained using the noble metals, polar dielectrics or some semiconductors) or composite materials obtained by properly embedding metallic nanoparticles and nanowires into dielectric background. However, in microwave frequency region the obtained structures with permittivity smaller than one are anisotropic. Therefore, we have concentrated our investigation on the cloaks in microwave frequency region that can be obtained relatively easily using periodic structures that change constitutive parameters in only one direction. All the presented results are for Schurig-type of cloaks, i.e. for cloaks that have only radial component of permeability that varies along the radial direction. Similar results can be obtained for TE cloaks with only radial component of permittivity that is a function of radial coordinate.

Using the developed PSO algorithm we have optimized the relevant constitutive parameters (μ_r and ε_z) of each layer of the circular-cylindrical cloak, in order to obtain a cloak that does not scatter the electromagnetic field at the central frequency, i.e. the "perfect" cloak at normal incidence. It should be noted that such a "perfect" cloak is designed with the assumption of lossless metamaterial ($\gamma = 0$). The calculated relevant constitutive parameters of the Schurig cloak and the optimized cloak are given in Table 4.4. The considered number of layers is 10, i.e. both the Schurig cloak and the optimized cloak consist of the same number of layers. The layer no. 1 represents the innermost layer while the layer no. 10 is the outermost one. The level of complexity of the construction of the optimized cloak is the same as in the construction of the Schurig cloak (if needed, the interval of obtainable permeability values can be easily adjusted in the optimization process if some of the values of μ_r cannot be obtained in the practical cloak realization). However, the physical insight into wave propagation through the optimized cloak is lost. The calculated total scattering width of the optimized cloak, together with the comparison to the original Schurig cloak, is given in Fig. 4.6. The results are given in a narrow frequency range above the central frequency (8.5 GHz), since the cloak behaves quite symmetrically for frequencies lower than the central one. The invisibility gain is simply obtained by dividing the total scattering widths of the referent case (PEC only) and the case with the cloak present. It is evident that by using the optimization process it is possible to design a virtually invisible cloak with the obtained invisibility gain of about 1,400 (although the physical insight of the cloak is lost). Note that the bandwidth of the optimized cloak is reduced even more, compared to the Schurig cloak. While in the Schurig cloak the estimated invisibility bandwidth is approximately 0.2%, for the optimized cloak the bandwidth is only about 0.08%.

The angular variation of the bistatic scattering width (σ_{2D}) has been calculated at the central frequency just to check if there is any direction with distinctively stronger scattered field (Fig. 4.7). As can be seen, the scattered field of the optimized cloak is around 20 dB lower than that of the Schurig cloak.

Layer No.	**Schurig cloak**	**Optimized cloak**	**Optimized cloak (γ = 0.0003)**
	ε_z =3.431; μ_ϕ =1.0	ε_z =3.858; μ_ϕ =1.0	ε_z =3.813; μ_ϕ =1.0
	μ_r	μ_r	μ_r
1	0.003	0.056	0.020
2	0.022	0.025	0.016
3	0.051	0.010	0.020
4	0.085	0.092	0.078
5	0.119	0.587	0.192
6	0.154	0.046	0.068
7	0.187	0.216	0.193
8	0.219	0.999	0.500
9	0.249	0.076	0.093
10	0.278	0.616	0.503

Table 4.4. Relevant constitutive parameters of the Schurig cloak and the optimized cloaks

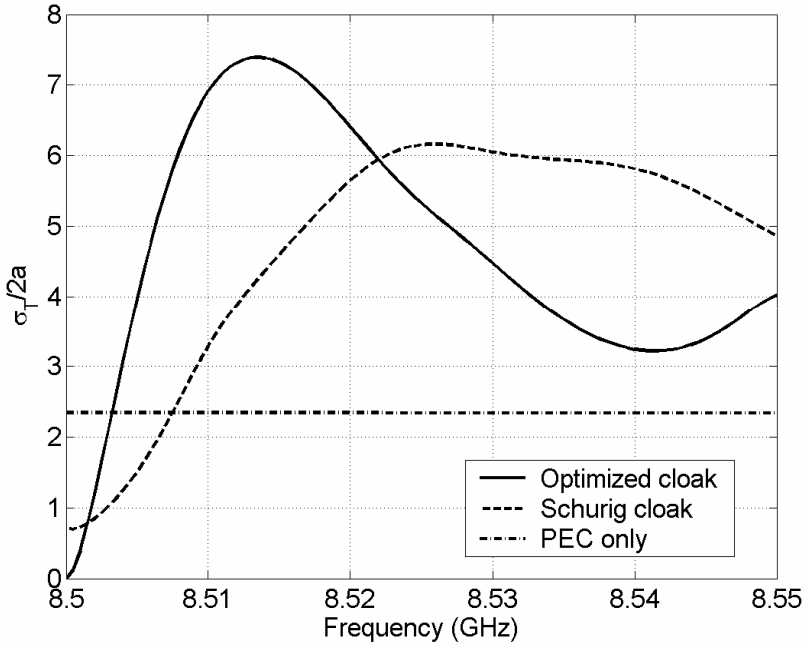

Figure 4.6. Normalized total scattering width vs. frequency for the Schurig cloak and the invisibility gain – optimized cloak. The constitutive parameters of both cloaks are given in Table 4.4

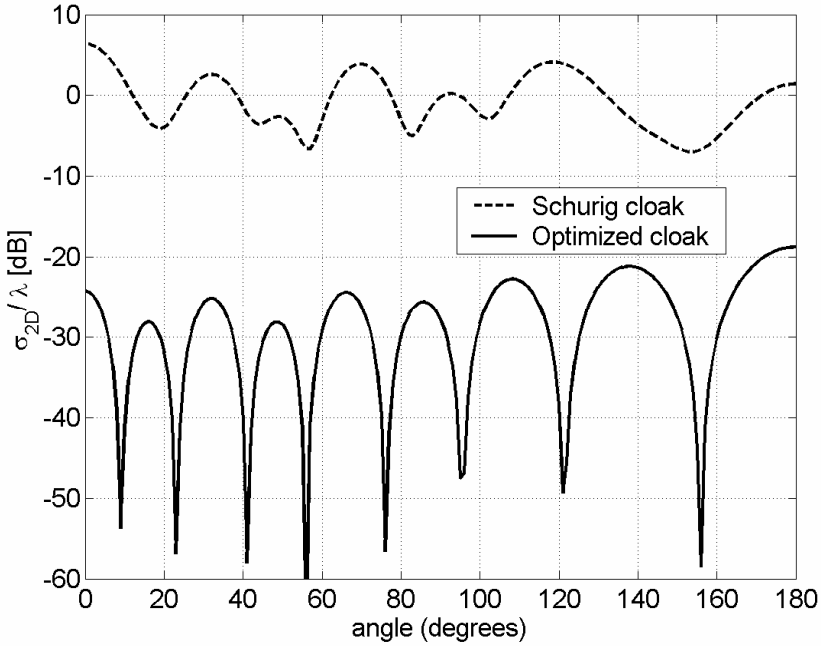

Figure 4.7. Normalized bistatic scattering width of the considered cloak realizations at the central frequency (8.5 GHz). The constitutive parameters of both cloaks are given in Table 4.4

4.2.1. Number of layers

The Schurig cloak consists of ten metamaterial layers, which is the starting point of our study. Here we shall study how the number of layers in the cloak, i.e. the subtlety of the approximation of radial permeability, relates to the level of invisibility obtained by optimization. All the results have been obtained by PSO optimization, keeping the total dimensions of the cloak intact (i.e. the inner and outer radii). From Fig. 4.8 it can be seen that the normalized total scattering width decreases as the number of layers increases. It is interesting to note that better invisibility performance than with the Schurig cloak (that has $\sigma_T/2a = 0.717$) can be obtained with only three metamaterial layers. Also, it should be stressed that the level of achieved invisibility is significantly increased once the tenth layer is added. With ten layers the cloak becomes practically invisible, although only at a single frequency.

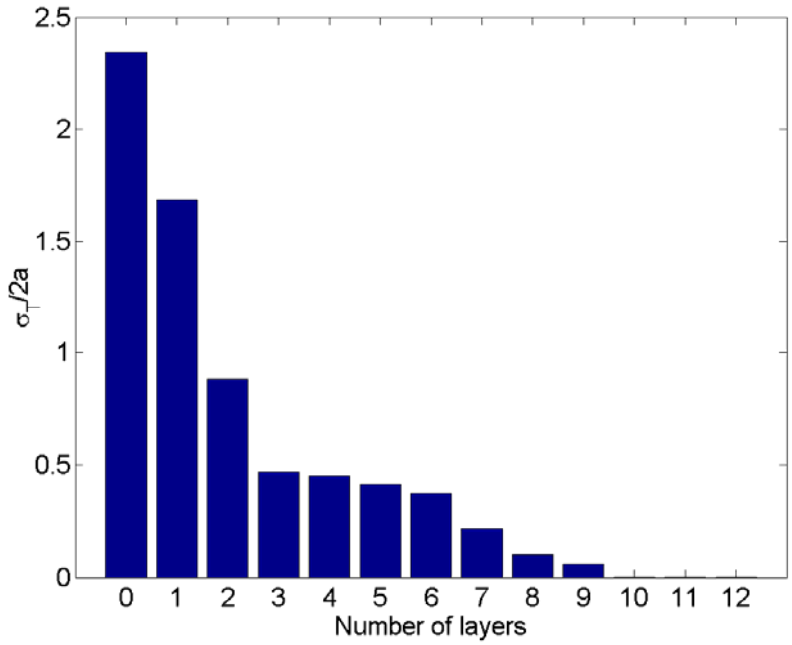

Figure 4.8. Normalized total scattering width vs. number of layers for a cloaked cylinder with 1.5 λ diameter. The parameters of layers where optimized with PSO at a single frequency of 8.5 GHz.

We have also investigated how the radius of the cylinder that we would like to cloak influences the needed number of cloak layers. The considered cylinder in Schurig case had ~ 1.5 λ diameter. In Fig. 4.9 we have investigated the cylinder with 1.0 λ diameter (at central frequency 8.5 GHz), while the ratio of the outer and inner cloak radius was kept the same (i.e. the considered radii are a = 1.765 cm and b = 3.836 cm). It is interesting to note that with the reduction of the cloaked cylinder radius the needed number of layers in order to obtain "the perfect cloak" is also reduced, and in this case one needs only 7 layers to obtain invisibility gain more than 1000.

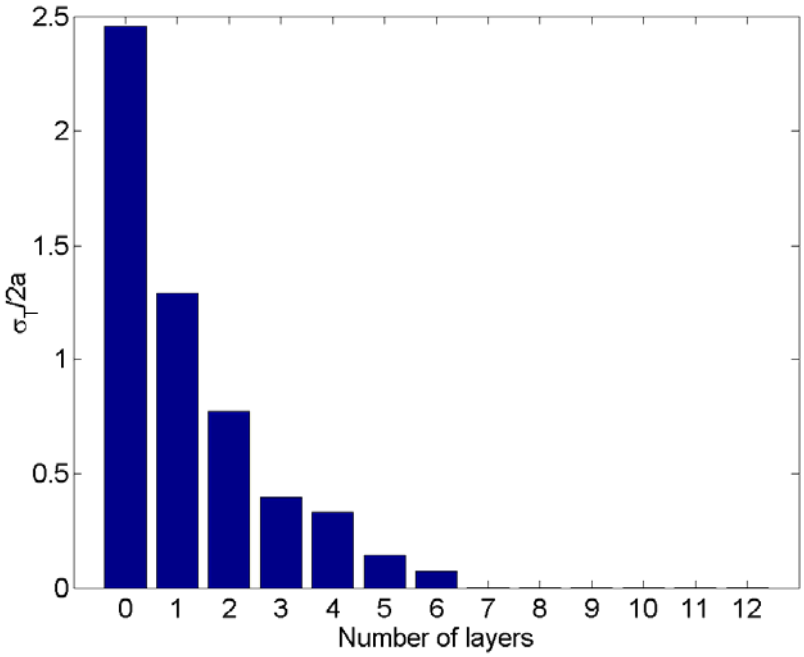

Figure 4.9. Normalized total scattering width vs. number of layers for a cloaked cylinder with 1.0 λ diameter. The parameters of layers where optimized with PSO at a single frequency of 8.5 GHz.

4.2.2. Losses and tolerance

In addition, we have estimated the influence of losses in the material on the maximum achievable invisibility gain. We have started from the lossless cloak and gradually increased losses running the optimization procedure for all the considered values of γ independently. The losses are described with factor γ in

$$\mu_{eff} = 1 - \frac{f_{mp}^{\ 2} - f_0^{\ 2}}{f^2 - f_0^{\ 2} - j\gamma f}. \tag{4.7}$$

As expected, the total scattering width increases (and therefore the obtained invisibility gain decreases) as the losses increase (see Fig. 4.10). It has also been found that the losses of $\gamma = 10^{-3} f_0$ are still acceptable, for the invisibility gain of the optimized lossy cloak has fallen to approximately the same value as the invisibility gain of the lossless Schurig cloak (around 3). In the same figure we have plotted the influence of material losses on the bandwidth of the cloak (i.e. the frequency range where invisibility gain is larger than 1). It can be seen that the bandwidth increases with the introduction of the losses, while at the same time the maximum invisibility gain is reduced.

Furthermore, sensitivity of the optimal solution to construction tolerances has been tested. We have run statistical analysis to estimate how much the variation (as a result of construction tolerances) of the values of the radial component of permeability tensor μ_r and of permittivity ε_z influences the obtained total scattering width. Fig. 4.11 shows the mean value of total scattering width if μ_r and ε_z are varied randomly by 0% to 5% of their initial (ideal)

value with uniform distribution (worst case). Two cases are shown - with and without losses. It can be seen that the cloak is not too sensitive to parameter tolerances and lossy cloaks are even less sensitive. We can conclude that cloaks that are quite invisible can be realized even with reasonably large parameter variances. The cloak with small losses is also easier to realize in practice since the variation of parameters is much smaller, i.e. all the values of radial permeability lie in range from 0 to 0.5 (Table 4.4, column 3), so the design could proceed as in [14].

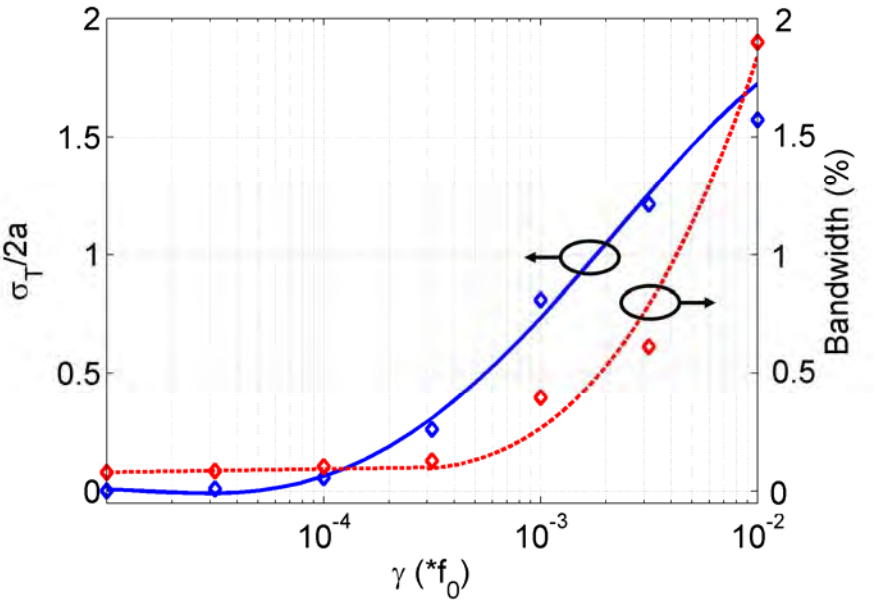

Figure 4.10. Dependence of obtained total scattering width and bandwidth on losses for the invisibility gain – optimized cloak.

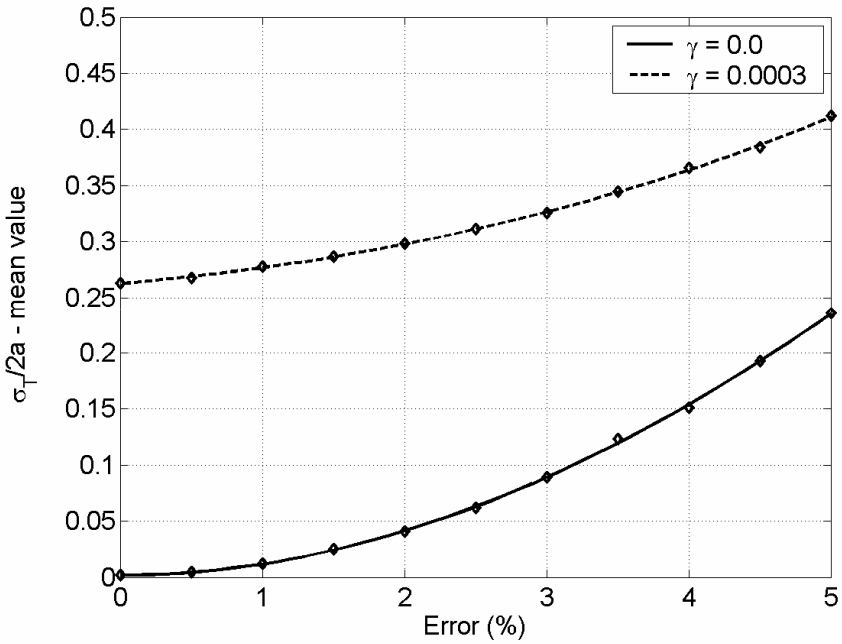

Figure 4.11. Dependence of obtained total scattering width on construction tolerances for the invisibility gain – optimized cloak. The mean value of total scattering width is shown.

4.2.3. Bandwidth - optimized cloak

We have also investigated the possibility of enlarging the bandwidth of the cloak while keeping the same level of the invisibility gain (i.e. the minimum of the total scattering width) as the one of the Schurig cloak. Two cases have been considered – the optimization of the lossless cloak ($\gamma = 0$) and the optimization of the lossy cloak with small losses of $\gamma = 10^{-3} f_0$, which have been shown to be still acceptable. The calculated total scattering widths are shown in Figs. 4.12 and 4.13, respectively. The comparison with the Schurig cloak (lossless and lossy, respectively) is also given. The optimized bandwidth is around 0.4% for the lossless case and about 0.58% for the lossy case. Meanwhile, the Schurig cloak exhibits bandwidths of 0.2% (lossless case) and 0.24% (lossy case). In other words, the improvement in the bandwidth compared to the Schurig cloak is between 2 and 2.5 in both considered cases.

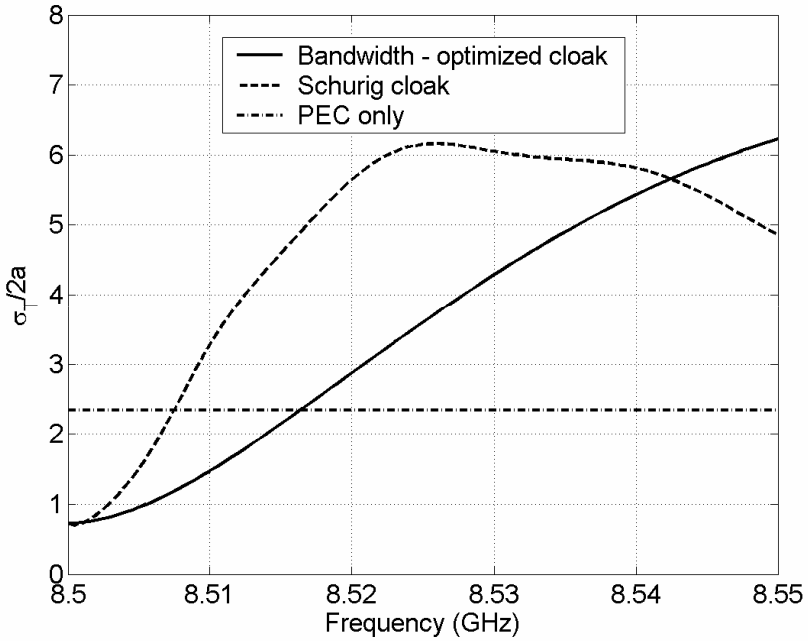

Figure 4.12. Normalized total scattering width vs. frequency for the Schurig cloak and the bandwidth optimized cloak. Lossless cloaks are considered ($\gamma = 0$).

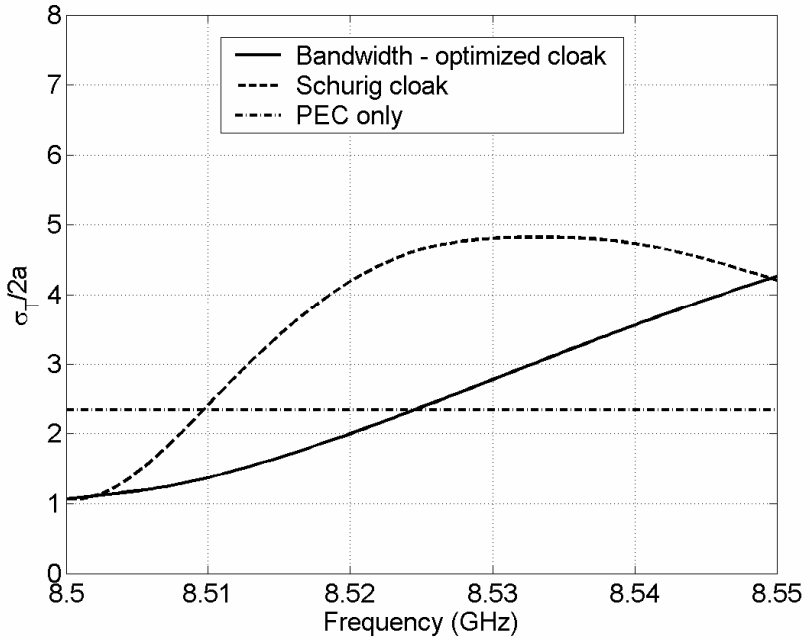

Figure 4.13. Normalized total scattering width vs. frequency for the Schurig cloak and the bandwidth optimized cloak. Lossy cloaks are considered ($\gamma = 10^{-3} f_0$).

4.2.4. Three layers cloak

Fig. 4.8 shows the minimum total scattering width that is possible to obtain by respective number of metamaterial layers (the goal of optimization in that optimization). It can be seen that the normalized total scattering width decreases as the number of layers increases. From section 4.2.1 it also follows that by using optimization it is possible to achieve better invisibility performance than with the Schurig cloak (that has $\sigma_T / 2a = 0.717$) by employing only three metamaterial layers. As 3-layers cloak is undoubtedly more convenient to produce in practice, it is obviously interesting to provide study of the three layer cloak design and performance in more details. The results of the three layer optimization are summarized in Table 4.5.

Layer No.	**Optimized cloak**
	ε_z =3.841; μ_ϕ =1.0
	μ_r
1	0.021
2	0.123
3	0.218

Table 4.5. Relevant constitutive parameters of the 3-layer cloak

The obtained relative permeability values are reasonably easy to obtain in practice, making realization of such cloak possible by means of split ring resonators. The dispersion of 3-layers cloak was also taken into account and modeled by Lorentz model. In Fig. 4.14 frequency dependence of total scattering width of 3-layers cloak is given, as well as the comparison with Schurig cloak (which is ten-layered). The results are given in a narrow frequency range above the central frequency (8.5 GHz), since the cloak behaves quite symmetrically for frequencies lower than the central one. Obviously by significantly smaller number of layers similar results have been obtained (the invisibility gain was slightly improved at the expense of bandwidth).

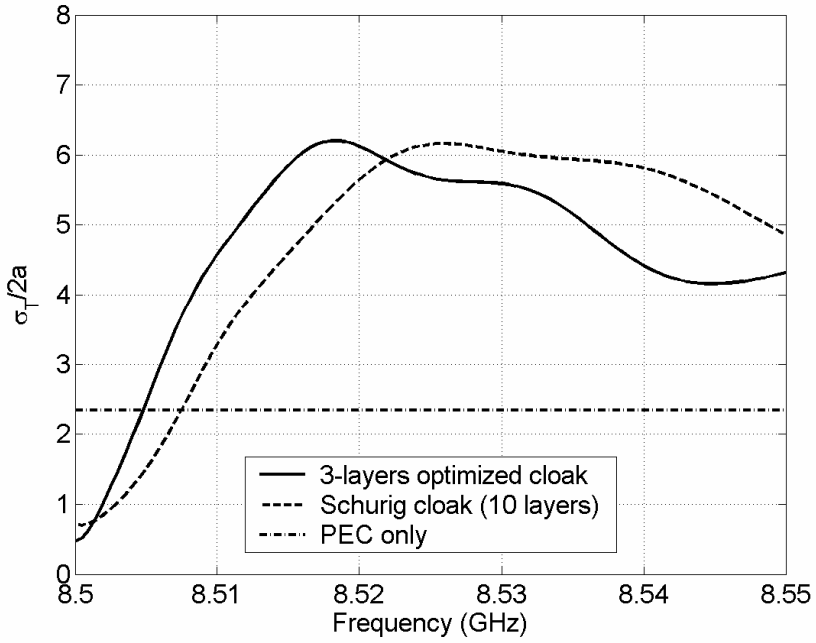

Figure 4.14. Normalized total scattering width vs. frequency for the Schurig cloak and the invisibility gain – optimized 3-layer cloak

Furthermore, sensitivity of the optimal solution to construction tolerances has been tested. We have run statistical analysis to estimate how much the variation (as a result of construction tolerances) of the values of the radial component of permeability tensor μ_r and of permittivity ε_z influences the obtained total scattering width. Fig. 4.15 shows the mean value of total scattering width if μ_r and ε_z are varied randomly from 0% to 5% of their initial (ideal) value with uniform distribution (worst case).

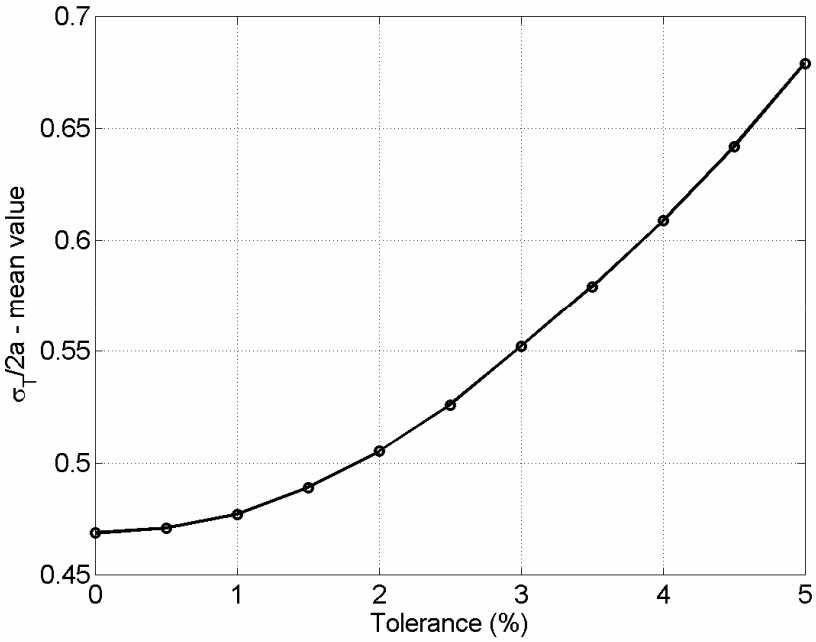

Figure 4.15. Dependence of obtained total scattering width on construction tolerances for the 3-layers cloak. The mean value of total scattering width is shown.

As an example, 2% tolerance was studied in more details. Constitutive parameters were varied uniformly in 2% interval of exact values for 10^6 times and total scattering width at central frequency (8.5 GHz) was calculated for each case. The number of values per small interval of total scattering width is given in Fig. 4.16. Obviously most values are concentrated around the exact value (around 0.47), suggesting that with reasonable construction tolerances it is still possible to obtain good invisibility performance.

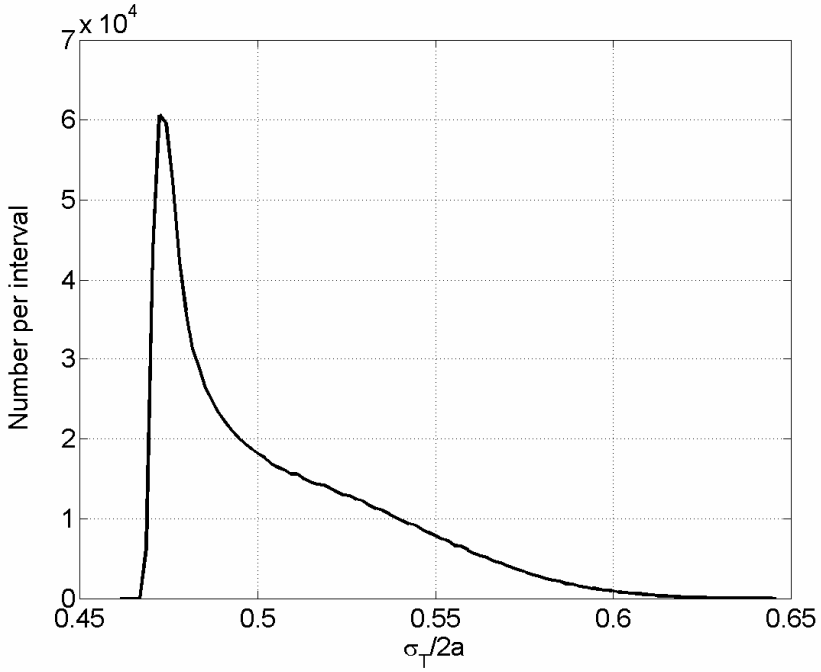

Figure 4.16. Distribution of 10^6 total scattering widths obtained by 2% variation of constitutive parameters

We have also investigated the influence of the cloaked cylinder diameter on performance of the cloak with three-layers (we have kept the ratio b/a = 2.173 as in the Schurig cloak). The results are summarized in table 4.6. It can be seen that the quality of the cloak with three-layers is drastically improved if we reduce the diameter of the cloaked cylinder: for the diameter of the cloaked cylinder $2a = 0.5\ \lambda$ the total scattered width is $\sigma_T/2a = 0.053$, while for the $2a = 3.0\ \lambda$ the total scattered width is $\sigma_T/2a = 0.876$ (this variation is larger than 10 times). On the other side the total scattered width of the 10-layer Schurig cloak varies only between 0.939 and 0.624. Furthermore, we have investigated how many layers the optimized cloak needs to contain in order to have better performance than the 10-layer Schurig cloak. We have concluded that for a small diameter of the cloaked cylinder it is enough to have 2 layers, while for larger diameters more layers are needed (e.g. for 3 λ cloaked cylinder one need to have 6-layer structure).

Cloaked cylinder diameter (2*a*)	$\sigma_T/2a$ **of optimized cloak with 3 layers**	$\sigma_T/2a$ **of Schurig cloak with 10 layers**	**Minimum number of layers of optimized cloak**
0.5 λ	0.053	0.939	2
1.0 λ	0.397	0.716	3
1.5 λ	0.469	0.717	3
2.0 λ	0.745	0.703	4
3.0 λ	0.876	0.624	6

Table 4.5. Total scattering widths of optimized 3-layer cloaks as a function of cloaked cylinder diameter.

Finally, we have investigated what is the optimal size (outer radius) of the cloak. As an example we have considered a PEC cylinder of variable radius and a three-layer cloak. The variables to be optimized are permeability in radial direction ($\mu_\varphi = 1.0$), the permittivity ε_z and the ratio *b/a.* The results are given in table 4.6. It can be seen that for small radius of the cloaked cylinder the cloak has resonant nature (i.e. the values of permeability in radial direction are alternating) and the optimal cloaks have large permittivity values. On the other side, for larger sizes of the cloaked cylinder the values of permeability in radial direction smoothly grows with the radial coordinate, and the outer radius and permittivity values are quite similar to the Schurig design (ε_z=3.431, *b/a* = 2.17).

Cloaked cylinder diameter (2a)	$\sigma_T/2a$ **of optimized cloak with 3 layers**	*b/a* **outer radius**	μ_r **of the first layer**	μ_r **of the second layer**	μ_r **of the third layer**	ε_z	$\sigma_T/2a$ **of Schurig cloak with 10 layers**
0.5 λ	0.009	1.924	0.8687	0.0050	0.3186	8.4627	0.939
1.0 λ	0.206	1.580	1.0	0.0145	0.1566	8.0124	0.716
1.5 λ	0.440	2.246	0.0251	0.1332	0.2449	3.5321	0.717
2.0 λ	0.561	1.848	0.0242	0.1071	0.1822	4.5858	0.703

Table 4.6. Relevant constitutive parameters of the 3-layer cloak with variable outer radius

5 OBLIQUE INCIDENCE PLANE WAVE SCATTERING BY SCHURIG CLOAK

Oblique incidence plane wave scattering by Schurig cloak

5.1. ANALYSIS METHOD

In the preceding chapters mathematical description, analysis and optimization of a cylindrical cloak for perpendicular incidence is made. In this chapter we will analyze the case when the incoming plane wave has an arbitrary angle of arrival (Figure 5.1). Oblique incidence is more complicated to analyze than perpendicular incidence because TE_z or TM_z incoming wave will also induce cross-polarization component. Because of this the resulting differential equations will be coupled. We would like to comment that this is a still open problem in scientific literature – till now only J. Monzon tried to solve this complex electromagnetic problem. In [29] he derived the solution using Barnes-type representation of cylinder functions (with the main practical question opened – how to make an efficient program that will solve this complex electromagnetic problem).

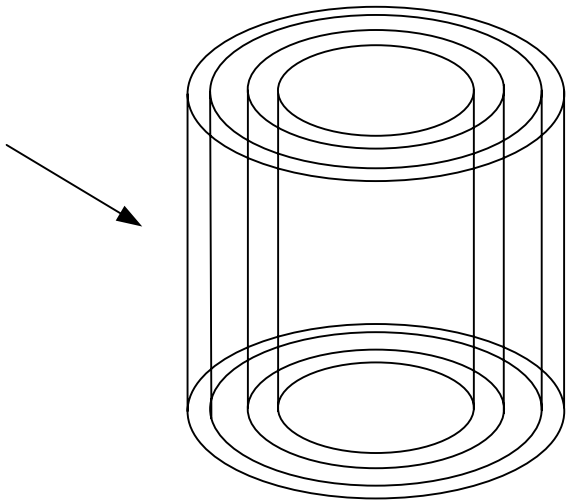

Figure 5.1 A sketch of the analyzed structure

Our analysis begins with the Maxwell equations. For the analysis only the Faraday and Ampere law are used:

$$\nabla \times \mathbf{E} = -\mathrm{j}\omega \underline{\boldsymbol{\mu}} \mathbf{H} \tag{5.1}$$

$$\nabla \times \mathbf{H} = \mathrm{j}\omega \underline{\boldsymbol{\varepsilon}} \mathbf{E} \tag{5.2}$$

In equations (5.1.a) and (5.1.b) $\underline{\boldsymbol{\mu}}$ and $\underline{\boldsymbol{\varepsilon}}$ represents tensor of permeability and permittivity with 3 components.

$$\underline{\boldsymbol{\mu}} = \begin{bmatrix} \mu_{\rho\rho} & 0 & 0 \\ 0 & \mu_{\phi\phi} & 0 \\ 0 & 0 & \mu_{zz} \end{bmatrix} \tag{5.3}$$

$$\underline{\boldsymbol{\varepsilon}} = \begin{bmatrix} \varepsilon_{\rho\rho} & 0 & 0 \\ 0 & \varepsilon_{\phi\phi} & 0 \\ 0 & 0 & \varepsilon_{zz} \end{bmatrix} \tag{5.4}$$

Cloak has cylindrical symmetry and because of that simplest way to solve the problem is to use the cylindrical coordinate system. Using the definition of the $\nabla\times$ operator in the cylindrical coordinate system [30] we get from equation (5.1):

$$\frac{1}{\rho}\frac{\partial E_z}{\partial \phi} - \frac{\partial E_\phi}{\partial z} = -\mathrm{j}\omega\mu_0\mu_{\rho\rho}H_\rho \tag{5.5}$$

$$\frac{\partial E_\rho}{\partial z} - \frac{\partial E_z}{\partial \rho} = -\mathrm{j}\omega\mu_0\mu_{\phi\phi}H_\phi \tag{5.6}$$

$$\frac{1}{\rho}\frac{\partial\left(\rho E_\phi\right)}{\partial \rho} - \frac{1}{\rho}\frac{\partial E_\rho}{\partial \phi} = -\mathrm{j}\omega\mu_0\mu_{zz}E_z \tag{5.7}$$

and from equation (5.2):

$$\frac{1}{\rho}\frac{\partial H_z}{\partial \phi} - \frac{\partial H_\phi}{\partial z} = \mathrm{j}\omega\varepsilon_0\varepsilon_{\rho\rho}E_\rho \tag{5.8}$$

$$\frac{\partial H_\rho}{\partial z} - \frac{\partial H_z}{\partial \rho} = \mathrm{j}\omega\varepsilon_0\varepsilon_{\phi\phi}E_\phi \tag{5.9}$$

$$\frac{1}{\rho}\frac{\partial\left(\rho H_\phi\right)}{\partial \rho} - \frac{1}{\rho}\frac{\partial H_\rho}{\partial \phi} = \mathrm{j}\omega\varepsilon_0\varepsilon_{zz}E_z \tag{5.10}$$

From the previous equations we can express the ρ and ϕ of the **E** and **H** fields in the following way:

$$E_\rho = -\mathrm{j}\frac{1}{\omega\varepsilon_0\varepsilon_{\rho\rho}}\frac{1}{\rho}\frac{\partial H_z}{\partial \phi} + \mathrm{j}\frac{1}{\omega\varepsilon_0\varepsilon_{\rho\rho}}\frac{\partial H_\phi}{\partial z} \tag{5.11}$$

$$E_\phi = -\mathrm{j}\frac{1}{\omega\varepsilon_0\varepsilon_{\phi\phi}}\frac{\partial H_\rho}{\partial z} + \mathrm{j}\frac{1}{\omega\varepsilon_0\varepsilon_{\phi\phi}}\frac{\partial H_z}{\partial \rho} \tag{5.12}$$

$$H_\rho = \mathrm{j}\frac{1}{\omega\mu_0\mu_{\rho\rho}}\frac{1}{\rho}\frac{\partial E_z}{\partial \phi} - \mathrm{j}\frac{1}{\omega\mu_0\mu_{\rho\rho}}\frac{\partial E_\phi}{\partial z} \tag{5.13}$$

$$H_\phi = \mathrm{j}\frac{1}{\omega\mu_0\mu_{\phi\phi}}\frac{\partial E_\rho}{\partial \mathrm{z}} - \mathrm{j}\frac{1}{\omega\mu_0\mu_{\phi\phi}}\frac{\partial E_z}{\partial \rho} \tag{5.14}$$

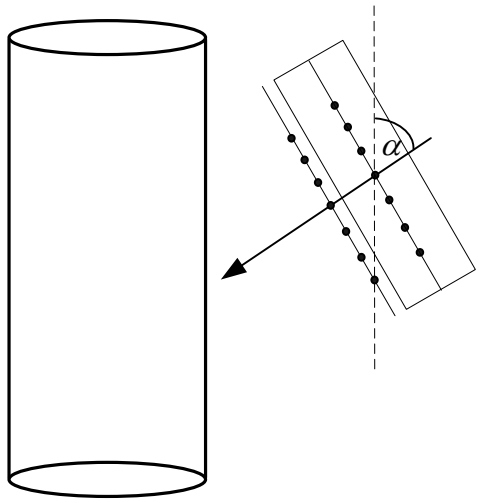

Figure 5.2. Translation symmetry in *z*-direction

From the translation symmetry in *z*-direction we can assume dependence of $\mathbf{E}$ and $\mathbf{H}$ fields in *z* coordinate as:

$$\mathbf{E}(\rho,\phi,z) = \hat{\mathbf{E}}(\rho,\phi)e^{-\mathrm{j}k_z z} \tag{5.15}$$

$$\mathbf{H}(\rho,\phi,z) = \hat{\mathbf{H}}(\rho,\phi)e^{-\mathrm{j}k_z z} \tag{5.16}$$

Symbol $\hat{\mathbf{E}}$ and $\hat{\mathbf{H}}$ represents $\mathbf{E}$ and $\mathbf{H}$ fields without dependency on *z* coordinate. With that assumption we get equations:

$$\hat{E}_\rho = -\mathrm{j}\frac{1}{\omega\varepsilon_0\varepsilon_{\rho\rho}}\frac{1}{\rho}\frac{\partial \hat{H}_z}{\partial \phi} + \frac{k_z}{\omega\varepsilon_0\varepsilon_{\rho\rho}}\hat{H}_\phi \tag{5.17}$$

$$\hat{E}_\phi = \frac{-k_z}{\omega\varepsilon_0\varepsilon_{\phi\phi}}\hat{H}_\rho + \mathrm{j}\frac{1}{\omega\varepsilon_0\varepsilon_{\phi\phi}}\frac{\partial \hat{H}_z}{\partial \rho} \tag{5.18}$$

$$\hat{H}_\rho = \mathrm{j}\frac{1}{\omega\mu_0\mu_{\rho\rho}}\frac{1}{\rho}\frac{\partial \hat{E}_z}{\partial \phi} - \frac{k_z}{\omega\mu_0\mu_{\rho\rho}}\hat{E}_\phi \tag{5.19}$$

$$\hat{H}_\phi = \frac{k_z}{\omega\mu_0\mu_{\phi\phi}}\hat{E}_\rho - \mathrm{j}\frac{1}{\omega\mu_0\mu_{\phi\phi}}\frac{\partial \hat{E}_z}{\partial \rho} \tag{5.20}$$

Because we want to represent the ρ and ϕ components of $\mathbf{E}$ and $\mathbf{H}$ fields as a function of E_z and H_z, we will substitute equations (5.17) and (5.18) into the equations (5.19) and (5.20) and vice versa. After short manipulation we get:

$$\hat{E}_\rho = -\mathrm{j}\frac{\omega\mu_0\mu_{\phi\phi}}{m_{\phi\rho}^2 - k_z^2}\frac{1}{\rho}\frac{\partial\hat{H}_z}{\partial\phi} - \mathrm{j}\frac{k_z}{m_{\phi\rho}^2 - k_z^2}\frac{\partial\hat{E}_z}{\partial\rho} \tag{5.21}$$

$$\hat{E}_\phi = -\mathrm{j}\frac{k_z}{m_{\rho\phi}^2 - k_z^2}\frac{1}{\rho}\frac{\partial\hat{E}_z}{\partial\phi} + \mathrm{j}\frac{\omega\mu_0\mu_{\rho\rho}}{m_{\rho\phi}^2 - k_z^2}\frac{\partial\hat{H}_z}{\partial\rho} \tag{5.22}$$

$$\hat{H}_\rho = \mathrm{j}\frac{\omega\varepsilon_0\varepsilon_{\phi\phi}}{m_{\rho\phi}^2 - k_z^2}\frac{1}{\rho}\frac{\partial\hat{E}_z}{\partial\phi} - \mathrm{j}\frac{k_z}{m_{\rho\phi}^2 - k_z^2}\frac{\partial\hat{H}_z}{\partial\rho} \tag{5.23}$$

$$\hat{H}_\phi = -\mathrm{j}\frac{k_z}{m_{\phi\rho}^2 - k_z^2}\frac{1}{\rho}\frac{\partial\hat{H}_z}{\partial\phi} - \mathrm{j}\frac{\omega\varepsilon_0\varepsilon_{\rho\rho}}{m_{\phi\rho}^2 - k_z^2}\frac{\partial\hat{E}_z}{\partial\rho} \tag{5.24}$$

where the used abbreviations are:

$$m_{\rho\phi}^2 = \omega^2\mu_0\mu_{\rho\rho}\varepsilon_0\varepsilon_{\phi\phi} \tag{5.25}$$

$$m_{\phi\rho}^2 = \omega^2\mu_0\mu_{\phi\phi}\varepsilon_0\varepsilon_{\rho\rho} \tag{5.26}$$

Equations (5.21) - (5.24) are substituted into equations (5.11) and (5.14) and after short derivation we get two coupled partial differential equations

$$\begin{aligned}&\rho^2\frac{\partial^2\hat{E}_z}{\partial\rho^2} + \rho\frac{\partial\hat{E}_z}{\partial\rho} + \rho^2\left(m_{\phi\rho}^2 - k_z^2\right)\frac{\varepsilon_{zz}}{\varepsilon_{\rho\rho}}\hat{E}_z + \frac{m_{\phi\rho}^2 - k_z^2}{m_{\rho\phi}^2 - k_z^2}\frac{\varepsilon_{\phi\phi}}{\varepsilon_{\rho\rho}}\frac{\partial^2\hat{E}_z}{\partial\phi^2} - \\ &\rho\frac{m_{\phi\rho}^2 - k_z^2}{m_{\rho\phi}^2 - k_z^2}\frac{k_z}{\omega\varepsilon_0\varepsilon_{\rho\rho}}\frac{\partial}{\partial\phi}\left(\frac{\partial\hat{H}_z}{\partial\rho}\right) + \rho\frac{k_z}{\omega\varepsilon_0\varepsilon_{\rho\rho}}\frac{\partial}{\partial\rho}\left(\frac{\partial\hat{H}_z}{\partial\phi}\right) = 0\end{aligned} \tag{5.27}$$

$$\begin{aligned}&\rho^2\frac{\partial^2\hat{H}_z}{\partial\rho^2} + \rho\frac{\partial\hat{H}_z}{\partial\rho} + \rho^2\left(m_{\rho\phi}^2 - k_z^2\right)\frac{\mu_{zz}}{\mu_{\rho\rho}}\hat{H}_z + \frac{m_{\rho\phi}^2 - k_z^2}{m_{\phi\rho}^2 - k_z^2}\frac{\mu_{\phi\phi}}{\mu_{\rho\rho}}\frac{\partial^2\hat{H}_z}{\partial\phi^2} + \\ &\rho\frac{m_{\rho\phi}^2 - k_z^2}{m_{\phi\rho}^2 - k_z^2}\frac{k_z}{\omega\mu_0\mu_{\rho\rho}}\frac{\partial}{\partial\phi}\left(\frac{\partial\hat{E}_z}{\partial\rho}\right) - \rho\frac{k_z}{\omega\mu_0\mu_{\rho\rho}}\frac{\partial}{\partial\rho}\left(\frac{\partial\hat{E}_z}{\partial\phi}\right) = 0\end{aligned} \tag{5.28}$$

Using the Schwartz theorem from multivariable calculus [31] and assumption that solutions of above equations are from $C^2\left(\left(\mathrm{a},\infty\right)\times\left(0,2\pi\right)\right)$, where *a* represents the inner radius of cloak, we can interchange the order of derivatives and get:

$$\begin{aligned}&\rho^2\frac{\partial^2\hat{E}_z}{\partial\rho^2} + \rho\frac{\partial\hat{E}_z}{\partial\rho} + \rho^2\left(m_{\phi\rho}^2 - k_z^2\right)\frac{\varepsilon_{zz}}{\varepsilon_{\rho\rho}}\hat{E}_z + \frac{m_{\phi\rho}^2 - k_z^2}{m_{\rho\phi}^2 - k_z^2}\frac{\varepsilon_{\phi\phi}}{\varepsilon_{\rho\rho}}\frac{\partial^2\hat{E}_z}{\partial\phi^2} - \\ &\rho\frac{m_{\phi\rho}^2 - k_z^2}{m_{\rho\phi}^2 - k_z^2}\frac{k_z}{\omega\varepsilon_0\varepsilon_{\rho\rho}}\frac{\partial}{\partial\rho}\left(\frac{\partial\hat{H}_z}{\partial\phi}\right) + \rho\frac{k_z}{\omega\varepsilon_0\varepsilon_{\rho\rho}}\frac{\partial}{\partial\rho}\left(\frac{\partial\hat{H}_z}{\partial\phi}\right) = 0\end{aligned} \tag{5.29}$$

$$\rho^2\frac{\partial^2\hat{H}_z}{\partial\rho^2}+\rho\frac{\partial\hat{H}_z}{\partial\rho}+\rho^2\left(m_{\rho\phi}^2-k_z^2\right)\frac{\mu_{zz}}{\mu_{\rho\rho}}\hat{H}_z+\frac{m_{\rho\phi}^2-k_z^2}{m_{\phi\rho}^2-k_z^2}\frac{\mu_{\phi\phi}}{\mu_{\rho\rho}}\frac{\partial^2\hat{H}_z}{\partial\phi^2}+$$
$$\rho\frac{m_{\rho\phi}^2-k_z^2}{m_{\phi\rho}^2-k_z^2}\frac{k_z}{\omega\mu_0\mu_{\rho\rho}}\frac{\partial}{\partial\rho}\left(\frac{\partial\hat{E}_z}{\partial\phi}\right)-\rho\frac{k_z}{\omega\mu_0\mu_{\rho\rho}}\frac{\partial}{\partial\rho}\left(\frac{\partial\hat{E}_z}{\partial\phi}\right)=0 \tag{5.30}$$

Now we have 2 coupled partial differential equations which are very hard to solve. We want somehow to remove derivation dependent on ϕ and get 2 coupled ordinary differential equations. From the spectral representation method of linear operators [32], [33] and theorems from functional analysis [34] we know that function can be decomposed in the base of eigenvectors of the operator.

$$\hat{E}_z(\rho,\phi)=\sum_{n=-\infty}^{+\infty}\underset{\sim}{\hat{E}}_z^n(\rho)e^{\mathrm{j}n\phi} \tag{5.31}$$

$$\hat{H}_z(\rho,\phi)=\sum_{n=-\infty}^{+\infty}\underset{\sim}{\hat{H}}_z^n(\rho)e^{\mathrm{j}n\phi} \tag{5.32}$$

After we substitute (5.31) and (5.32) into equations (5.29) and (5.30) we get:

$$\rho^2\frac{\partial^2}{\partial\rho^2}\left(\sum_{n=-\infty}^{+\infty}\underset{\sim}{\hat{E}}_z^n(\rho)e^{\mathrm{j}n\phi}\right)+\rho\frac{\partial}{\partial\rho}\left(\sum_{n=-\infty}^{+\infty}\underset{\sim}{\hat{E}}_z^n(\rho)e^{\mathrm{j}n\phi}\right)+$$
$$\rho^2\left(m_{\phi\rho}^2-k_z^2\right)\frac{\varepsilon_{zz}}{\varepsilon_{\rho\rho}}\left(\sum_{n=-\infty}^{+\infty}\underset{\sim}{\hat{E}}_z^n(\rho)e^{\mathrm{j}n\phi}\right)+\frac{m_{\phi\rho}^2-k_z^2}{m_{\rho\phi}^2-k_z^2}\frac{\varepsilon_{\phi\phi}}{\varepsilon_{\rho\rho}}\frac{\partial^2}{\partial\phi^2}\left(\sum_{n=-\infty}^{+\infty}\underset{\sim}{\hat{E}}_z^n(\rho)e^{\mathrm{j}n\phi}\right)- \tag{5.33}$$
$$\rho\frac{m_{\phi\rho}^2-k_z^2}{m_{\rho\phi}^2-k_z^2}\frac{k_z}{\omega\varepsilon_0\varepsilon_{\rho\rho}}\frac{\partial}{\partial\rho}\left(\frac{\partial}{\partial\phi}\left(\sum_{n=-\infty}^{+\infty}\underset{\sim}{\hat{H}}_z^n(\rho)e^{\mathrm{j}n\phi}\right)\right)+\rho\frac{k_z}{\omega\varepsilon_0\varepsilon_{\rho\rho}}\frac{\partial}{\partial\rho}\left(\frac{\partial}{\partial\phi}\left(\sum_{n=-\infty}^{+\infty}\underset{\sim}{\hat{H}}_z^n(\rho)e^{\mathrm{j}n\phi}\right)\right)=0$$

$$\rho^2\frac{\partial^2}{\partial\rho^2}\left(\sum_{n=-\infty}^{+\infty}\underset{\sim}{\hat{H}}_z^n(\rho)e^{\mathrm{j}n\phi}\right)+\rho\frac{\partial}{\partial\rho}\left(\sum_{n=-\infty}^{+\infty}\underset{\sim}{\hat{H}}_z^n(\rho)e^{\mathrm{j}n\phi}\right)+$$
$$\rho^2\left(m_{\rho\phi}^2-k_z^2\right)\frac{\mu_{zz}}{\mu_{\rho\rho}}\left(\sum_{n=-\infty}^{+\infty}\underset{\sim}{\hat{H}}_z^n(\rho)e^{\mathrm{j}n\phi}\right)+\frac{m_{\rho\phi}^2-k_z^2}{m_{\phi\rho}^2-k_z^2}\frac{\mu_{\phi\phi}}{\mu_{\rho\rho}}\frac{\partial^2}{\partial\phi^2}\left(\sum_{n=-\infty}^{+\infty}\underset{\sim}{\hat{H}}_z^n(\rho)e^{\mathrm{j}n\phi}\right)+ \tag{5.34}$$
$$\rho\frac{m_{\rho\phi}^2-k_z^2}{m_{\phi\rho}^2-k_z^2}\frac{k_z}{\omega\mu_0\mu_{\rho\rho}}\frac{\partial}{\partial\rho}\left(\frac{\partial}{\partial\phi}\left(\sum_{n=-\infty}^{+\infty}\underset{\sim}{\hat{E}}_z^n(\rho)e^{\mathrm{j}n\phi}\right)\right)-\rho\frac{k_z}{\omega\mu_0\mu_{\rho\rho}}\frac{\partial}{\partial\rho}\left(\frac{\partial}{\partial\phi}\left(\sum_{n=-\infty}^{+\infty}\underset{\sim}{\hat{E}}_z^n(\rho)e^{\mathrm{j}n\phi}\right)\right)=0$$

Eigenfunctions are lineary independent and operators with derivatives are linear [35] so we can interchange sums and derivatives, and by using linear independency we get:

$$\rho^2\frac{d^2\underset{\sim}{\hat{E}}_z^n}{d\rho^2}+\rho\frac{d\underset{\sim}{\hat{E}}_z^n}{d\rho}+\left(\rho^2\left(m_{\phi\rho}^2-k_z^2\right)\frac{\varepsilon_{zz}}{\varepsilon_{\rho\rho}}-n^2\frac{m_{\phi\rho}^2-k_z^2}{m_{\rho\phi}^2-k_z^2}\frac{\varepsilon_{\phi\phi}}{\varepsilon_{\rho\rho}}\right)\underset{\sim}{\hat{E}}_z^n+$$
$$\rho\left(\frac{\mathrm{j}nk_z}{\omega\varepsilon_0\varepsilon_{\rho\rho}}-\frac{m_{\phi\rho}^2-k_z^2}{m_{\rho\phi}^2-k_z^2}\frac{\mathrm{j}nk_z}{\omega\varepsilon_0\varepsilon_{\rho\rho}}\right)\frac{d\underset{\sim}{\hat{H}}_z^n}{d\rho}=0 \tag{5.35}$$

$$\rho^2\frac{d^2\hat{\underset{\sim}{H}}_z^n}{d\rho^2}+\rho\frac{d\hat{\underset{\sim}{H}}_z^n}{d\rho}+\left(\rho^2\left(m_{\rho\phi}^2-k_z^2\right)\frac{\mu_{zz}}{\mu_{\rho\rho}}-n^2\frac{m_{\rho\phi}^2-k_z^2}{m_{\phi\rho}^2-k_z^2}\frac{\mu_{\phi\phi}}{\mu_{\rho\rho}}\right)\hat{\underset{\sim}{H}}_z^n+$$
$$\rho\left(\frac{m_{\rho\phi}^2-k_z^2}{m_{\phi\rho}^2-k_z^2}\frac{\mathrm{j}nk_z}{\omega\mu_0\mu_{\rho\rho}}-\frac{\mathrm{j}nk_z}{\omega\mu_0\mu_{\rho\rho}}\right)\frac{d\hat{\underset{\sim}{E}}_z^n}{d\rho}=0 \tag{5.36}$$

In order to get compact notations we introduce the following coefficients:

$$\overline{A}_E(\rho)=\rho^2\left(m_{\phi\rho}^2-k_z^2\right)\frac{\varepsilon_{zz}}{\varepsilon_{\rho\rho}}-n^2\frac{m_{\phi\rho}^2-k_z^2}{m_{\rho\phi}^2-k_z^2}\frac{\varepsilon_{\phi\phi}}{\varepsilon_{\rho\rho}} \tag{5.37}$$

$$\overline{A}_H(\rho)=\rho\left(\frac{\mathrm{j}nk_z}{\omega\varepsilon_0\varepsilon_{\rho\rho}}-\frac{m_{\phi\rho}^2-k_z^2}{m_{\rho\phi}^2-k_z^2}\frac{\mathrm{j}nk_z}{\omega\varepsilon_0\varepsilon_{\rho\rho}}\right) \tag{5.38}$$

$$\overline{B}_H(\rho)=\rho^2\left(m_{\rho\phi}^2-k_z^2\right)\frac{\mu_{zz}}{\mu_{\rho\rho}}-n^2\frac{m_{\rho\phi}^2-k_z^2}{m_{\phi\rho}^2-k_z^2}\frac{\mu_{\phi\phi}}{\mu_{\rho\rho}} \tag{5.39}$$

$$\overline{B}_E(\rho)=\rho\left(\frac{m_{\rho\phi}^2-k_z^2}{m_{\phi\rho}^2-k_z^2}\frac{\mathrm{j}nk_z}{\omega\mu_0\mu_{\rho\rho}}-\frac{\mathrm{j}nk_z}{\omega\mu_0\mu_{\rho\rho}}\right) \tag{5.40}$$

Where line above coefficient represents function in the continuous domain. The compact notation of the considered partial differential equations is:

$$\rho^2\frac{d^2\hat{\underset{\sim}{E}}_z^n}{d\rho^2}+\rho\frac{d\hat{\underset{\sim}{E}}_z^n}{d\rho}+\overline{A}_E\hat{\underset{\sim}{E}}_z^n+\overline{A}_H\frac{d\hat{\underset{\sim}{H}}_z^n}{d\rho}=0 \tag{5.41}$$

$$\rho^2\frac{d^2\hat{\underset{\sim}{H}}_z^n}{d\rho^2}+\rho\frac{d\hat{\underset{\sim}{H}}_z^n}{d\rho}+\overline{B}_H\hat{\underset{\sim}{H}}_z^n+\overline{B}_E\frac{d\hat{\underset{\sim}{E}}_z^n}{d\rho}=0 \tag{5.42}$$

Outside cloak $\underline{\boldsymbol{\mu}}=1$ and $\underline{\boldsymbol{\varepsilon}}=1$ which simplifies equations to:

$$\rho^2\frac{d^2\hat{\underset{\sim}{E}}_z^n}{d\rho^2}+\rho\frac{d\hat{\underset{\sim}{E}}_z^n}{d\rho}+\left(\rho^2\left(k_0^2-k_z^2\right)-n^2\right)\hat{\underset{\sim}{E}}_z^n=0 \tag{5.43}$$

$$\rho^2\frac{d^2\hat{\underset{\sim}{H}}_z^n}{d\rho^2}+\rho\frac{d\hat{\underset{\sim}{H}}_z^n}{d\rho}+\left(\rho^2\left(k_0^2-k_z^2\right)-n^2\right)\hat{\underset{\sim}{H}}_z^n=0 \tag{5.44}$$

where:

$$k_0=\frac{2\pi}{\lambda} \tag{5.49}$$

For TM_z incident wave we can write (see Figure 5.3)

$$\mathbf{E}^i=E_0^i\left(\hat{x}\cos(\alpha)+\hat{z}\sin(\alpha)\right)e^{-\mathrm{j}k_0\sin(\alpha)x+\mathrm{j}k_0\cos(\alpha)z} \tag{5.50}$$

The scattered field is equal

$$E_0^s = R \cdot E_0^i \tag{5.51}$$

$$\mathbf{E}^s = E_0^s \left(-\hat{x}\cos(\alpha) + \hat{z}\sin(\alpha)\right) e^{\mathrm{j}k_0 \sin(\alpha)x + \mathrm{j}k_0 \cos(\alpha)z} \tag{5.52}$$

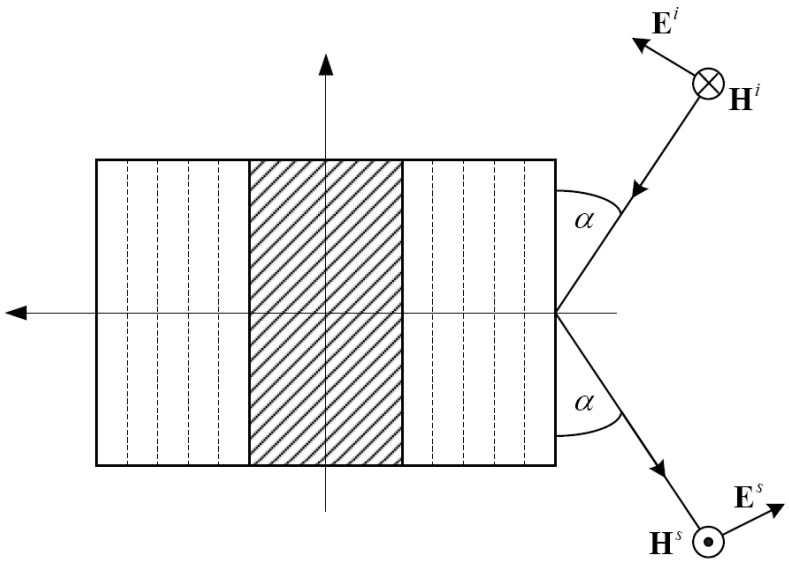

Figure 5.3. Oblique incidence on cloak, TM_z mode

We are interested in E_z and H_z components.

$$E_z^i = E_0^i \sin(\alpha) e^{-\mathrm{j}k_0 \sin(\alpha)x + \mathrm{j}k_0 \cos(\alpha)z} \tag{5.53}$$

$$E_z^s = E_0^s \sin(\alpha) e^{\mathrm{j}k_0 \sin(\alpha)x + \mathrm{j}k_0 \cos(\alpha)z} \tag{5.54}$$

We can choose z=0 for incidence plane

$$E_z^i = E_0^i \sin(\alpha) e^{-\mathrm{j}k_0 \sin(\alpha)x} \tag{5.55}$$

$$E_z^s = E_0^s \sin(\alpha) e^{\mathrm{j}k_0 \sin(\alpha)x} \tag{5.56}$$

Solutions for equations (5.43) and (5.43) are [36]

$$\hat{\underset{\sim}{E}}_z^n = J_n(k_z \rho) \tag{5.57}$$

$$\hat{\underset{\sim}{E}}_z^n = R_n \mathrm{H}_n^{(2)}(k_z \rho) \tag{5.58}$$

where (5.57) represents incoming and (5.58) outgoing wave. From representation exponential functions with Bessel function we get [37]:

$$\hat{E}_z^n = E_0 \sin(\alpha) \sum_{n=-\infty}^{\infty} \mathrm{j}^{-n} \left(\mathrm{J}_n(k_z\rho) + R_n \mathrm{H}_n^{(2)}(k_z\rho) \right) e^{\mathrm{j}n\phi} \tag{5.59.a}$$

$$\hat{H}_z^n = E_0 \sin(\alpha) \sum_{n=-\infty}^{\infty} \mathrm{j}^{-n} C_n \mathrm{H}_n^{(2)}(k_z\rho) e^{\mathrm{j}n\phi} \tag{5.59.b}$$

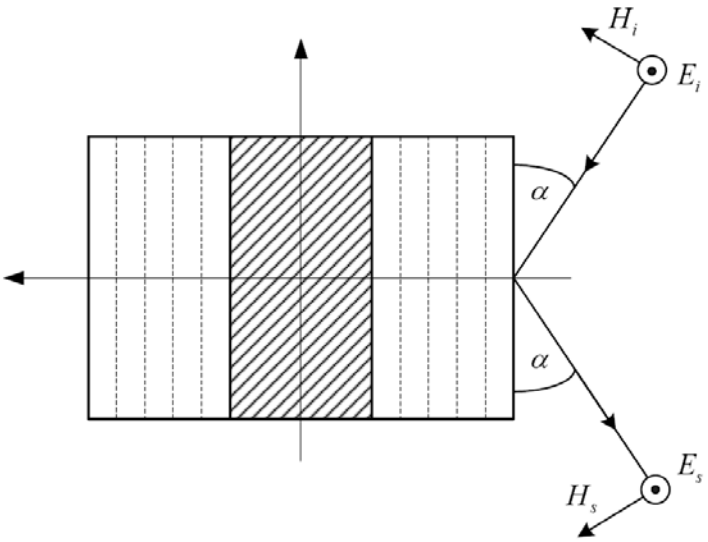

Figure 5.4. Oblique incidence on cloak, TE_z mode

For TE_z polarization similar procedure gives us:

$$\hat{E}_z^n = E_0 \sin(\alpha) \sum_{n=-\infty}^{\infty} \mathrm{j}^{-n} R_n \mathrm{H}_n^{(2)}(k_z\rho) e^{\mathrm{j}n\phi} \tag{5.60.a}$$

$$\hat{H}_z^n = E_0 \sin(\alpha) \sum_{n=-\infty}^{\infty} \mathrm{j}^{-n} \left(\mathrm{J}_n(k_z\rho) + C_n \mathrm{H}_n^{(2)}(k_z\rho) \right) e^{\mathrm{j}n\phi} \tag{5.60.b}$$

Equations inside the cloak region will be solved using finite difference method [38], [39]. Derivation is approximated with central difference formula

$$\frac{d\hat{\underset{\sim}{E}}_z^n}{d\rho}(\rho_0) \approx \frac{\hat{\underset{\sim}{E}}_z^n[\rho_0 + h] - \hat{\underset{\sim}{E}}_z^n[\rho_0 - h]}{2h} \tag{5.61}$$

$$\frac{d^2\hat{\underset{\sim}{E}}_z^n}{d\rho^2}(\rho_0) \approx \frac{\hat{\underset{\sim}{E}}_z^n[\rho_0 + h] - 2\hat{\underset{\sim}{E}}_z^n[\rho_0] + \hat{\underset{\sim}{E}}_z^n[\rho_0 - h]}{h^2} \tag{5.62}$$

where *h* represent difference between two points in the radial direction in equidistant domain subdivision. Distance from PEC is approximated with:

$$\rho = a + ih, \qquad i = 0, 1, 2, \ldots \tag{5.63}$$

Coefficients in equations (5.37) – (5.40) are approximated with:

$$A_E[i] = (a+ih)^2 \left(m_{\phi\rho}^2 - k_z^2\right)\frac{\varepsilon_{zz}}{\varepsilon_{\rho\rho}} - n^2\frac{m_{\phi\rho}^2 - k_z^2}{m_{\rho\phi}^2 - k_z^2}\frac{\varepsilon_{\phi\phi}}{\varepsilon_{\rho\rho}} \tag{5.64}$$

$$A_H[i] = (a+ih)\left(\frac{\mathrm{j}nk_z}{\omega\varepsilon_0\varepsilon_{\rho\rho}} - \frac{m_{\phi\rho}^2 - k_z^2}{m_{\rho\phi}^2 - k_z^2}\frac{\mathrm{j}nk_z}{\omega\varepsilon_0\varepsilon_{\rho\rho}}\right) \tag{5.65}$$

$$B_H[i] = (a+ih)^2 \left(m_{\rho\phi}^2 - k_z^2\right)\frac{\mu_{zz}}{\mu_{\rho\rho}} - n^2\frac{m_{\rho\phi}^2 - k_z^2}{m_{\phi\rho}^2 - k_z^2}\frac{\mu_{\phi\phi}}{\mu_{\rho\rho}} \tag{5.66}$$

$$B_E[i] = (a+ih)\left(\frac{m_{\rho\phi}^2 - k_z^2}{m_{\phi\rho}^2 - k_z^2}\frac{\mathrm{j}nk_z}{\omega\mu_0\mu_{\rho\rho}} - \frac{\mathrm{j}nk_z}{\omega\mu_0\mu_{\rho\rho}}\right) \tag{5.67}$$

By this equations (5.41) and (5.42) are transformed into:

$$\begin{aligned}&(a+ih)^2\frac{\hat{\underset{\sim}{E}}_z^n[i+1] - 2\hat{\underset{\sim}{E}}_z^n[i] + \hat{\underset{\sim}{E}}_z^n[i-1]}{h^2} + (a+ih)\frac{\hat{\underset{\sim}{E}}_z^n[i+1] - \hat{\underset{\sim}{E}}_z^n[i-1]}{2h} + \\ &A_E[i]\hat{\underset{\sim}{E}}_z^n[i] + A_H[i]\frac{\hat{\underset{\sim}{H}}_z^n[i+1] - \hat{\underset{\sim}{H}}_z^n[i-1]}{2h} = 0\end{aligned} \tag{5.68}$$

$$\begin{aligned}&(a+ih)^2\frac{\hat{\underset{\sim}{H}}_z^n[i+1] - 2\hat{\underset{\sim}{H}}_z^n[i] + \hat{\underset{\sim}{H}}_z^n[i-1]}{h^2} + (a+ih)\frac{\hat{\underset{\sim}{H}}_z^n[i+1] - \hat{\underset{\sim}{H}}_z^n[i-1]}{2h} + \\ &B_H[i]\hat{\underset{\sim}{H}}_z^n[i] + B_E[i]\frac{\hat{\underset{\sim}{E}}_z^n[i+1] - \hat{\underset{\sim}{E}}_z^n[i-1]}{2h} = 0\end{aligned} \tag{5.69}$$

By grouping the coefficients we get:

$$\begin{aligned}&\hat{\underset{\sim}{E}}_z^n[i-1]\left\{\left(\frac{a+ih}{h}\right)^2 - \frac{a+ih}{2h}\right\} + \hat{\underset{\sim}{E}}_z^n[i]\left\{-2\left(\frac{a+ih}{h}\right)^2 + A_E[i]\right\} + \\ &\hat{\underset{\sim}{E}}_z^n[i+1]\left\{\left(\frac{a+ih}{h}\right)^2 + \frac{a+ih}{2h}\right\} + \hat{\underset{\sim}{H}}_z^n[i-1]\left\{-\frac{A_H[i]}{2h}\right\} + \hat{\underset{\sim}{H}}_z^n[i+1]\left\{\frac{A_H[i]}{2h}\right\} = 0\end{aligned} \tag{5.70}$$

$$\hat{\underset{\sim}{H}}_z^n[i-1]\left\{\left(\frac{a+ih}{h}\right)^2-\frac{a+ih}{2h}\right\}+\hat{\underset{\sim}{H}}_z^n[i]\left\{-2\left(\frac{a+ih}{h}\right)^2+B_H[i]\right\}+$$
$$\hat{\underset{\sim}{H}}_z^n[i+1]\left\{\left(\frac{a+ih}{h}\right)^2+\frac{a+ih}{2h}\right\}+\hat{\underset{\sim}{E}}_z^n[i-1]\left\{-\frac{B_E[i]}{2h}\right\}+\hat{\underset{\sim}{E}}_z^n[i+1]\left\{\frac{B_E[i]}{2h}\right\}=0 \quad (5.71)$$

For solving the considered system of equations we need to introduce the boundary conditions at each layer boundary

$$H_\phi\big|_{\rho-}=H_\phi\big|_{\rho+} \quad (5.72)$$

$$E_\phi\big|_{\rho-}=E_\phi\big|_{\rho+} \quad (5.73)$$

$$E_z\big|_{\rho-}=E_z\big|_{\rho+} \quad (5.74)$$

$$H_z\big|_{\rho-}=H_z\big|_{\rho+} \quad (5.75)$$

From equation (5.24) and the following supstitution for coefficients

$$M_\phi^H=\frac{k_z n}{m_{\phi\rho}^2-k_z^2}\frac{1}{\rho} \quad (5.76)$$

$$M_\phi^E=-\mathrm{j}\frac{\omega\varepsilon_0\varepsilon_{\rho\rho}}{m_{\phi\rho}^2-k_z^2} \quad (5.77)$$

we get the equation for H_ϕ component at the boundary between two layers

$$\hat{\underset{\sim}{H}}_\phi^n=M_\phi^H\hat{\underset{\sim}{H}}_z^n+\underset{\sim}{M}_\phi^E\frac{\partial\hat{\underset{\sim}{E}}_z^n}{\partial\rho} \quad (5.78)$$

By discretizing the equation and by expressing the ρ coordinate as $a+ih$ we get:

$$\hat{\underset{\sim}{H}}_\phi^n[N]=M_\phi^H\hat{\underset{\sim}{H}}_z^n[N]+M_\phi^E\frac{\hat{\underset{\sim}{E}}_z^n[N]-\hat{\underset{\sim}{E}}_z^n[N-1]}{h} \quad (5.79)$$

The boundary condition for the continuity of the H_ϕ component will give the following equation

$$\underline{M}_\phi^H\hat{\underset{\sim}{H}}_z^n[N]+\underline{M}_\phi^E\frac{\hat{\underset{\sim}{E}}_z^n[N]-\hat{\underset{\sim}{E}}_z^n[N-1]}{h}=\overline{M}_\phi^H\hat{\underset{\sim}{H}}_z^n[N+1]+\overline{M}_\phi^E\frac{\hat{\underset{\sim}{E}}_z^n[N+2]-\hat{\underset{\sim}{E}}_z^n[N+1]}{h} \quad (5.80)$$

The form that is suitable for coding is equal

$$\hat{\underset{\sim}{E}}_z^n[N-1]\left\{-\frac{\underline{M}_\phi^E}{h}\right\}+\hat{\underset{\sim}{E}}_z^n[N]\left\{\frac{\underline{M}_\phi^E}{h}\right\}+\hat{\underset{\sim}{E}}_z^n[N+1]\left\{\frac{\overline{M}_\phi^E}{h}\right\}+\hat{\underset{\sim}{E}}_z^n[N+2]\left\{-\frac{\overline{M}_\phi^E}{h}\right\}+$$
$$\hat{\underset{\sim}{H}}_z^n[N]\left\{\underline{M}_\phi^H\right\}+\hat{\underset{\sim}{H}}_z^n[N+1]\left\{-\overline{M}_\phi^H\right\}=0 \tag{5.81}$$

The boundary condition for E_ϕ results in a dual equation:

$$\hat{\underset{\sim}{E}}_\phi^n=N_\phi^E\hat{\underset{\sim}{E}}_z^n+N_\phi^H\frac{\partial\hat{\underset{\sim}{H}}_z^n}{\partial\rho} \tag{5.82}$$

and in a dual discretized-form equation

$$\hat{\underset{\sim}{H}}_z^n[N-1]\left\{-\frac{\underline{N}_\phi^H}{h}\right\}+\hat{\underset{\sim}{H}}_z^n[N]\left\{\frac{\underline{N}_\phi^H}{h}\right\}+\hat{\underset{\sim}{H}}_z^n[N+1]\left\{\frac{\overline{N}_\phi^H}{h}\right\}+\hat{\underset{\sim}{H}}_z^n[N+2]\left\{-\frac{\overline{N}_\phi^H}{h}\right\}+$$
$$\hat{\underset{\sim}{E}}_z^n[N]\left\{\underline{N}_\phi^E\right\}+\hat{\underset{\sim}{E}}_z^n[N+1]\left\{-\overline{N}_\phi^E\right\}=0 \tag{5.83}$$

where abbreviations represents:

$$N_\phi^E=\frac{k_z n}{m_{\rho\phi}^2-k_z^2}\frac{1}{\rho} \tag{5.84}$$

$$N_\phi^H=\mathrm{j}\frac{\omega\mu_0\mu_{\rho\rho}}{m_{\rho\phi}^2-k_z^2} \tag{5.85}$$

Discretization of the last two boundary conditions results in:

$$\hat{\underset{\sim}{H}}_z^n[N]=\hat{\underset{\sim}{H}}_z^n[N+1] \tag{5.86}$$

$$\hat{\underset{\sim}{E}}_z^n[N]=\hat{\underset{\sim}{E}}_z^n[N+1] \tag{5.87}$$

Boundary conditions at the PEC boundary are:

$$\hat{\underset{\sim}{E}}_z^n[1]=0 \tag{5.88}$$

$$\hat{\underset{\sim}{E}}_\phi^n[1]=0 \tag{5.89}$$

Boundary condition for the *H*-field together with equation (5.22) results in:

$$\hat{\underset{\sim}{H}}_z^n[1]=\hat{\underset{\sim}{H}}_z^n[2] \tag{5.90}$$

For TM_z polarization, the boundary conditions on the external boundary are obtained using the equations (5.59.a) and (5.59.b):

$$\underline{M}_{\phi}^{H}\hat{\underset{\sim}{H}}_{z}^{n}[N]+\underline{M}_{\phi}^{E}\frac{\hat{\underset{\sim}{E}}_{z}^{n}[N]-\hat{\underset{\sim}{E}}_{z}^{n}[N-1]}{h}=$$
$$\bar{M}_{\phi}^{H}\sin(\alpha)j^{-n}C_{n}\mathrm{H}_{n}^{(2)}(k_{z}b)+\bar{M}_{\phi}^{E}\sin(\alpha)j^{-n}\left(\mathrm{J}_{n}'(k_{z}b)+R_{n}\mathrm{H}_{n}'^{(2)}(k_{z}b)\right) \quad (5.91)$$

$$\underline{N}_{\phi}^{E}\hat{\underset{\sim}{E}}_{z}^{n}[N]+\underline{N}_{\phi}^{H}\frac{\hat{\underset{\sim}{H}}_{z}^{n}[N]-\hat{\underset{\sim}{H}}_{z}^{n}[N-1]}{h}=$$
$$\bar{N}_{\phi}^{E}\sin(\alpha)j^{-n}\left(\mathrm{J}_{n}(k_{z}b)+R_{n}\mathrm{H}_{n}^{(2)}(k_{z}b)\right)+\bar{N}_{\phi}^{H}\sin(\alpha)j^{-n}C_{n}\mathrm{H}_{n}'^{(2)}(k_{z}b) \quad (5.92)$$

which results in

$$\hat{\underset{\sim}{E}}_{z}^{n}[N-1]\left\{-\frac{\underline{M}_{\phi}^{E}}{h}\right\}+\hat{\underset{\sim}{E}}_{z}^{n}[N]\left\{\frac{\underline{M}_{\phi}^{E}}{h}\right\}+\hat{\underset{\sim}{H}}_{z}^{n}[N]\left\{\underline{M}_{\phi}^{H}\right\}+R_{n}\left\{-j^{-n}\sin(\alpha)\bar{M}_{\phi}^{E}\mathrm{H}_{n}'^{(2)}(k_{z}b)\right\}+$$
$$C_{n}\left\{-j^{-n}\sin(\alpha)\bar{M}_{\phi}^{H}\mathrm{H}_{n}^{(2)}(k_{z}b)\right\}=j^{-n}\sin(\alpha)\bar{M}_{\phi}^{E}\mathrm{J}_{n}'(k_{z}b) \quad (5.93)$$

$$\hat{\underset{\sim}{H}}_{z}^{n}[N-1]\left\{-\frac{\underline{N}_{\phi}^{H}}{h}\right\}+\hat{\underset{\sim}{H}}_{z}^{n}[N]\left\{\frac{\underline{N}_{\phi}^{H}}{h}\right\}+\hat{\underset{\sim}{E}}_{z}^{n}[N]\left\{\underline{N}_{\phi}^{E}\right\}+R_{n}\left\{-j^{-n}\sin(\alpha)\bar{N}_{\phi}^{E}\mathrm{H}_{n}^{(2)}(k_{z}b)\right\}+$$
$$C_{n}\left\{-j^{-n}\sin(\alpha)\bar{N}_{\phi}^{H}\mathrm{H}_{n}'^{(2)}(k_{z}b)\right\}=j^{-n}\sin(\alpha)\bar{N}_{\phi}^{E}\mathrm{J}_{n}(k_{z}b) \quad (5.94)$$

Boundary conditions (5.74) and (5.75) results in:

$$\hat{\underset{\sim}{E}}_{z}^{n}[N]=j^{-n}\sin(\alpha)\left(\mathrm{J}_{n}(k_{z}b)+R_{n}\mathrm{H}_{n}^{(2)}(k_{z}b)\right) \quad (5.95)$$

$$\hat{\underset{\sim}{H}}_{z}^{n}[N]=j^{-n}\sin(\alpha)C_{n}\mathrm{H}_{n}^{(2)}(k_{z}b) \quad (5.96)$$

which give us the final two equations:

$$\hat{\underset{\sim}{E}}_{z}^{n}[N]+R_{n}\left\{-j^{-n}\sin(\alpha)\mathrm{H}_{n}^{(2)}(k_{z}b)\right\}=j^{-n}\sin(\alpha)\mathrm{J}_{n}(k_{z}b) \quad (5.97)$$

$$\hat{\underset{\sim}{H}}_{z}^{n}[N]+C_{n}\left\{-j^{-n}\sin(\alpha)\mathrm{H}_{n}^{(2)}(k_{z}b)\right\}=0 \quad (5.98)$$

For TE_z polarization, the boundary conditions on the external boundary are obtained using the equations (5.60.a) and (5.60.b):

$$\underline{M}_{\phi}^{H}\hat{\underset{\sim}{H}}_{z}^{n}[N]+\underline{M}_{\phi}^{E}\frac{\hat{\underset{\sim}{E}}_{z}^{n}[N]-\hat{\underset{\sim}{E}}_{z}^{n}[N-1]}{h}=$$
$$\bar{M}_{\phi}^{H}\sin(\alpha)j^{-n}\left(\mathrm{J}_{n}(k_{z}b)+C_{n}\mathrm{H}_{n}^{(2)}(k_{z}b)\right)+\bar{M}_{\phi}^{E}\sin(\alpha)j^{-n}R_{n}\mathrm{H}_{n}'^{(2)}(k_{z}b) \quad (5.99)$$

$$\underline{N}_{\phi}^{E}\hat{\underset{\sim}{E}}_{z}^{n}[N]+\underline{N}_{\phi}^{H}\frac{\hat{\underset{\sim}{H}}_{z}^{n}[N]-\hat{\underset{\sim}{H}}_{z}^{n}[N-1]}{h}=$$
$$\bar{N}_{\phi}^{E}\sin(\alpha)j^{-n}R_{n}\mathrm{H}_{n}^{(2)}(k_{z}b)+\bar{N}_{\phi}^{H}\sin(\alpha)j^{-n}\left(\mathrm{J}_{n}'(k_{z}b)+C_{n}\mathrm{H}_{n}'^{(2)}(k_{z}b)\right) \quad (5.100)$$

which result in:

$$\hat{\underset{\sim}{E}}_z^n[N-1]\left\{-\frac{\underline{M}_\phi^E}{h}\right\}+\hat{\underset{\sim}{E}}_z^n[N]\left\{\frac{\underline{M}_\phi^E}{h}\right\}+\hat{\underset{\sim}{H}}_z^n[N]\left\{\underline{M}_\phi^H\right\}+R_n\left\{-j^{-n}\sin(\alpha)\bar{M}_\phi^E\mathrm{H}_n'^{(2)}(k_z b)\right\}+ \quad (5.101)$$
$$C_n\left\{-j^{-n}\sin(\alpha)\bar{M}_\phi^H\mathrm{H}_n^{(2)}(k_z b)\right\}=j^{-n}\sin(\alpha)\bar{M}_\phi^H\mathrm{J}_n(k_z b)$$

$$\hat{\underset{\sim}{H}}_z^n[N-1]\left\{-\frac{\underline{N}_\phi^H}{h}\right\}+\hat{\underset{\sim}{H}}_z^n[N]\left\{\frac{\underline{N}_\phi^H}{h}\right\}+\hat{\underset{\sim}{E}}_z^n[N]\left\{\underline{N}_\phi^E\right\}+R_n\left\{-j^{-n}\sin(\alpha)\bar{N}_\phi^E\mathrm{H}_n^{(2)}(k_z b)\right\}+ \quad (5.102)$$
$$C_n\left\{-j^{-n}\sin(\alpha)\bar{N}_\phi^H\mathrm{H}_n'^{(2)}(k_z b)\right\}=j^{-n}\sin(\alpha)\bar{N}_\phi^H\mathrm{J}_n'(k_z b)$$

Boundary conditions (5.74) and (5.75) result in:

$$\hat{\underset{\sim}{E}}_z^n[N]=j^{-n}\sin(\alpha)R_n\mathrm{H}_n^{(2)}(k_z b) \quad (5.103)$$

$$\hat{\underset{\sim}{H}}_z^n[N]=j^{-n}\sin(\alpha)\left(\mathrm{J}_n(k_z b)+C_n\mathrm{H}_n^{(2)}(k_z b)\right) \quad (5.104)$$

which give us the final two equations in TE^z case:

$$\hat{\underset{\sim}{E}}_z^n[N]+R_n\left\{-j^{-n}\sin(\alpha)\mathrm{H}_n^{(2)}(k_z b)\right\}=0 \quad (5.105)$$

$$\hat{\underset{\sim}{H}}_z^n[N]+C_n\left\{-j^{-n}\sin(\alpha)\mathrm{H}_n^{(2)}(k_z b)\right\}=j^{-n}\sin(\alpha)\mathrm{J}_n(k_z b) \quad (5.106)$$

The expression for the scattering width σ_{2D} and for the total scattering width σ_T are obtained as follows. From the definition [17]:

$$\sigma_{2D}=\lim_{\rho\to\infty}2\pi\rho\left|\frac{E^s}{E^i}\right|^2 \quad (5.107)$$

it follows (we substitute the expressions for the incident and scattered waves):

$$\sigma_{2D}=\lim_{\rho\to\infty}2\pi\rho\left|\frac{E_0\sum_{n=-\infty}^{\infty}j^{-n}R_n\mathrm{H}_n^{(2)}(k_z b)e^{jn\phi}}{E^i e^{-jk_z x}}\right|^2 \quad (5.108)$$

Using large argument approximation of the Hankel function [36]

$$\mathrm{H}_n^{(2)}(k_z\rho)\cong\sqrt{\frac{2j}{\pi k_z\rho}}j^n\mathrm{e}^{-jk_z\rho} \quad (5.109)$$

we obtain the expression for the scattering width σ_{2D}:

$$\sigma_{2D} = \frac{4}{k_0 \sin(\alpha)} \left| \sum_{n=-\infty}^{\infty} R_n e^{jn\phi} \right|^2 \tag{5.110}$$

For TE^z polarization the used definition for radar cross section is [17]:

$$\sigma_{2D} = \lim_{\rho \to \infty} 2\pi\rho \left| \frac{H^s}{H^i} \right|^2 \tag{5.111}$$

With the large value approximation from (5.109) and with the definition of incident and scattered wave for TE^z case (see eqs. (5.60.a) and (5.60.b)), equation (5.111) is reduced to:

$$\sigma_{2D} = \frac{4}{k_0 \sin(\alpha)} \left| \sum_{n=-\infty}^{\infty} C_n e^{jn\phi} \right|^2 \tag{5.112}$$

The total scattering width is defined as

$$\sigma_T = \frac{P_L}{\left| S^i \right|} \tag{5.113}$$

where $\left| S^i \right|$ represents the magnitude of the Poyting vector of the incident wave and P_L represents the scattered power per unit length (in the axial direction):

$$\mathbf{S}^i = \frac{\left| E_0^i \right|^2}{2\eta} \mathbf{k}^i \tag{5.114}$$

$$P_L = \rho \int_0^{2\pi} \mathbf{S}^s \cdot \boldsymbol{\rho} d\phi = \rho \int_0^{2\pi} \frac{2}{\pi k_0 \rho} \left| \sum_{n=-\infty}^{\infty} R_n e^{in\phi} \right|^2 \tag{5.115}$$

$$\mathbf{S}^s = \frac{\left| E_0^s \right|^2}{2\eta} \mathbf{k}^i \tag{5.116}$$

Using the orthogonality of complex exponentials $\exp(jn\phi)$ and after short manipulation we get:

$$\sigma_T^{TM} = \frac{4}{k_0} \sum_{n=-\infty}^{\infty} \left| R_n \right|^2 \tag{5.117}$$

$$\sigma_T^{TE} = \frac{4}{k_0} \sum_{n=-\infty}^{\infty} \left| C_n \right|^2 \tag{5.118}$$

5.2. RESULTS

Using the developed program for the oblique incidence we have tested the sensitivity of the Schurig cloak on the angle of incidence wave. The original problem was a 2D problem, i.e. it was assumed that the incoming angle of the incident wave is 90 degrees. However, for practical realizations it is very important to check the sensitivity of the considered cloak on incoming angle of the incident wave. Figure 5.5 illustrates the sensitivity of the Schurig cloak (we have used a 10-layer model of the cloak). It can be seen that the cloak has scattered-field reduction property up to incoming angle ~ 75º (or ~ 105 º). For angles smaller than 75º the cloaked cylinder scatters more power than the bare PEC cylinder. That can be seen in Fig. 5.6 where the scattered width of the cloaked and bare PEC cylinder is compared for incident angle 75º. The cross-polarized scattered field is also shown in Fig. 5.6 (the cross-polarized scattered field is not excited only for normal incidence). In Figures 5.7 and 5.8 we have investigated properties of the TE_z (Cai) cloak. The parameters of the cloak are defined by the equaton (3.1.c), and we have analyzed a 10-layer realization of the TE_z cloak. It can be seen that the TM_z cloak is less sensitive on the angle of arival of incident wave than the TE_z cloak. From Figures 5.7 and 5.8 it can be seen that for TE_z cloak for angles smaller than 80º the cloaked cylinder scatters more power than the bare PEC cylinder.

The sensitivity to angle of incidence can ba also illustrated by plotting the total scattered width of the PEC cylinder with and without the cloak. Both TM_z and TE_z cases are considered in Figures 5.9 and 5.10. It can be seen that the TM_z (Schurig) cloak reduces the scattered power for angles of incidence 69º - 111º , while the TEz (Cai) cloak reduces the scattered power for angles of incidence 77º - 103º.

We have also optimized the cloak dimensions for the angle of incidence that is different from the normal incidence. As an example we have considered a cloak with the reduced variation of constitutive parameters for TM_z polarization (i.e. the cloak which structure is similar to the Schuring's cloak). In table 5.1 we have compared the cloak parameters optimized for incidence angle 90º and 75º, respectively. The difference between structure parameters is not too large, i.e. both structures have the same level of complexity. The comparison between scattered widths of these two structures is given in Figure 5.9 (both of them are excited form the direction used in the cloak design). It can be seen that larger reduction of scattered field can be obtianed for normal incidence, i.e. when the incident wave follows the symmetry of the cloak.

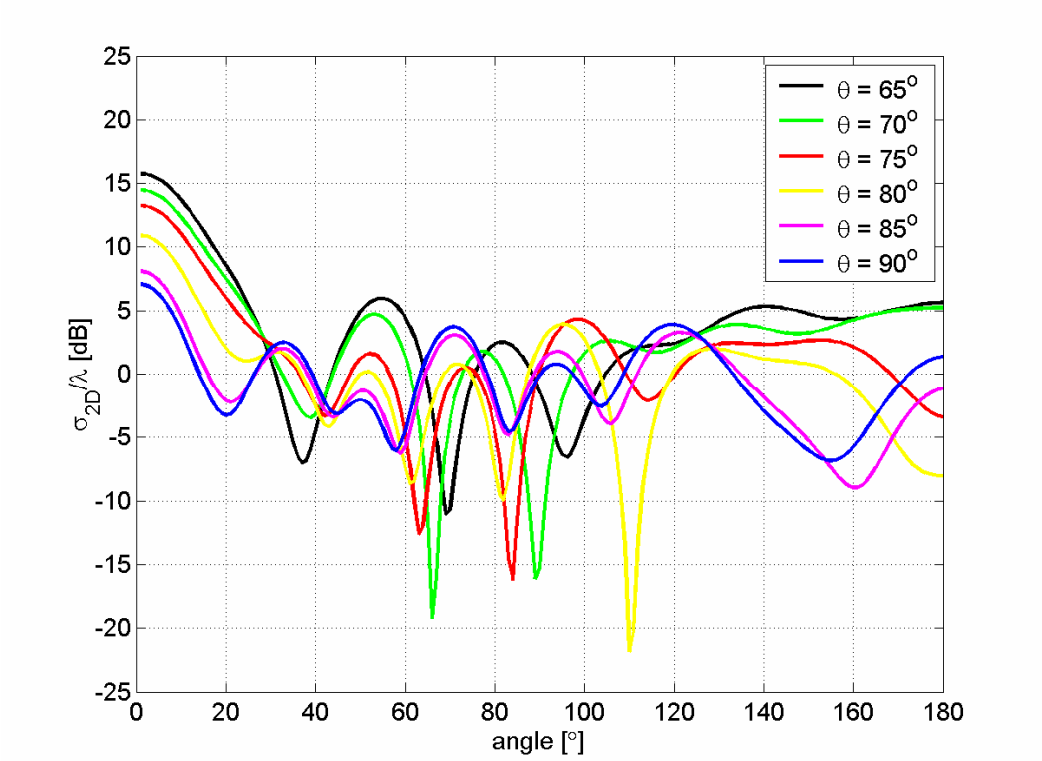

Figure 5.5. Normalized scattering width vs. angle of incidence for the Schurig cloak.

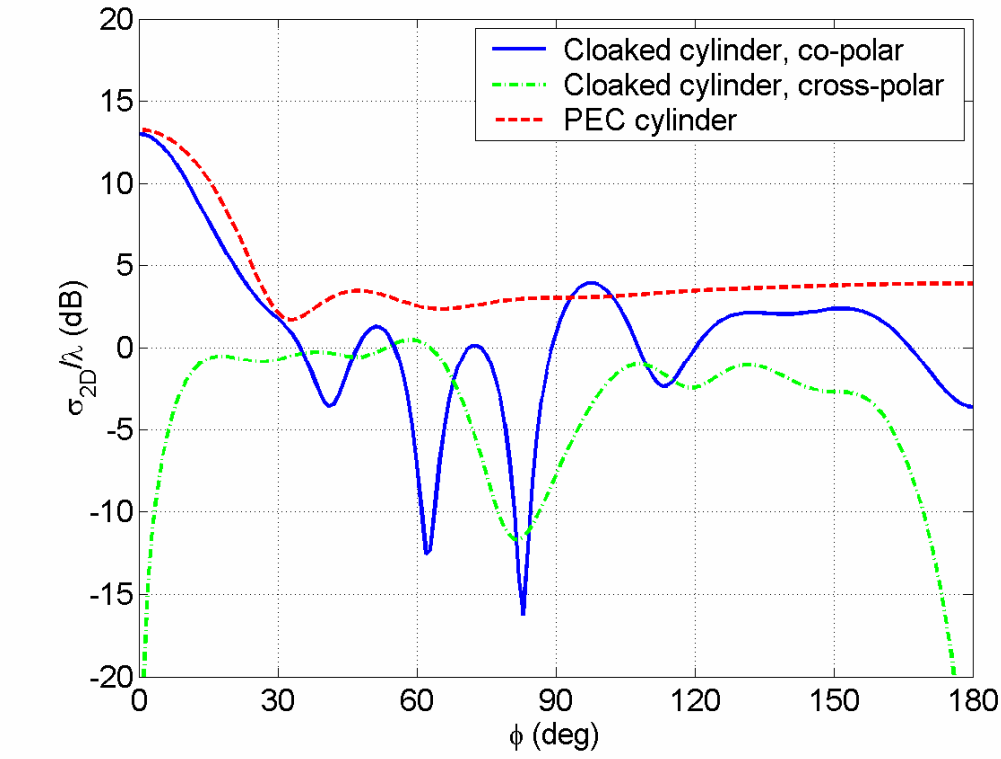

Figure 5.6. Comparison of the normalized scattering width of the Schurig cloak and of the bare PEC cylinder (incident angle is 75º).

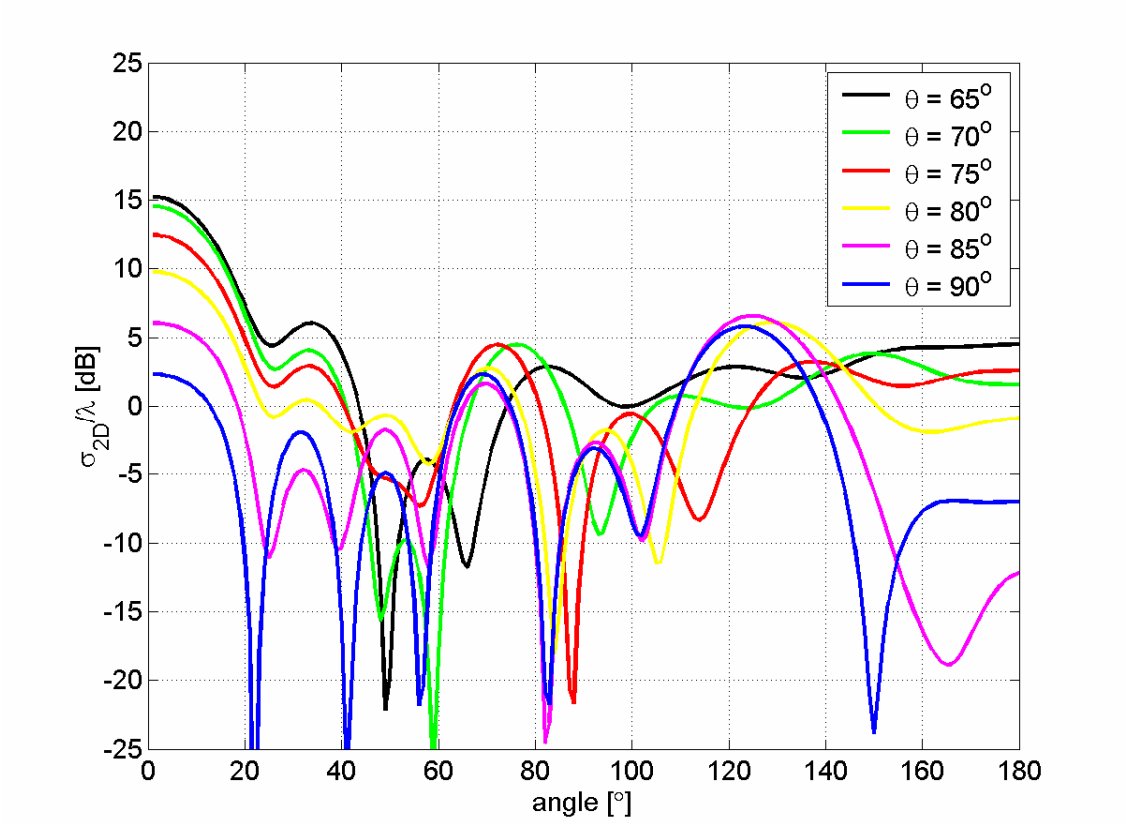

Figure 5.7. Normalized scattering width vs. angle of incidence for the TE_z cloak

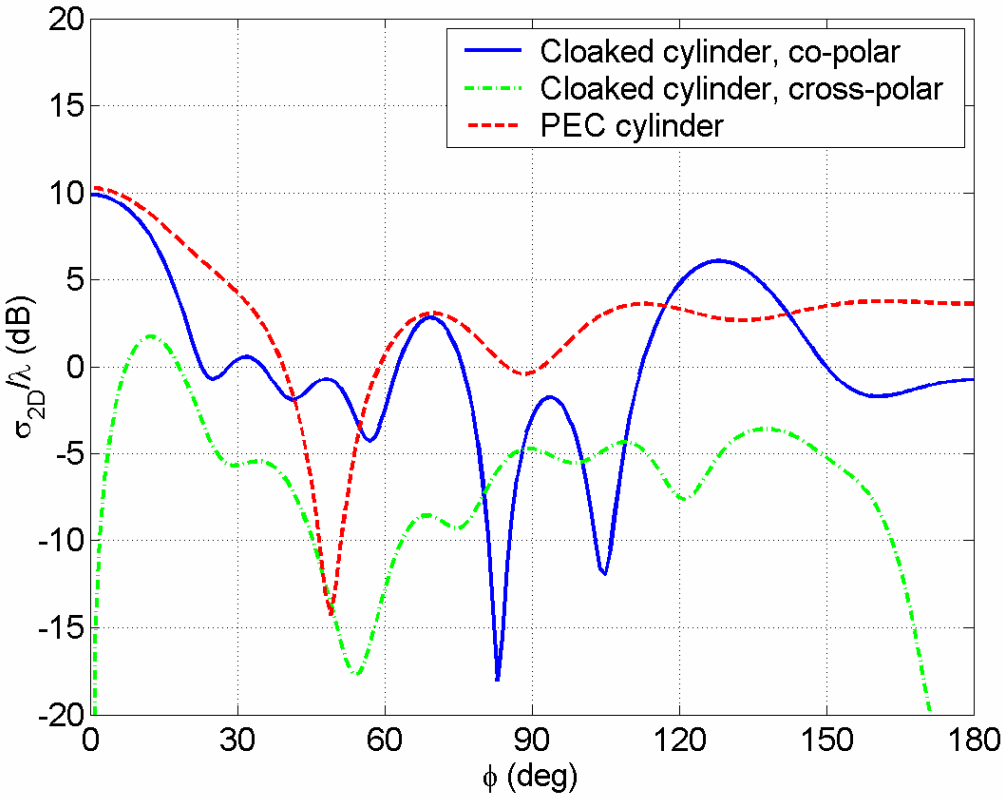

Figure 5.8. Comparison of the normalized scattering width of the TE_z cloak and of the bare PEC cylinder (incident angle is 80º).

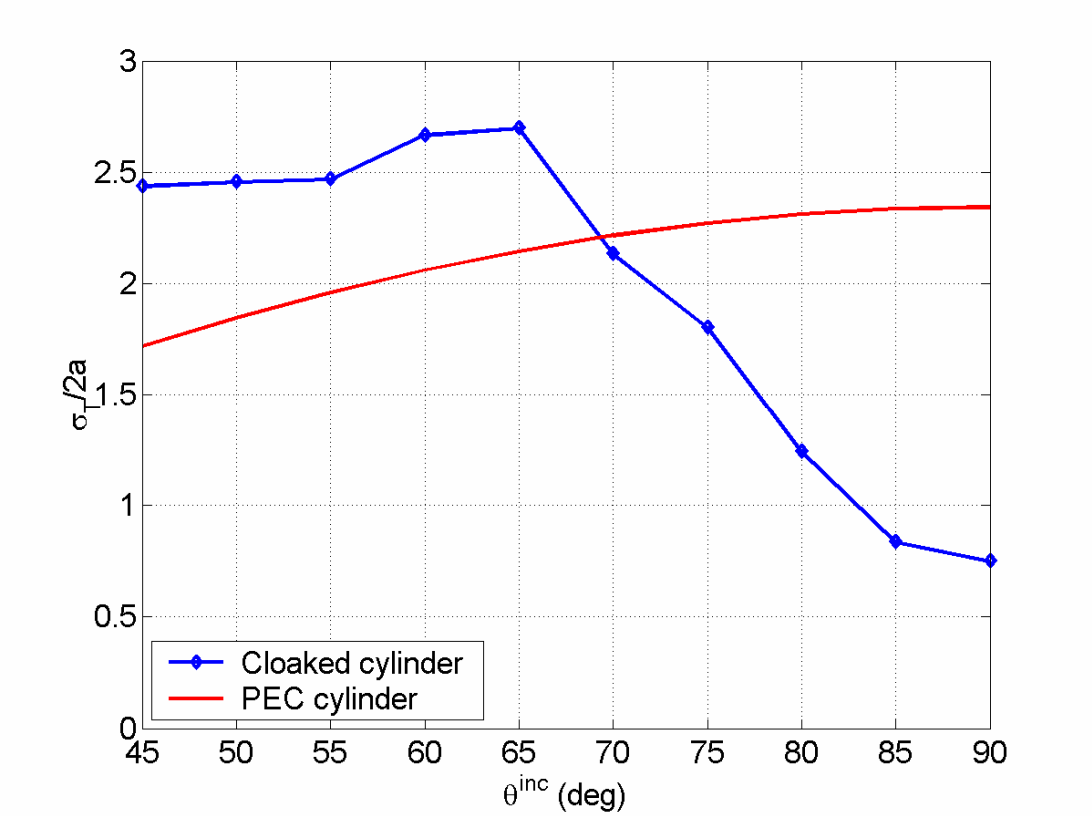

Figure 5.9. Total scattering width $\sigma_T/2a$ vs. angle of incidence for the TM_z cloak

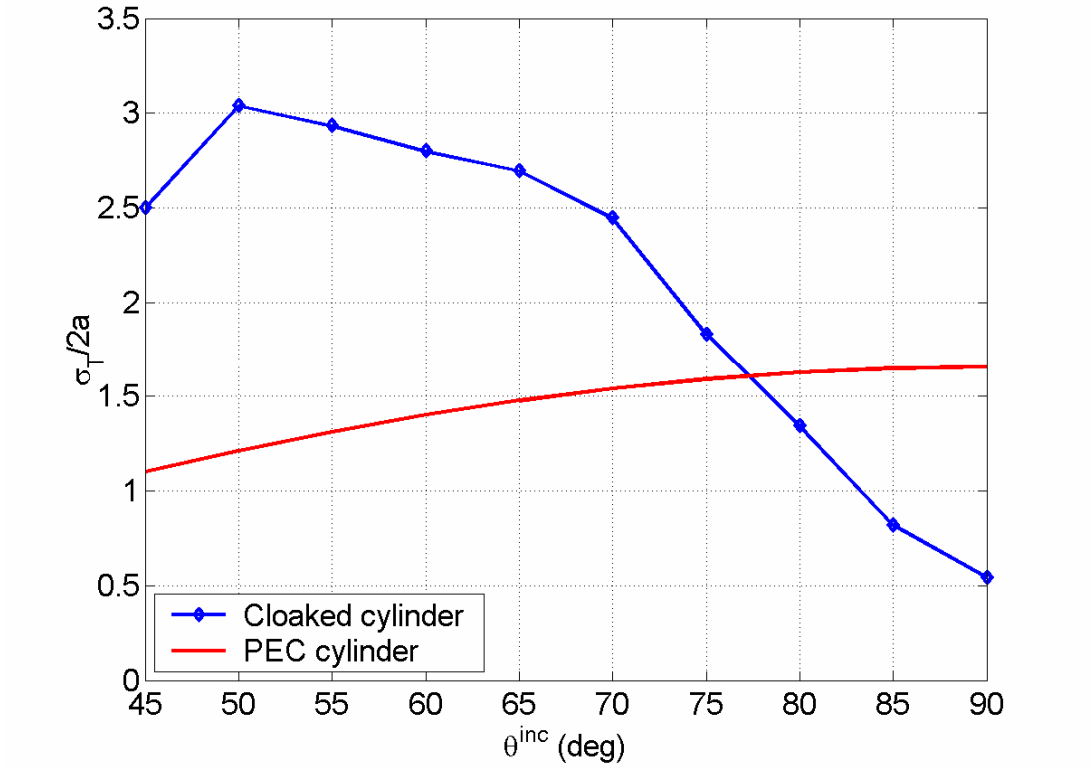

Figure 5.10. Total scattering width $\sigma_T/2a$ vs. angle of incidence for the TE_z cloak

Layer No.	**Optimized cloak for** $\theta^{inc} = 75°$	**Optimized cloak for** $\theta^{inc} = 90°$
	ε_z =3.433; μ_ϕ =1.0	ε_z =3.841; μ_ϕ =1.0
	μ_r	μ_r
1	0.065	0.021
2	0.156	0.123
3	0.255	0.218

Table 5.1. Relevant constitutive parameters of the 3-layer cloaks optimized for incidence angles $\theta^{inc} = 75°$ and $\theta^{inc} = 90°$, respectively.

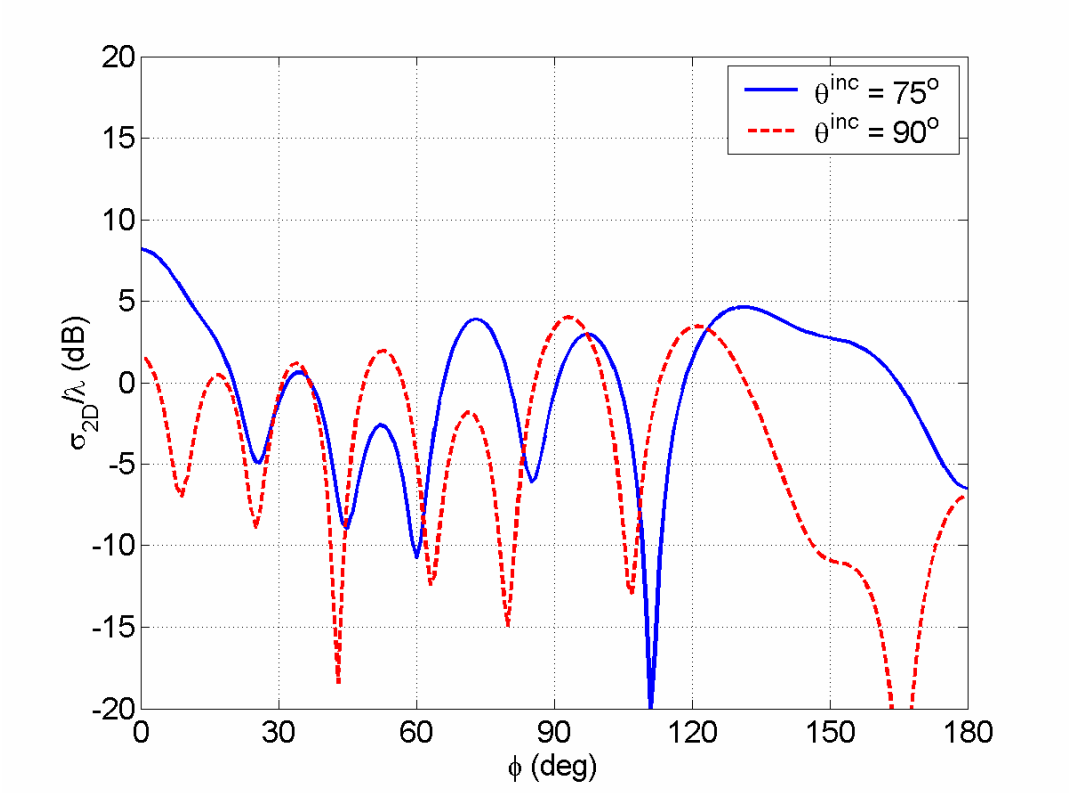

Figure 5.11. Normalized scattering width σ_{2D}/λ of two cloaks optimized for incidence angles 90º and 75º, respectively. Both cloaks are excited form the directions used in the cloak design.

6 ANALYSIS OF UNIAXIAL MULTILAYER SPHERICAL STRUCTURES USED FOR INVISIBLE CLOAK REALIZATION

Analysis of uniaxial multilayer spherical structures used for invisible cloak realization

6.1. INTRODUCTION

The already presented cloak designs and optimizations are based on the analysis of plane wave scattering by a circular cylinder, which is a two-dimensional problem. Such approach simplifies the required procedure and enables reasonably accurate approximation for cylinder-like objects. However, for scatterers of arbitrary geometry two-dimensional approximation is not general enough, which leads to requirement for full three-dimensional scattering analysis.

This chapter presents the generalization of the analysis and optimizations to three dimensions. The analysis focuses on calculating bistatic scattering cross sections for various cloak realizations and investigating the possibility of optimizing cloak parameters to improve the invisibility performance. For these purposes, the program for analyzing spherical structures was developed and the optimization algorithm was connected with the extended version of the program.

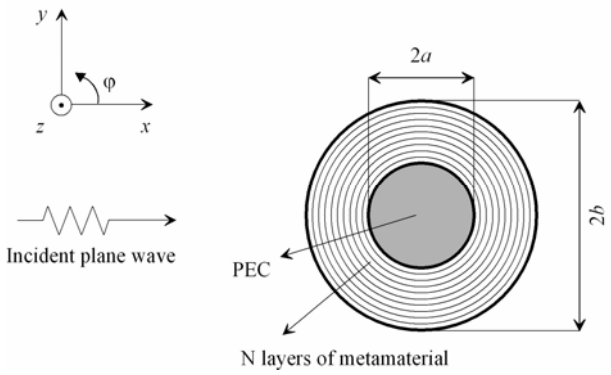

Figure 6.1. The cross section of the analyzed spherical structure.

6.2. THEORETICAL CONSIDERATIONS

6.2.1. Vector eigenvectors

When solving some differential equation such as e.g. wave equation, one of the common methods is to find some appropriate set of linearly independent functions (eigenfunctions) in terms of which it is possible to express any solution (function). By applying such method, to obtain some particular solution (due to source terms or boundary conditions) one only needs to find the coefficients corresponding to each term of the eigenfunction, i.e. differential equation could be in principle be reduced to algebraic one.

In this section we will show how to construct the eigenfunctions for vector wave equation that is satisfied by the electric and magnetic field. Let $\mathbf{C}\equiv\mathbf{C}(\mathbf{r})$ be some vector field that satisfies the homogeneous vector Helmholtz equation (it represents e.g. electric or magnetic field or vector potential in the absence of sources):

$$\nabla^2\mathbf{C}+k^2\mathbf{C}=0 \tag{6.1}$$

where k is called wavenumber (in general it is a complex number).

As mentioned above, the idea is to find some complete set of vectors in terms of which it is possible to expand any vector $\mathbf{C}$ that satisfies (6.1). As a basis for such expansion we first find the scalar function ψ which satisfies the scalar Helmholtz equation (subject to some boundary conditions):

$$\nabla^2\psi+k^2\psi=0 \tag{6.2}$$

Using scalar function ψ and defining some constant vector $\mathbf{a}$ it is possible to derive three sets of mutually linearly independent vector functions [41] each of which individually satisfies (6.1.):

$$\begin{aligned}\mathbf{L}&=\nabla\psi\\ \mathbf{M}&=\nabla\times\mathbf{a}\psi\\ \mathbf{N}&=\frac{1}{k}\cdot\left(\nabla\times\nabla\times\mathbf{a}\psi\right)=\frac{1}{k}\cdot\left(\nabla\times\mathbf{M}\right)\end{aligned} \tag{6.3}$$

The **L**, **M** and **N** vectors also have the following properties which arise due to their definition:

a) **L** is irrotational, i.e. $\left(\nabla\times\mathbf{L}\right)=0$

b) **M** and **N** are solenoidal, i.e. $\nabla\cdot\mathbf{M}=\nabla\cdot\mathbf{N}=0$

c) Since **a** is presumed constant, vector **M** could also be written as: $\mathbf{M}=\mathbf{L}\times\mathbf{a}=\frac{1}{k}\cdot\left(\nabla\times\mathbf{N}\right)$

d) Vector **M** is perpendicular to **L**, i.e. $\mathbf{L}\cdot\mathbf{M}=0$. Also, **M** is perpendicular to **a**.

If by solving (6.2) we find some set of scalar functions $\{\psi_n\}$ which form a complete set in the Hilbert space, it can be shown that any vector field **C** that satisfies (6.1) could be represented by a linear combination of **L**, **M** and **N** vectors that correspond to each scalar ψ_n in the set, i.e.

$$\mathbf{C} = \sum_n \left(a_n \mathbf{M}_n + b_n \mathbf{N}_n + c_n \mathbf{L}_n \right) \tag{6.4}$$

where a_n, b_n and c_n are coefficients to be determined.

Now we turn our attention to the electric and magnetic fields in region without sources where they are described by the following equations (we assume time-harmonic case and, in first case, the isotropic medium):

$$\begin{aligned} \nabla \times \mathbf{E} &= -j\omega\mu\mathbf{H} \\ \nabla \times \mathbf{H} &= j\omega\varepsilon\mathbf{E} \\ \nabla \cdot \mathbf{E} &= \nabla \cdot \mathbf{H} = 0 \end{aligned} \tag{6.5}$$

Since in the source free regions divergence of the electric and magnetic field is zero, it is possible to write them as a curl of another vector (divergence of the curl is always zero). If we define vectors **A** and **F** such that:

$$\begin{aligned} \mathbf{H} &= \frac{1}{\mu} \nabla \times \mathbf{A} \\ \mathbf{E} &= -\frac{1}{\varepsilon} \nabla \times \mathbf{F} \end{aligned} \tag{6.6}$$

for each vector we can derive an independent solution for both electric and magnetic field, by inserting them into Maxwell's equations and applying Lorenz condition. Physically, vectors **A** and **F** represent potentials that arise due to electric and magnetic sources, respectively. The total field in the region without sources turns out to be the superposition of the fields that arise from **A** and **F**:

$$\begin{aligned} \mathbf{E} &= \mathbf{E}_A + \mathbf{E}_F = \frac{1}{j\omega\mu\varepsilon} \nabla \times \nabla \times \mathbf{A} - \frac{1}{\varepsilon} \nabla \times \mathbf{F} \\ \mathbf{H} &= \mathbf{H}_A + \mathbf{H}_F = \frac{1}{\mu} \nabla \times \mathbf{A} - \frac{1}{j\omega\mu\varepsilon} \nabla \times \nabla \times \mathbf{F} \end{aligned} \tag{6.7}$$

Now we make a particular choice for **A** and **F**:

$$\begin{aligned} \mathbf{A} &= \psi_{TM} \cdot \mathbf{a} \\ \mathbf{F} &= \psi_{TE} \cdot \mathbf{a} \end{aligned} \tag{6.8}$$

where ψ_{TM} and ψ_{TE} are scalar functions that both satisfy Helmholtz equation (6.2) and **a** is some constant vector. The expression (6.7) could now be rewritten as:

$$\begin{aligned}\mathbf{E} &= \frac{1}{j\omega\mu\varepsilon}\nabla\times\nabla\times\left(\psi_{TM}\cdot\mathbf{a}\right)-\frac{1}{\varepsilon}\nabla\times\left(\psi_{TE}\cdot\mathbf{a}\right)\\ \mathbf{H} &= \frac{1}{\mu}\nabla\times\left(\psi_{TM}\cdot\mathbf{a}\right)-\frac{1}{j\omega\mu\varepsilon}\nabla\times\nabla\times\left(\psi_{TE}\cdot\mathbf{a}\right)\end{aligned} \tag{6.9}$$

Comparing the (6.9) with (6.3) we immediately find that it is possible to define equivalent vector functions e.g. $\mathbf{M}_{TE}=\nabla\times\left(\psi_{TE}\cdot\mathbf{a}\right)$ and $\mathbf{N}_{TM}=\nabla\times\nabla\times\left(\psi_{TM}\cdot\mathbf{a}\right)$ in terms of which it is possible to expand the electric and magnetic field in the way as described in (6.4). Such expansion is of the form:

$$\begin{aligned}\mathbf{E} &= \sum_n\left(a_n\mathbf{M}_{TE,n}+b_n\mathbf{N}_{TM,n}\right)=\mathbf{E}_{TE}+\mathbf{E}_{TM}\\ \mathbf{H} &= -\frac{k}{j\omega\mu}\sum_n\left(a_n\mathbf{N}_{TE,n}+b_n\mathbf{M}_{TM,n}\right)=\mathbf{H}_{TE}+\mathbf{H}_{TM}\end{aligned} \tag{6.10}$$

We also note that:

a) the expansion (6.10) is a bit more general than (6.4) in the sense that two generating scalar functions (ψ_{TM} and ψ_{TE}) are actually needed (however they only differ to some multiplicator).

b) in such expansion terms in vector **L** are zero, which is expected since divergence of **L** by definition is not generally zero unlike the divergence of electric and magnetic field.

c) Since vector **M** is perpendicular to the constant vector **a** we denote the respective terms of the field expansion in **M** (and accordingly their **N** counterparts) as transverse electric (TE) or transverse magnetic (TM) to **a**. This means that each field is decomposed to the TE part and TM part (generated by ψ_{TE} and ψ_{TM}, respectively).

To summarize the above considerations, we note that the problem of solving for electric and magnetic fields can be formulated as:

a) fixing the appropriate constant vector **a**
b) finding the complete sets of scalar functions ψ_{TE} and ψ_{TM} by solving homogeneous scalar Helmholtz equation
c) expanding the field in TE and TM parts (so-called magnetic and electric multipoles, respectively) and determining coefficients such as a_n and b_n by applying the given boundary conditions or expanding the given source functions.

6.2.2. Spherical harmonics

The scalar functions ψ in the expansion of the fields (6.10) as well as suitable choices of vector **a** depend on the choice of coordinate system. In this section we describe procedure for spherical coordinate system (r,φ,θ) and seek for expansion of the fields in free space in terms of spherical eigenfunctions, i.e. spherical harmonics. The procedure described above requires finding some fixed vector **a**. Although any vector **a** can be chosen in principle, in spherical coordinate system it is not possible to find such vector that would a priori generate

independent vectors **M** and **N** across the whole surface of the sphere – if e.g. we use radial unit vector $\hat{\mathbf{r}}$, we find that it is not constant across the sphere. Similar issues arise also in more general coordinate systems.

Nevertheless, for spherical coordinate systems in particular it can be found that from radial vector it is actually still possible to construct appropriate vectors **M** and **N** that are independent across the spherical surface. We try to construct vector **M** tangential to sphere (which is proportional to e.g. electric or magnetic field) of the following form:

$$\mathbf{M} = \nabla \times \hat{\mathbf{r}} u(r) \psi \tag{6.11}$$

i.e. we have chosen non-constant vector of the form $\mathbf{a}=u(r)\cdot\hat{\mathbf{r}}$, where $u(r)$ is some radial function, yet undetermined. After some derivation it can be shown that with selection $u(r)$ = r the function ψ satisfies the scalar Helmholtz differential equation [41], [42].

Now we need to find the complete set of functions ψ that satisfy scalar Helmholtz equation (6.14c) in spherical coordinates. The typical procedure is the method of separation of variables. We assume that the function $\psi \equiv \psi(\mathbf{r})$ can be written as a product of three functions of r-, θ- and φ- coordinates, respectively:

$$\psi = f(r) \cdot g(\theta) \cdot h(\varphi) \tag{6.12}$$

This form of ψ is then inserted in Helmholtz equation in spherical coordinates, and after some manipulations one obtains three independent equations for functions f, g and h:

a) 1D Helmholtz equation

$$\frac{\partial^2 h}{\partial \varphi^2} + m^2 h = 0 \tag{6.13a}$$

b) Legendre differential equation

$$\frac{1}{\sin\theta}\frac{\partial}{\partial\theta}\left[\sin\theta\frac{\partial g}{\partial\theta}\right] + \left[n(n+1) - \left(\frac{m}{\sin\theta}\right)^2\right] g = 0 \tag{6.13b}$$

c) Spherical Bessel differential equation

$$\frac{\partial^2 f}{\partial r^2} + \frac{2}{r}\frac{\partial f}{\partial r} + \left[k^2 - \frac{n(n+1)}{r^2}\right] f = 0 \tag{6.13c}$$

Here m^2 and $n(n+1)$ are separation constants, while m,n are integers. The solutions of (6.13a) are harmonic functions $h(\varphi) = e^{-jm\varphi}$, while the solutions (6.13b) are Legendre functions of the first and second kind $g(\theta) = P_n^m(\cos\theta)$ and $g(\theta) = Q_n^m(\cos\theta)$ (the latter ones give the non-physical solution due to singularity at $\theta = 0^\circ$ and $\theta = 180^\circ$). Finally, the solutions of (6.13c) are spherical Bessel and Hankel functions of the first and second kind $f(r) = h_n^{(1)}(kr)$

and $f(r) = h_n^{(2)}(kr)$. We choose solutions in accordance to physical reality of the problem in question (outgoing wave in free space, no singularities on the spherical surface) and write the normalized solution for ψ as:

$$\psi_{mn} = f(r) \cdot g(\theta) \cdot h(\varphi) = h_n^{(2)}(kr) \cdot P_n^m(\cos\theta) \cdot e^{-jm\varphi} \tag{6.14}$$

Note that actual solution is actually multiple of ψ_{mn}. If one needs to take into account standing waves in some spherical layer, then spherical Bessel functions $j_n(kr)$ should be also considered.

Spherical vector eigenfunctions **L**, **M** and **N** can be now constructed from each ψ_{mn}, i.e. by inserting (6.14) into (6.11) and (6.3). Therefore, we have by now obtained proper mathematical tool to expand any vector function in spherical coordinates as a sum of vector eigenfunctions. The remaining task is to apply the developed tool to potential and field equations and to obtain required field expressions in terms of vector eigenfunctions.

In accordance with discussions described above we expand potentials **A** and **F** as:

$$\begin{aligned} \mathbf{A} &= \psi_{TM} \cdot \mathbf{r} = \sum_{m,n} B_{mn} \psi_{mn} \cdot r\hat{\mathbf{r}} \\ \mathbf{F} &= \psi_{TE} \cdot \mathbf{r} = \sum_{m,n} A_{mn} \psi_{mn} \cdot r\hat{\mathbf{r}} \end{aligned} \tag{6.15}$$

where A_{mn} and B_{mn} are coefficients to be determined.

We note that the potentials contain only the radial component. The final expansion of the electric and magnetic field is then obtained by inserting (6.15) into (6.9) which is the expression for electric and magnetic field in terms radial components of potentials that provide decomposition to TE and TM (to *r*-coordinate) parts. The expression is of the form (6.10) only with double index *mn*. The coefficients in the expansion are then obtained by applying boundary conditions or by expanding the (known) source terms in spherical harmonics and finding the field coefficients that correspond to each source term (i.e. differential equation is then reduced to algebraic one).

As a final remark, the radial dependence in (6.14) is often incorporated in modified form of spherical Hankel functions (so-called Schelkunoff form):

$$\hat{H}_n^{(2)}(kr) = kr \cdot h_n^{(2)}(kr) \tag{6.16}$$

The connection between spherical Hankel functions in Schelkunoff and ordinary form $\hat{H}_n^{(2)}$ and $h_n^{(2)}$ with the regular (cylindrical) functions $H_n^{(2)}$ is given by:

$$\hat{H}_n^{(2)}(kr) = kr \cdot h_n^{(2)}(kr) = kr \cdot \sqrt{\frac{\pi}{2kr}} H_{n+\frac{1}{2}}^{(2)}(kr) = \sqrt{\frac{kr\pi}{2}} H_{n+\frac{1}{2}}^{(2)}(kr) \tag{6.17}$$

The same relation as (6.17) holds also for other types of Bessel/Hankel functions. The Bessel/Hankel functions of the Schelkunoff form are solutions to the slightly modified equation compared to (6.13c):

$$\frac{\partial^2 f}{\partial r^2}+\left[k^2-\frac{n(n+1)}{r^2}\right]f=0 \tag{6.18}$$

Note that the expansions of the type (6.15) are only slightly changed by employing the Schelkunoff form of Hankel functions instead of the ordinary ones (only the coefficients such as A_{mn} or B_{mn} are different and r is incorporated in Hankel functions).

6.2.3. Modifications for anisotropic structures

In this section we consider the extension of the above described method of field expansion to the anisotropic structures. In particular, we consider uniaxial structures where electric permittivity and magnetic permeability are given by the tensors of the form:

$$\overline{\overline{\varepsilon}}=\varepsilon_0\begin{bmatrix}\varepsilon_r & 0 & 0\\ 0 & \varepsilon_t & 0\\ 0 & 0 & \varepsilon_t\end{bmatrix} \tag{6.19a}$$

$$\overline{\overline{\mu}}=\mu_0\begin{bmatrix}\mu_r & 0 & 0\\ 0 & \mu_t & 0\\ 0 & 0 & \mu_t\end{bmatrix}, \tag{6.19b}$$

which means that the radial (r-) and transverse (φ- and θ-) components of the fields "see" different properties of the medium when propagating through such media. The curl Maxwell equations in the region without sources are now of the form similar to (6.5):

$$\begin{aligned}\nabla\times\mathbf{E}&=-j\omega\overline{\overline{\mu}}\mathbf{H}\\ \nabla\times\mathbf{H}&=j\omega\overline{\overline{\varepsilon}}\mathbf{E}\end{aligned} \tag{6.20}$$

The idea is to expand electric in magnetic fields in spherical eigenvectors according to procedure described in previous sections. To make such expansion, one needs to obtain proper differential equation for the anisotropic case. To make dealing with tensors more convenient, we make use of the flux density vectors $\mathbf{B}=\overline{\overline{\mu}}\mathbf{H}$ and $\mathbf{D}=\overline{\overline{\varepsilon}}\mathbf{E}$ rather than fields **E** and **H**, and thus rewrite the curl equations as:

$$\begin{aligned}\nabla\times\left[\overline{\overline{\varepsilon}}^{-1}\cdot\mathbf{D}\right]&=-j\omega\mathbf{B}\\ \nabla\times\left[\overline{\overline{\mu}}^{-1}\cdot\mathbf{B}\right]&=j\omega\mathbf{D}\end{aligned} \tag{6.21}$$

In accordance to the procedure previously described, we now choose potentials with radial components only, by which we construct independent expressions for the TE (from F_r) and TM (from A_r) fields. The potentials (6.15) are therefore written as:

$$\begin{aligned}\mathbf{A} &= \psi_{TM} \cdot r\hat{\mathbf{r}} = A_r \cdot \hat{\mathbf{r}} \\ \mathbf{F} &= \psi_{TE} \cdot r\hat{\mathbf{r}} = F_r \cdot \hat{\mathbf{r}}\end{aligned} \tag{6.22}$$

while with such choice of potentials the TE and TM flux density vectors are then given corresponding to (6.6) as

$$\begin{aligned}\mathbf{B}_{TM} &= \nabla \times \mathbf{A} = \nabla \times \left(A_r \cdot \hat{\mathbf{r}} \right) \\ \mathbf{D}_{TE} &= -\nabla \times \mathbf{F} = -\nabla \times \left(F_r \cdot \hat{\mathbf{r}} \right)\end{aligned} \tag{6.23}$$

Now we substitute (6.23) into (6.21) and obtain respective TM and TE counterparts of (6.23):

$$\begin{aligned}\mathbf{B}_{TE} &= \frac{1}{j\omega} \nabla \times \left(\overline{\overline{\varepsilon}}^{-1} \cdot \left(\nabla \times F_r \hat{\mathbf{r}} \right) \right) \\ \mathbf{D}_{TM} &= \frac{1}{j\omega} \nabla \times \left(\overline{\overline{\mu}}^{-1} \cdot \left(\nabla \times A_r \hat{\mathbf{r}} \right) \right)\end{aligned} \tag{6.24}$$

Using (6.21) we can choose to establish the following relations between TM and TE parts of **D** and **B** and thus obtain decoupled expressions in terms of **A** and **F**, respectively:

$$\begin{aligned}\nabla \times \left[\overline{\overline{\varepsilon}}^{-1} \cdot \mathbf{D}_{TM} \right] &= -j\omega \mathbf{B}_{TM} \\ \nabla \times \left[\overline{\overline{\mu}}^{-1} \cdot \mathbf{B}_{TE} \right] &= j\omega \mathbf{D}_{TE}\end{aligned} \tag{6.25}$$

The equations (6.25) are now expanded using (6.24) and (6.23) and, since radial component of the left sides is zero (due to definition of TM and TE cases), after some algebraic manipulations we arrive to the differential equations for A_r and F_r (i.e. for ψ_{TM} and ψ_{TE}):

$$\frac{\varepsilon_r}{\varepsilon_t} \frac{\partial^2 A_r}{\partial r^2} + \frac{1}{r^2 \sin\theta} \frac{\partial}{\partial \theta} \left[\sin\theta \frac{\partial A_r}{\partial \theta} \right] + \frac{1}{r^2 \sin^2\theta} \frac{\partial^2 A_r}{\partial \varphi^2} + k_0{}^2 \mu_t \varepsilon_r A_r = 0 \tag{6.26a}$$

$$\frac{\mu_r}{\mu_t} \frac{\partial^2 F_r}{\partial r^2} + \frac{1}{r^2 \sin\theta} \frac{\partial}{\partial \theta} \left[\sin\theta \frac{\partial F_r}{\partial \theta} \right] + \frac{1}{r^2 \sin^2\theta} \frac{\partial^2 F_r}{\partial \varphi^2} + k_0{}^2 \mu_r \varepsilon_t F_r = 0 \tag{6.26b}$$

where $k_0{}^2 = \omega^2 \mu_0 \varepsilon_0$.

By comparison with Helmholtz equation in spherical coordinates (6.13) we note that the expressions (6.26) can be easily shown (by doing some rewriting) to be actually equivalent, except for the factors $\varepsilon_r/\varepsilon_t$ and μ_r/μ_t (so-called anisotropy ratios) in the term of the second radial derivative. We also note that TE and TM functions do not satisfy the same equation in terms of medium parameters, as was the case in isotropic media.

Using the separation of variables method, one obtains the same θ- and φ- dependence as in (6.13a) and (6.13b), while for r-dependence the following equations for radial dependences of A_r and F_r are obtained:

$$\frac{\partial^2 A_r}{\partial r^2} + \left[k_0^2 \varepsilon_t \mu_t - \frac{\varepsilon_t}{\varepsilon_r} \frac{n(n+1)}{r^2} \right] A_r = 0 \tag{6.27a}$$

$$\frac{\partial^2 F_r}{\partial r^2} + \left[k_0^2 \varepsilon_t \mu_t - \frac{\mu_t}{\mu_r} \frac{n(n+1)}{r^2} \right] F_r = 0 \tag{6.27b}$$

These equations turn to be spherical Bessel differential equations of Schelkunoff form (6.18). The solutions are then spherical Bessel/Hankel functions. For both cases the argument is:

$$k_0 \sqrt{\mu_t \varepsilon_t} r = k_t r \tag{6.28}$$

On the other hand, the orders of Bessel/Hankel function is different for each case:

a) for TM case:

$$\nu_1 = \left[n(n+1) \frac{\varepsilon_t}{\varepsilon_r} + \frac{1}{4} \right]^{\frac{1}{2}} - \frac{1}{2} \tag{6.29a}$$

b) for TE case:

$$\nu_2 = \left[n(n+1) \frac{\mu_t}{\mu_r} + \frac{1}{4} \right]^{\frac{1}{2}} - \frac{1}{2} \tag{6.29b}$$

We also note that the resulting orders are not integers. Now we can construct the set of eigenfunctions in terms of which expand radial vector potentials are expanded according to procedure described for isotropic case. The expansions are of the form:

$$\begin{aligned} A_r &= \psi_{TM} r = \sum_{m,n} B_{mn} \hat{H}^{(2)}_{\nu_1}(k_t r) \cdot P_n^m(\cos\theta) \cdot e^{-jm\varphi} \\ F_r &= \psi_{TE} r = \sum_{m,n} A_{mn} \hat{H}^{(2)}_{\nu_2}(k_t r) \cdot P_n^m(\cos\theta) \cdot e^{-jm\varphi} \end{aligned} \tag{6.30}$$

The Hankel functions of the second kind represent waves traveling outside the sphere. For fields expansions inside the sphere one only needs to add terms with Bessel functions of the first kind, $\hat{J}_{\nu_1}$ and $\hat{J}_{\nu_2}$, which represent the standing waves.

The remaining task is to construct vector eigenfunctions **M** and **N** and expand the electric and magnetic field in terms of them. Since we are dealing with anisotropic media the intermediate step consists of expressing the flux density vectors **B** and **D** according to (6.23) and (6.24) by which the actual fields follow due to properties of TE and TM cases as:

$$\mathbf{E}_{TE} = \frac{1}{\varepsilon_t}\mathbf{D}_{TE}$$
$$\mathbf{H}_{TM} = \frac{1}{\mu_t}\mathbf{B}_{TM} \tag{6.31}$$

The rest of the procedure is the same as in the isotropic case described in the previous section, while the final expansion is of the form as given in (6.10), only with double indexes (*mn*).

6.2. RESULTS OF THE CLOAK ANALYSIS

6.2.1. Pendry cloak design

For analysis of cloaking of three-dimensional objects, cloaking of a PEC sphere of 0.75λ radius (i.e. a=2.645 cm at the frequency of 8.5 GHz) was considered and few configurations were compared. The achieved invisibility is expressed in terms of bistatic scattering cross section σ_{3D} (normalized to the cross-section of the PEC sphere) [17]. In the first configuration, the cloak constitutive parameters have been calculated by using coordinate transformations given in [9] (so-called Pendry design) which required radial variations of radial components of the permittivity and permeability tensor, respectively, while keeping transverse components constant:

$$\varepsilon_r = \mu_r = \frac{b}{b-a}\left(\frac{r-a}{r}\right)^2$$
$$\varepsilon_\theta = \mu_\theta = \frac{b}{b-a} \tag{6.32}$$
$$\varepsilon_\varphi = \mu_\varphi = \frac{b}{b-a}$$

These variations were approximated by piecewise constant functions representing the number of cloak layers. In Fig. 6.2 comparison of the obtained bistatic cross section for the uncloaked PEC sphere and the one cloaked with Pendry design is shown. The influence of the cloak thickness was also taken into account. For thick cloak design (outer radius of 2a) the forward scattered field (0° direction) is even larger than the one of the PEC sphere itself which actually makes it unsuitable for cloaking purposes. On the other hand, for thin cloak design (outer radius of 1.06a) both forward (shadow) and backward (reflection) scattered field are significantly reduced, since thin cloaks occupy smaller region of space. Therefore thin cloaks are more interesting for further study.

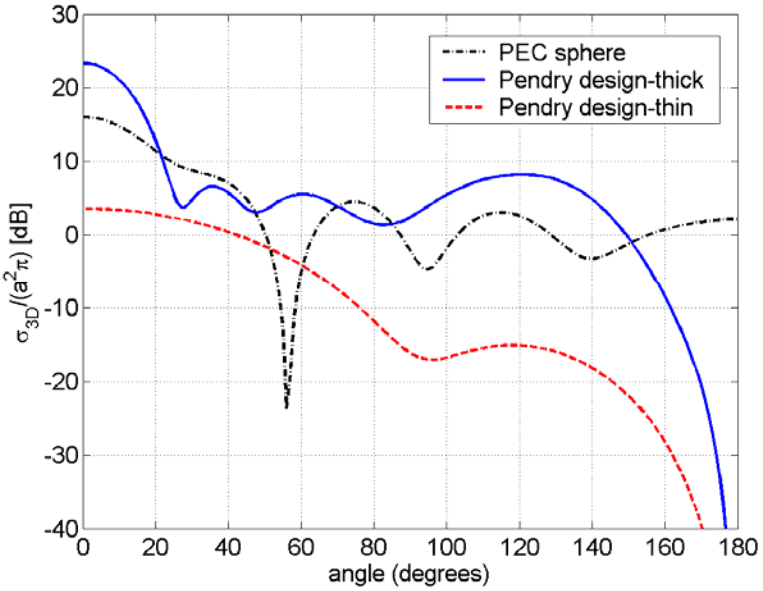

Figure 6.2 Normalized bistatic scattering cross section of PEC sphere and two versions of Pendry cloak design

6.2.2. Engheta cloak

Another approach to cloaking is based on expanding the scattered field in electric and magnetic multipoles and reducing the magnitude of several relevant multipoles [43] via optimizing the cloak constitutive parameters and required thickness (so-called Engheta cloak). The comparison between performance of the Engheta cloak proposed in [43] and the Pendry-designed thin cloak (5 layers) is given in Fig. 6.3. For both cloaks the outer radius is 1.06*a*. It should be noted that although Pendry cloak design provides much better invisibility performance (Fig. 6.3), Engheta cloak is one-layered and isotropic [43], which results in much simpler design in practice.

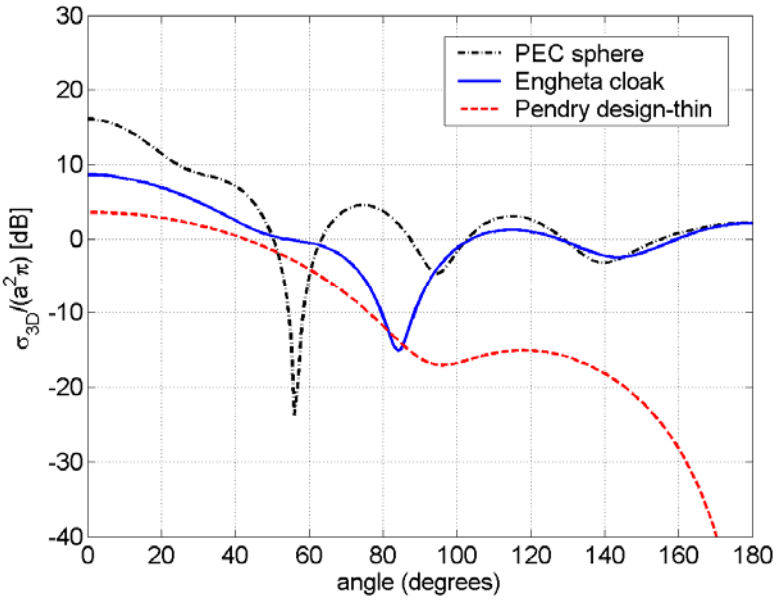

Figure 6.3 Normalized bistatic scattering cross section of PEC sphere, Engheta cloak and the Pendry (thin) design

6.2.3. Optimized cloak

As suggested in [43], the technique described above could be improved by introducing more cloak layers and allowing material anisotropy. Such extension was carried out in this paper. By using the developed PSO algorithm we have considered cases with various numbers of anisotropic layers and have optimized the permittivity and permeability tensor components in order to achieve minimum scattering cross section. The overall cloak thickness was kept consistent to previous configurations (i.e. outer radius of 1.06*a*). It was found that with only two layers it is possible to find such combination of parameters (Table 6.1) that enables significant scattering cross section reduction for both forward and backward direction. In comparison with Pendry cloak design (5 layers) given in Fig. 6.4, forward scattering has been even more reduced while the practical realization of 2-layers optimized cloak should be simpler (although anisotropic dielectric and magnetic materials are required). For illustration, in Fig. 6.5 the field plots around the structures for the two best obtained cloak configurations as well as PEC sphere are given in terms of total field (i.e. incident+scattered field), and scattered field itself.

Layer No.	Outer radius [cm]	Relative permittivity		Relative permeability	
		Transverse	Radial	Transverse	Radial
1	2.7328	3.9223	3.0994	2.3165	1.8378
2	2.8006	3.9223	0.9086	2.3165	0.8540

Table 6.1 Constitutive parameters of the optimized cloak

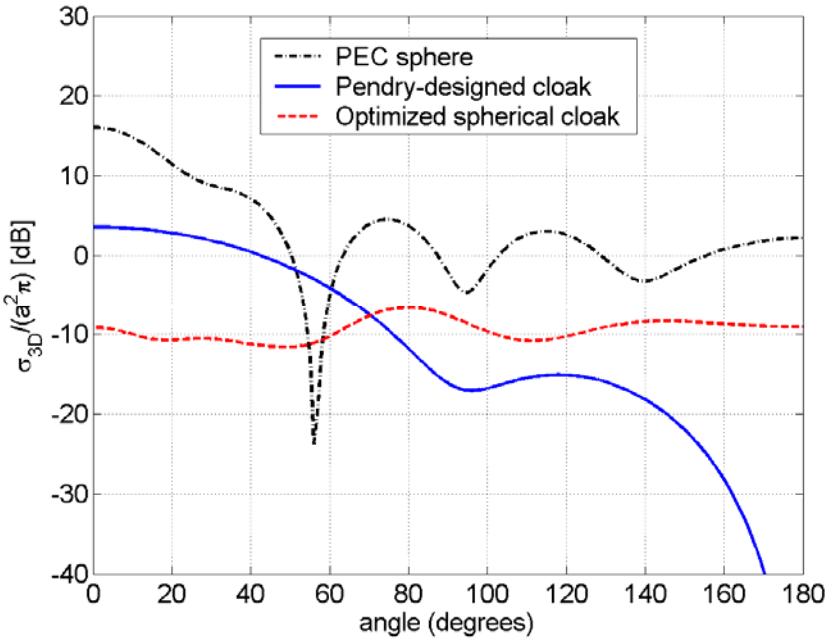

Figure 6.4 Normalized bistatic scattering cross sections of PEC sphere, Pendry (thin) design and optimized cloak.

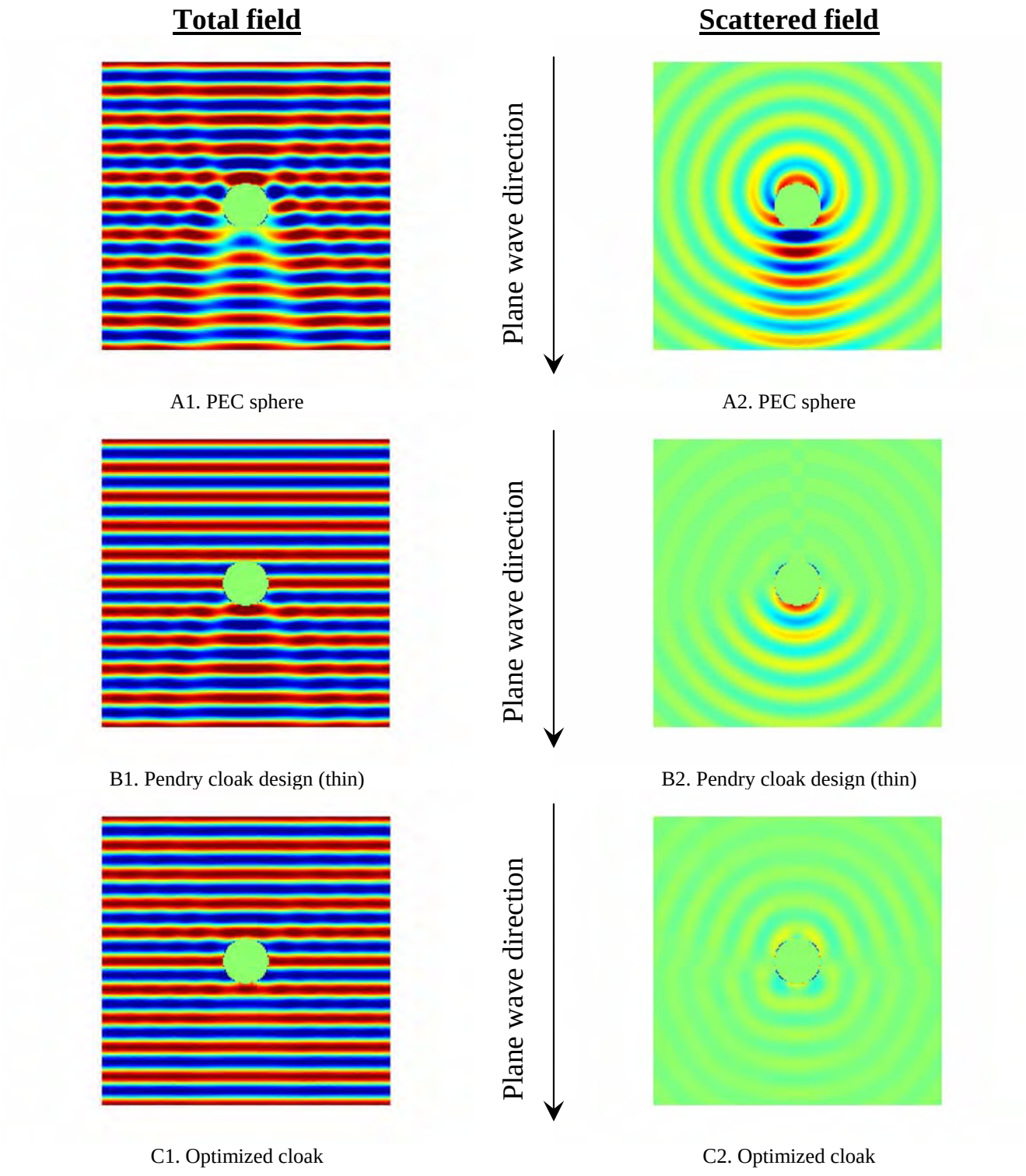

Figure 6.5. Plots of total and scattered field distribution in the vicinity of a PEC sphere (A) and two cloak configurations – five layers Pendry design (B) and two-layers optimized design (C). The plane wave is impinging from top. The scale is normalized for all cases.

CONCLUSIONS

Conclusions

During the 12 months assigned to this project the software for full-wave analysis of uniaxial multilayer cylinders used for invisible cloak realization has been developed. The analysis approach is based on the modal approach, i.e. distribution of the electromagnetic field in radial direction is described with a modified Bessel differential equation that takes into account the radial anisotropy of the proposed structures. Such an approach is suitable for 2D problems, i.e. when the incident wave is propagating in the perpendicular direction to the structure axis. For the oblique incidence case we have developed more general analysis approach in which distribution of the electromagnetic field in radial direction is determined using finite-difference discretization of the appropriate partial differential equations. In order to characterize the level of "invisibility" achieved by metamaterials, we have calculated the total scattering width, as well as the angular variations of scattering width in the azimuthal plane. The scattering properties of a PEC cylinder are also given as a referent case necessary to calculate the total scattering width reduction.

In this report we have shown that the achieved total scattering width reduction is only around three for structures proposed by Pendry and Schurig with anisotropy in radial direction only. The reason for such a small cloak gain lies in the reflection of the incident wave from the cloak surface due to the impedance mismatch. Furthermore, it is shown that the needed continuous radial variation of constitutive parameters can be successfully approximated with about 6 layers of constant permittivity and permeability, meaning there is hardly any improvement of the achieved invisibility for structures with more layers. The needed number of layers with constant constitutive parameters however strongly depends on the radius of the object that we would like to cloak. Furthermore, it was shown that the cloaks that are designed for normal incidence can successfully work for incident angles in the range 75º - 105º. If the incident angle is different from 90º, our analysis approach enables us to make a cloak design for a particular angle of incidence simply by connecting the developed program with the optimization routine.

The dispersion of split-ring-resonator-based structures and thin-wire-based structures were taken into account by Lorentz and Drude models, respectively. It was found that the achieved invisibility is, due to the dispersion, a narrow-band phenomenon. For the TM_z cloak (i.e. for the cloak that was experimentally made by Schurig *et al*.) the invisibility bandwidth (relative frequency range where the total scattering width reduction is larger than 1) is about 0.24%, while for the TE_z cloak (i.e. the cloak that can be made using periodic wire media) the invisibility bandwidth is a bit larger and its value is about 2.4%. This is explained by the fact that the thin-wire-based structures are less sensitive to frequency changes than the split-ring-

resonator-based structures. All the results of the presented analysis show that metamaterial-based cloaks are still in their infant phase, while practical engineering realizations are yet to be seen.

We have also merged the developed analysis program with the global optimization routine based on the PSO algorithm. By this we have developed a software platform that we have used to provide answers to two questions: is it possible to realize a cylindrical cloak that is entirely invisible (at least at the central frequency) only with the radial component of permeability tensor being coordinate dependent, and is it possible to enlarge the bandwidth of such a cloak? The obtained results show that it is indeed possible to realize the "perfect" cylindrical cloak, but at the expense of bandwidth that is reduced to just about 0.08%. The discussion on the influence of the number of cloak layers shows that with only three layers it is possible to obtain a better cloak performance than the Schurig cloak (containing ten layers), and that with ten or more layers one can design a cloak that is practically invisible. However, these results strongly depends on the cloaked object radius, and more layers are needed for structures with larger radius (on the other side, for structures with small radius two-layer cloaks give very good results). Furthermore, it is shown that the bandwidth of the Schurig cloak can indeed be increased by up to a factor of 2.5, by optimizing the cloak layer parameters, while maintaining the same minimal value of the total scattered width. Finally, it is demonstrated that losses in the cloak increase the total scattering width, or in other words, reduce the invisibility gain. However, for values of around $\gamma = 10^{-3} f_0$ the invisibility gain of the optimized cloak is still roughly equal to the invisibility of the Schurig cloak with no losses.

Finally, we have extended the developed program to uniaxial spherical cloaks. The three-dimensional analysis is in principle more suitable for arbitrary geometries of the object. We have compared the properties of cylindrical and spherical cloaks, and the largest difference is in the thickness of the optimum cloak. While in the cylindrical case the typical ratio between the outer and inner radius of the cloak is around 2, in the spherical case this ratio is much smaller, typically around 1.1. By merging the developed program for analyzing multilayered spherical structures with the PSO global optimization routine it was found that it is possible to realize a cloak with only two thin anisotropic layers, which significantly reduces scattered field in comparison to other cloak realizations given in literature.

As a short summary, the realized outcomes of the project are:

- We have developed the program "UniaxCloak" that analyzes cylindrical and spherical cloaks made from the uniaxial materials. The program can fully characterize uniaxial cloaks, i.e. it calculates scattered width and total scattered width in a frequency range of interest. In the cylindrical case, the incident wave can have arbitrary angle of incidence.
- We have merged the program "UniaxCloak" with the global optimization program based on the particle swarm optimization (PSO) method. By this we can determine the optimum cloak design since the analysis methods based on the transformation electromagnetics do not take all the effects into account.
- We have made a detailed investigation of properties of cloaks that are made from uniaxial materials. In practice, such cloaks can be made from metamaterials, for example from split-ring periodic structures or periodic wire structures.

BIBLIOGRAPHY

Bibliography

[1] L.S. Dollin, "On the possibility of comparison of three-dimensional electromagnetic systems with nonuniform anisotropic filling," *Izv. VUZov Radiofizika*, **Vol. 4**, No. 5, pp. 964-967, 1961.

[2] M. Kerker, "Invisible bodies," *J. Opt. Soc. Am.,* **Vol. 65,** pp. 376-379, Apr. 1975.

[3] A. Alu, N. Engheta, "Achieving transparency with plasmonic and metamaterial coatings," *Phys. Rev. E,* **Vol. 72**, 016623, 2005; Erratum, **Vol. 73**, 019906, 2006.

[4] A. Alu, N. Engheta, "Plasmonic materials in transparency and cloaking problem: mechanism, robustness, and physical insights," *Opt. Express*, **Vol. 15**, pp. 3318-3332, Feb. 2007.

[5] B. Edwards, A. Alu, M. G. Silveirinha and N. Engheta, "Experimental verification of plasmonic cloaking at microwave frequencies with metamaterials," Physical Review Letters, **Vol. 103**, 153901, 2009.

[6] P.-S. Kildal, A. A. Kishk, A. Tengs, "Reduction of forward scattering from cylindrical objects using hard surfaces", *IEEE Trans. on Antennas and Propagation.,* **Vol. AP-44**, pp. 1509-1520, Nov. 1996.

[7] W. K. Kahn and H. Kurss, "Minimum-scattering antennas," *IEEE Trans. on Antennas and Propagation,* **Vol. AP-13,** pp. 671–675, Sep. 1965.

[8] N.G. Alexopoulos and N.K. Uzunoglu, "Electromagnetic scattering from active objects: invisible scatterers," *Appl. Opt.* **Vol. 17, pp.** 235–239, Jan. 1978.

[9] J. B. Pendry, D. Schurig, D. R. Smith, "Controlling electromagnetic fields", *Science*, **Vol. 312,** pp. 1780-1782, June 2006.

[10] D. Schurig, J. B. Pendry, and D. R. Smith, "Calculation of material properties and ray tracing in transformation media," *Opt. Express*, **Vol. 14**, pp. 9794-9804, Oct. 2006.

[11] U. Leonhardt, and T.G. Philbin, "General relativity in electrical engineering," *New Journal of Physics*; **Vol. 8**, pp. 247-265, 2006.

[12] A. D. Yaghjian and S. Maci, "Alternative Derivation of Electromagnetic Cloaks and Concentrators," arXiv: 0710.2933, Sep. 2008.

[13] D.-H. Kwon, and D. H. Werner, "Transformation electromagnetics: An overview of theory and applications," *IEEE Trans. on Antennas and Propagation Magazine,* **Vol. 52,** pp. 24-46, Feb. 2010.

[14] D. Schurig, J. J. Mock, B. J. Justice, S. A. Cummer, J. B. Pendry, A. F. Starr, D. R. Smith, "Metamaterial electromagnetic cloak at microwave frequencies", *Science,* **Vol. 314**, pp. 977-980, Nov. 2006.

[15] W. Cai, U. K. Chettiar, A. V. Kildishev, V. M. Shalaev, "Optical cloaking with non-magnetic metamaterials", *Nature photonics,* **Vol. 1**, pp. 224-227, Apr. 2007.

[16] Z. Sipus, P. S. Kildal, R. Leijon, and M. Johansson, "An algorithm for calculating Green's functions for planar, circular cylindrical and spherical multilayer substrates," *ACES Journal*, **Vol. 13,** pp. 243-254, Nov. 1998.

[17] E. F. Knott, J.F. Shaeffer, M. T. Tuley, *Radar Cross Section*, SciTech Publishing, 2004.

[18] S. Hrabar, "Waveguide experiments to characterize the properties of SNG and DNG metamaterials", chapter 3 in N. Engheta and R. Ziolkowsky (Ed.), *Metamaterials: Physics and Engineering Explorations,* John Wiley and IEEE, 2006.

[19] S. Hrabar, L. Benic, J. Bartolic, "Simple experimental determination of complex permittivity or complex permeability of SNG metamaterials", in *Proceedings on 36th European Microwave Conference 2006,* Manchester, UK, pp. 1395-1398, Sep.2006.

[20] H. Chen, Z. Liang, P. Yao, X. Jiang, H. ma, T. Chan, "Extending the bandwidth of electromagnetic cloaks," *Physical review B,* **Vol. 76**, Paper No. 241104(R), 2007.

[21] J. Kennedy and R. C. Eberhart, "Particle swarm optimization," in *Proc. IEEE Conf. Neural Networks IV*, Piscataway, NJ, 1995.

[22] J. Robinson and Y. Rahmat-Samii, "Particle swarm optimization in electromagnetics," *IEEE Trans. on Antennas and Propagation*, **vol. 52**, no. 2, pp. 397-407, Feb. 2004.

[23] R. C. Eberhart and Y. Shi, "Particle swarm optimization: developments, applications and resources," in *Proc. 2001 Congr. Evolutionary Computation*, vol. 1, 2001.

[24] T. Komljenovic, R. Sauleau, Z. Sipus, and L. L. Coq, "Layered Circular-Cylindrical Dielectric Lens Antennas – Synthesis and Height Reduction Technique," *IEEE Trans. on Antennas and Propagation*, **vol. 58**, pp. 1783-1788, May 2010.

[25] J. Kennedy and R. Mendes, "Neighborhood Topologies in Fully Informed and Best-of-Neighborhood Particle Swarms", *IEEE Trans. on Systems, Man, and Cybernetics*, Part C, **vol. 35**, no. 4, pp. 515-519, Jul., 2006.

[26] J. J. Liang, K. Qin, P. N. Suganthan, S. Baskar, "Comprehensive Learning Particle Swarm Optimizer for Global Optimization of Multimodal Functions," *IEEE Trans. on Evolutionary Computation*, **vol. 10**, no. 3, pp. 281-295, Jun. 2006.

[27] B.–I. Popa and S. A. Cummer, "Cloaking with Optimized Homogeneous Anisotropic Layers," *Physical Review A*, 79, 023806, 2009.

[28] Z. Yu, Y. Feng, X. Xu, J. Zhao and T. Jiang, "Optimized cylindrical invisibility cloak with minimum layers of non-magnetic isotropic materials," Journal of Physics D: Applied Physics, **Vol. 44**, 185102, 2011.

[29] J. C. Monzon, "Three-dimensional field representation in a ten parameter cylindrically symmetric anisotropic material," *IEEE Trans. on Antennas and Propagation*, **vol. 38**, pp. 551-555, April 1990.

[30] Bronštejn, Semendjajev, H*andbook of mathematics* , Springer, 1997.

[31] S.Lang, *Calculus of Several Variables*, Springer, 1987.

[32] G.W.Hanson, A.B.Yakovlev, *Operator Theory for Electromagnetics: An Introduction*, Springer, 2002.

[33] D.G.Dudley, *Mathematical Foundations for Electromagnetic Theory*, Wiley-IEEE Press, 1994.

[34] W.Rudin, *Functional Analysis*, McGraw-Hill Science, 1991.

[35] S.Lang, *Linear Algebra*, Springer, 2010.

[36] M.Abramowitz, I.A.Stegun, *Handbook of Mathematical Functions*, Dover Publications, 1965.

[37] M.A.Al-Gwaiz, *Sturm-Liouville Theory and its Applications*, Springer, 2007.

[38] M.N.O.Sadiku, *Numerical Techniques in Electromagnetics with MATLAB*, CRC Press, 2009.

[39] R.Kress, *Numerical Analysis*, Springer, 1998.

[40] C.A.Balanis, *Advanced Engineering Electromagnetics*, John Wiley & Sons, 1989.

[41] J. A. Stratton, *Electromagnetic Theory*, IEEE Press, 2007.

[42] R. F. Harrington, *Time-Harmonic Electromagnetic Fields*, IEEE Press, 2001.

[43] A. Alu, N. Engheta, "Effects of size and frequency dispersion in plasmonic cloaking", *Physical review E*, Vol. 78, p. 045602, 2008.